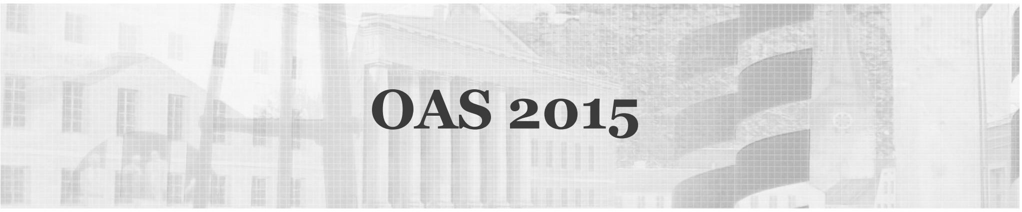

Proceedings of the 3nd International Conference

Optimization and Analysis of Structures

III

Tartu, Estonia, August 23–25, 2015

Editors:
J. Lellep, E. Puman

University of Tartu Press, 2015

The publication of this book has been financed
by the Estonian Doctoral School of Mathematics and Statistics

European Union
European Social Fund

Investing in your future

ISSN 2461-2677

Conference committee

Honorary Chairman:	Professor Emeritus Ülo Lepik
Conference chairman:	Professor Jaan Lellep
Scientific secretary:	Associate Professor Ella Puman

Local organizing committee:

Helle Hein, Heljo Kaima, Tiina Kraav, Alexander Liyvapuu, Annely Mürk, Annika Paltsepp, Julia Polikarpus, Larissa Roots, Ernst Tungel.

Organized by:

Institute of Mathematics, University of Tartu

Conference webpage: **http://oas2015.ut.ee**

International paper committee

J. Atkočiūnas,	Vilnius Gediminas Technical University, Lithuania
N. Banichuk,	A. Yu. Ishlinsky Institute for Problems in Mechanics, Russia
E. Barkanov,	Riga Technical University, Latvia
G. Cheng,	Dalian University of Technology, China
C. Cinquini,	University of Pavia, Italy
J. Engelbrecht,	Tallinn University of Technology, Estonia
J. Herskovits,	Federal University of Rio de Janeiro, Brazil
K. Jarmai,	University of Miskolc, Hungary
N. Jones,	University of Liverpool, UK
R. Kačianauskas,	Vilnius Gediminas Technical University, Lithuania
J. Logo,	Budapest University of Technology and Economics, Hungary
Z. Mróz,	Institute of Fundamental Technological Research, Poland
N. Olhoff,	Aalborg University, Denmark
J. Paavola,	Aalto University, Finland
T. Rabczuk,	Bauhaus-University Weimar, Germany
H. Rodrigues,	Technical University of Lisbon, Portugal
G. Rozvany,	Budapest University of Technology and Economics, Hungary
W. Schmidt,	Greifswald University, Germany
O. Sigmund,	Technical University of Denmark, Denmark
V. Tamuzs,	University of Latvia, Latvia
V. Toropov,	University of Leeds, UK
J. Varna,	Luleå University of Technology, Sweden
N. Vatin,	Peter the Great St. Petersburg Polytechnic University, Russia

Preface

The conferences on the Optimization and Analysis of Structures were held in the University of Tartu since 2011. The first conference of this series, the OAS 2011 was dedicated to the 90th jubileum of Professor Ülo Lepik.

The 2nd International Conference OAS was held in August, 25–27 2013.

This, the 3rd International Conference OAS is organized under the auspices of ISSMO. It takes place in August, 23–25 2015.

The aim of the 3nd International Conference "Optimization and Analysis of Structures 2013" is to stimulate and promote research and applications within applied mechanics and optimization and provide a forum for personal contacts, also for dissemination of existing knowledge in mechanics. We hope that the conference will stimulate the interchange of ideas in the theoretical and applied mechanics, solid mechanics, fracture mechanics as well as in the theory of of optimization and numerical methods of optimization.

The organizing committee gratefully acknowledges the authors of presentations for their contribution.

Jaan Lellep, Chairman of the organizing committee
Ella Puman, Scientific secretary of the conference

Institute of Mathematics, University of Tartu

Contents

Full papers

Study of plane-parallel motion of machine combination

Valerii Adamchuk[1], **Ievgenii Petrychenko**[2]

Institute for Agricultural Engineering and Electrification, National Scientific Centre,
Kiev Region, Ukraine
[1]*adamchukvv1@mail.ru*, [2]*petrichenko-zhenya@mail.ru*

Jüri Olt[3], **Alexander Liyvapuu**[4]
Institute of Technology, Estonian University of Life Sciences,
Tartu, Estonia
[3]*jyri.olt@emu.ee*, [4]*alexander.liyvapuu@emu.ee*

Abstract. A new mathematical model has been developed representing the motion of a seed drill combination simultaneously performing the preceding banded placement of mineral fertilisers. Such a combined unit comprises the gang-up wheeled tractor, the fertiliser distribution module behind the tractor attached to it with the use of a hitch and intended for the banded placement of mineral fertilisers and the grain drill behind the fertiliser distribution module attached to it also with the use of a hitch. For the components of this dynamic system the coordinates of their centres, their masses as well as the external forces and the reactions of the soil surface applied to them have been determined. In order to use the original dynamic equations in the form of the Lagrange equations of the second kind, the generalised coordinates and kinetic energy relations have been determined. Following the necessary transformations, a system of six differential equations of motion has been generated, which characterises the behaviour of the combined machine unit during its plane-parallel motion. In this system, two line coordinates and one angular coordinate characterise the behaviour of the propulsion and power unit (wheeled tractor), while three angular coordinates characterise the rotations of the draft gear and the centres of the machines integrated with its use. The obtained system of six differential equations of plane-parallel motion has been prepared for its solving on a PC in accordance with the developed software programme, which will facilitate the assessment of the stability of motion of the combined unit in the field surface plane when performing the work process.

Keywords: *generalized force, kinetic energy, plane-parallel motion, modelling.*

1. Introduction

Recently, a burning problem of over-compaction of the arable soil has arisen as a result of the high pressure imposed on it by agricultural machinery and the repeated impacts during multiple runs ([4], [5]). This urges to look for ever newer solutions of up-to-date energy-efficient technologies and methods of minimizing the impact of machinery running gear on soil by combining the operations of sowing, fertiliser placement, pre-sowing and post-sowing soil cultivation in the same run of the machine unit.

Overall, this allows to shorten the agro-technical terms of performance of field operations, reduce the loss of moisture due to the shorter interoperation time spans, save fuel and lubricants etc. [6].

The methodology of generating analytical mathematical models of agricultural machines and machine units is rather comprehensively presented in the numerous works by P.M. Vasilenko ([8], [9]), A. Vilde [10]. It is to be noted that the main type of motion of just agricultural machines (towed, direct-mounted and self-propelled) is their plane-parallel motion, because this type of motion determines the quality of performance of the aimed work processes. Many studies have been published about the research into the operation of combined agricultural machine units ([1], [3], [7]).

It should be stressed that the agro-technical and performance data of combined machine and tractor units as well as their productivity depend to a considerable extent on the nature of just their plane-parallel motion. Therefore, research into the plane-parallel motion of various machine units is needed both for the comparative assessment of the existing ones and the design of new concepts. The basic method of such research is the generation and solution of differential equations of the motion of machine units [8].

2. Materials and methods

Generation of differential equations of the plane-parallel motion of the combined machine unit in order to find its rational design and kinematic parameters ensuring the stability of its motion and, accordingly, the quality of performing the work process.

To build a mathematical model of the seed drill combination, we first prepare the equivalent schematic model of the dynamic system comprising the gang-up wheeled tractor at the front, followed by the fertiliser spreading unit attached to the tractor with a hitch, which applies mineral fertilisers in the form of banded spread, followed in its turn by the grain drill also attached with the use of a hitch (Fig. 1).

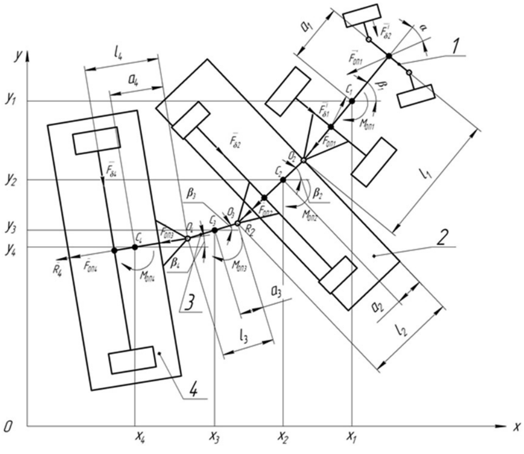

Fig. 1. Equivalent schematic model of the trailed seed drill combination:
1 - tractor, 2 - fertiliser spreading unit, 3 - hitch, 4 - grain drill.

The following assumptions have been made in the process of mathematical modelling. Since the dynamic system under consideration is a multi-mass one, we take into account only the motions of its main components taking place in some fixed plane $x0y$, i.e. we assume that this combined machine unit performs plane-parallel motion. Points C_i $(i = \overline{1,4})$ designate the centres of mass of the main members of the combined machine unit, the motion of which is examined in the adopted plane and the behaviour of which is assumed to be the generalised coordinates.

To generate the differential equations of motion of the examined dynamic system, we designate six generalised coordinates: $x_1, y_1, \beta_1, \beta_2, \beta_3, \beta_4$, which unequivocally identify its position in plane $x0y$. Among them, x_1, y_1 – the coordinates of the tractor's centre of mass, $\beta_1, \beta_2, \beta_3, \beta_4$ – the respective angles between the longitudinal axes of all members of the mechanical system and axis $0x$.

Also, we designate m_i $(i = \overline{1,4})$ – masses of the members of the dynamic system; $C_i(x_i, y_i)$ – centre of mass of the i-th member of the system, $(i = \overline{1,4})$; a_i – distance from the centre of mass of the member of the system to its front articulation joint; l_i – distance between the axes of the adjacent articulation joints.

Let the dynamic system at the initial instant $(t = 0)$ be aligned parallel to axis $0x$ and start moving from this position along this axis from the quiescent state.

To generate the differential equations of motion of this dynamic system, let's use the original dynamic equations in the form of the Lagrange equations of the second kind:

$$\frac{d}{dt}\left(\frac{\partial T}{\partial \dot{q}_s}\right) - \frac{\partial T}{\partial q_s} = Q_s \ (s = \overline{1,6}), \tag{1}$$

where T – kinetic energy of the dynamic system under consideration; q_s – generalised coordinate; s – number of the generalised coordinate; Q_s – generalised force that corresponds to generalised coordinate q_s.

We assume the kinetic energy of this dynamic system to be equal to the sum of the kinetic energies of all its members, taking into account their translational and rotational motions. Then we will have:

$$T = \sum_{i=1}^{4} T_i = \frac{1}{2}\sum_{i=1}^{4}\left[m_i\left(\dot{x}_i^2 + \dot{y}_i^2\right) + I_i\omega_i^2\right], \tag{2}$$

where I_i – moment of inertia of the i-th member around the vertical axis passing through its centre of mass; $\omega_i = \dot{\beta}_i$ – angular rate of turn of the i-th member around the vertical axis passing through its centre of mass; $\dot{x}_i, \dot{y}_i$ – projections of the vector of velocity of the centre of mass of the i-th member of the system on the respective coordinate axes.

Now we will find the expressions for the coordinates of the centre of mass of the i-th $(i = \overline{2,4})$ member of the machine unit, which are accordingly designated x_1, y_1. For that purpose we take into account the designations of the respective coordinates of the centres of mass, the angular displacements of the members at the front and the specified design parameters. Then we will have:

$$\left.\begin{aligned} x_2 &= x_1 - (l_1 - a_1)\cos\beta_1 - a_2\cos\beta_2, \\ y_2 &= y_1 - (l_1 - a_1)\sin\beta_1 - a_2\sin\beta_2, \end{aligned}\right\} \tag{3}$$

$$\left.\begin{aligned} x_3 &= x_1 - (l_1 - a_1)\cos\beta_1 - l_2\cos\beta_2 - a_3\cos\beta_3, \\ y_3 &= y_1 - (l_1 - a_1)\sin\beta_1 - l_2\sin\beta_2 - a_3 a_3\sin\beta_3, \end{aligned}\right\} \tag{4}$$

$$\left.\begin{aligned} x_4 &= x_1 - (l_1 - a_1)\cos\beta_1 - l_2\cos\beta_2 - l_3\cos\beta_3 - a_4\cos\beta_4, \\ y_4 &= y_1 - (l_1 - a_1)\sin\beta_1 - l_2\sin\beta_2 - l_3\sin\beta_3 - a_4\sin\beta_4. \end{aligned}\right\} \tag{5}$$

Relations (3)–(5) can be written down in the general form with the use of the following expressions:

$$\left.\begin{aligned} x_i &= x_1 - (l_1 - a_1)\cos\beta_1 - a_i\cos\beta_i - \sum_{j=2}^{i-1} l_j\cos\beta_j, \\ y_i &= y_1 - (l_1 - a_1)\sin\beta_1 - a_i\sin\beta_i - \sum_{j=2}^{i-1} l_j\sin\beta_j, (i = \overline{2,4}). \end{aligned}\right\} \tag{6}$$

Differentiating expression (6) with respect to time, we express the velocities of the centres of mass of system members in the general form:

$$\left.\begin{aligned} \dot{x}_i &= \dot{x}_1 + (l_1 - a_1)\dot{\beta}_1 \sin\beta_1 + a_i\dot{\beta}_i \sin\beta_i + \sum_{j=2}^{i-1} l_j\dot{\beta}_j \sin\beta_j, \\ \dot{y}_i &= \dot{y}_1 - (l_1 - a_1)\dot{\beta}_1 \cos\beta_1 - a_i\dot{\beta}_i \cos\beta_i - \sum_{j=2}^{i-1} l_j\dot{\beta}_j \sin\beta_j\,, (i = \overline{2,4}). \end{aligned}\right\} \quad (7)$$

Substituting obtained expressions (7) into (2), we obtain the final formula for the kinetic energy of this dynamic system:

$$T = \frac{1}{2}\left[m_1(\dot{x}_1^2 + \dot{y}_1^2) + I_1\dot{\beta}_1^2 + \sum_{i=2}^{4}\left[m_i\left(\dot{x}_i^2 + \dot{y}_i^2\right) + I_i\dot{\beta}_i^2\right]\right]. \quad (8)$$

Now let’s find the generalised forces that correspond to the assumed generalized coordinates.

For this purpose we reduce the forces acting on the wheels of the machine and tractor unit to the front and rear axles of the tractor [2]. The wheeled tractor that gangs up this combined unit has a wheel configuration of 4W2 with the driving rear axle, while the turns of the tractor are implemented by changing the positions of its front wheels (turning them through angles α).

Let’s designate the forces acting on this machine unit as follows:

F'_{k1} – tractive force of the tractor;
F_{0ni} – resisting force of the i-th member of the unit;
$F_{\delta i}$ – lateral force acting on the i-th member of the unit;
M_{0ni} – moment of resistance to rotation by the i-th member of the unit;
P_l and P_n – forces of the rolling resistance of wheels reduced to the tractor’s rear axle and assigned to force F_{0n2} and moment M_{0n2};
R_2 – total resisting force of the openers of the fertiliser sowing unit;
R_3– total resisting force of the openers of the grain drill.

All these forces and moments are specified according to [1] and the respective experimental studies depending on the type of soil, the tractor’s tyre parameters, the type of tractor etc.

Following the above-listed designations, the generalised force will be determined by the formula:

$$Q_{x_1} = \frac{1}{\delta x_1}\left[\sum_{i=1}^{n} \delta A\left(\vec{F}_i^a\right)\right]_{x_1} = \frac{1}{\delta x_1}\left[\sum_{i=1}^{4} F_{xi}\delta x_i\right]_{x_1} = \sum_{i=1}^{4} F_{xi},$$

bearing in mind that $\delta x_i = \delta x_1 \;\; (i = \overline{1,4})$.

Thus:

$$Q_{x_1} = \sum_{i=1}^{4} F_{xi}. \quad (9)$$

and similarly:

$$Q_{y_1} = \sum_{i=1}^{4} F_{yi}, \tag{10}$$

where F_{xi}, F_{yi} – sums of the projections of all forces acting on the i-th member of the dynamic system respectively on axes $0x$ and $0y$.

To find out the generalised forces that correspond to angular displacements β_i $(i = \overline{1,4})$, we determine the coordinates of articulation joints $O_i(x_{0i}, y_{0i})$ $(i = \overline{1,4})$ and their variation:

$$\left.\begin{aligned} x_{0i} &= x_1 - (l_1 - a_1)\cos\beta_1 - \sum_{j=2}^{i-1} l_j \cos\beta_j\,, \\ y_{0i} &= y_1 - (l_1 - a_1)\sin\beta_1 - \sum_{j=2}^{i-1} l_j \sin\beta_j\,. \end{aligned}\right\}$$

Hence:

$$\left.\begin{aligned} \delta x_{0i} &= \delta x_1 - (l_1 - a_1)\sin\beta_1\,\delta\beta_1 - \sum_{j=2}^{i-1} l_j \sin\beta_j\,\delta\beta_j, \\ \delta y_{0i} &= \delta y_1 - (l_1 - a_1)\cos\beta_1\,\delta\beta_1 - \sum_{j=2}^{i-1} l_j \cos\beta_j\,\delta\beta_j. \end{aligned}\right\} \tag{11}$$

Then generalised force Q_{β_1} will be defined by the following expression:

$$Q_{\beta_1} = \sum_{k=1}^{n} \delta A(\vec{F}_k^a)\,/\delta\beta_1 = M_{c_1} - M_{0n_1} + \sum_{i=2}^{4}\left[F_{xi}\delta x_{0i} + F_{yi}\delta y_{0i}\right]\,/\delta\beta_1 =$$
$$= (l_1 - a_1)\left[\sin\beta_1 \sum_{i=2}^{4} F_{xi} - \cos\beta_1 \sum_{i=2}^{4} F_{yi}\right] + M_{c_1} - M_{0n_1}.$$

That takes into account the fact that according to (11) at $\delta\beta_1 > 0$ we have:

$$\delta x_1 = \delta x_2 = \delta\beta_2 = \delta\beta_3 = \delta\beta_4 = 0,$$
$$\delta x_{0i} = (l_1 - a_1)\sin\beta_1\,\delta\beta_1,$$
$$\delta y_{0i} = -(l_1 - a_1)\cos\beta_1\,\delta\beta_1.$$

The final formula for the generalized force will have the following shape:

$$Q_{\beta_1} = M_{c_1} - M_{0n_1} + (l_1 - a_1)\left[\sin\beta_1 \sum_{i=2}^{4} F_{xi} - \cos\beta_1 \sum_{i=2}^{4} F_{yi}\right], \tag{12}$$

where M_{c_1} – algebraic sum of the moments of all forces acting on the first member of the dynamic system with respect to point C_1. Similarly, we find $Q_{\beta_i}(i = \overline{2,4})$:

$$Q_{\beta_i} = \left[\sum_{k=1}^{n} \delta A(\vec{F}_k^a)\right]_{\beta_i} /\delta\beta_i = M_{0_i} - M_{0n_i} + \sum_{j=i+1}^{4}\left[F_{xj}\delta x_{0i} + F_{yj}\delta y_{0j}\right]\,/\delta\beta_i =$$

$$= M_{0_i} - M_{0n_i} + l_i \left[\sin\beta_i \sum_{j=i+1}^{4} F_{xj} - \cos\beta_i \sum_{j=i+1}^{4} F_{yj} \right].$$

In this equation we take into account that:

$$\delta y_{0i} = -l_i \cos\beta_i \, \delta\beta_i, \qquad \delta x_{0i} = l_i \sin\beta_i \delta\beta_i.$$

Finally we arrive at the formula:

$$Q_{\beta_i} = M_{0_i} - M_{0n_i} + l_i \left[\sin\beta_i \sum_{j=i+1}^{4} F_{xj} - \cos\beta_i \sum_{j=i+1}^{4} F_{yj} \right], (i = \overline{2,4}), \qquad (13)$$

where M_{0i} – algebraic sum of the moments of all forces acting on the i-th member of the dynamic system with respect to point 0_i.

3. Results and discussion

Thus, we have obtained all data needed for the use of original dynamic equation (1). After making all substitutions and transformations, we will obtain the system of differential equations that characterises the motion of the towed combined sowing unit in the horizontal plane:

$$\left.\begin{aligned}
& m_1\ddot{x}_1 + \sum_{i=2}^{4} m_i\ddot{x}_i = \sum_{i=1}^{4} F_{xi}, \\
& m_1\ddot{y}_1 + \sum_{i=2}^{4} m_i\ddot{y}_i = \sum_{i=1}^{4} F_{yi}, \\
& I_1\ddot{\beta}_1 + (l_1 - a_1)\sum_{i=2}^{4} m_i(\ddot{x}_i \sin\beta_1 - \ddot{y}_i \cos\beta_1) = M_{c_1} - M_{0n_1} + \\
& \qquad +(l_1 - a_1)\left[\sin\beta_1 \sum_{i=2}^{4} F_{xi} - \cos\beta_1 \sum_{i=2}^{4} F_{yi}\right], \\
& I_2\ddot{\beta}_2 + m_2a_2(\ddot{x}_2 \sin\beta_1 - \ddot{y}_2 \cos\beta_2) + l_2(m_3(\ddot{x}_3 \sin\beta_2 - \ddot{y}_3 \cos\beta_2) + \\
& \qquad +m_4(\ddot{x}_4 \sin\beta_2 - \\
& -\ddot{y}_4 \cos\beta_2)) = M_{0_2} - M_{0n_2} + l_2\left[\sin\beta_2 \sum_{j=3}^{4} F_{xj} - \cos\beta_2 \sum_{j=3}^{4} F_{yj}\right], \\
& I_3\ddot{\beta}_3 + m_3a_3(\ddot{x}_3 \sin\beta_3 - \ddot{y}_3 \cos\beta_3) + l_3m_4(\ddot{x}_4 \sin\beta_3 - \ddot{y}_4 \cos\beta_3) = \\
& \qquad = M_{0_3} - M_{0n_3} + l_3[\sin\beta_3 F_{x4} - \cos\beta_3 F_{y4}], \\
& I_4\ddot{\beta}_4 + m_4a_4(\ddot{x}_4 \sin\beta_4 - \ddot{y}_4 \cos\beta_4) = M_{0_4} - M_{0n_4}.
\end{aligned}\right\} \qquad (14)$$

In system (14), the first two equations characterise the motions of the gang-up tractor along axes Ox and Oy, the third equation characterises the rotational motions of the tractor about the centre of mass. The last three equations of system (14) characterise the rotational motions of the fertiliser sowing module and grain drill as well as their draft gear.

Thus, we have obtained a system of six differential equations (14), which characterises the motions of the combined sowing machine and tractor unit performing simultaneously the banded placement of mineral fertilisers. This dynamic system has six degrees of freedom and its computational solution with the use of a PC will allow to find out not only the patterns of motion of each system member in the horizontal plane, but also the design and kinematic parameters providing for the stability of motion in the said plane.

4. Conclusion

An equivalent schematic model has been developed for the combined machine and tractor unit, which performs simultaneously the work processes of the banded placement of mineral fertilisers and the sowing of grain crops, i.e. a three-mass dynamic system in plane-parallel motion.

For the dynamic system under consideration the expressions have been obtained for the coordinates of its centres of mass, the generalised coordinates have been established and the expressions have been generated for the kinetic energy and generalised forces.

Basing on the original dynamic equations in the form of the Lagrange equations of the second kind, the operations stipulated by their use have been carried out and finally a system has been obtained comprising six differential equations, which characterise the behaviour of the dynamic system under consideration in the horizontal plane.

The computational solution of the obtained system of differential equations with the use of a PC will allow to select such design and kinematic parameters of the combined sowing machine unit, which will ensure the stability of its motion in the horizontal plane.

References

[1] V.M. Bulgakov and A.J. Gorbovoy. *Theory of motion of flax harvesters*. Lvov, 2007.

[2] R.H. Macmillan. *The Mechanics of Tractor – Implement Performance*. Theory and Worked Examples. University of Melbourne, 2002.

[3] V.T. Nadykto. Basic principles of ganging up modular power facilities. Melitopol, 2003.

[4] V. Nadykto, M. Arak and J. Olt. Theoretical research into the frictional slipping of wheel-type undercarriage taking into account the limitation of their impact on the soil. *Agronomy Research*, Vol. 13, No. 1, 2015, pp. 148–157.

[5] M. Schreiber and H. Kutzbach. Influence of soil and tire parameters on traction. *Research in Agricultural Engineering*, Vol. 54, No. 2, 2008, pp. 43–49.

[6] E. Šarauskis, S. Buragiene, K. Romaneckas, A. Sakalauskas, A. Jasinskas, E. Vaiciukevicius and D. Karayel. Working time, fuel consumption and economic analysis of diferent tillage and sowing systems in Lithuania. *Engineering for Rural Development*, 2012, pp. 52–59.

[7] O. Valainis, A. Rucins and A. Vilde. Technological operational assessment of one pass combined agricultural machinery for seedbed preparation and seeding. *Engineering for Rural Development*, 2014, pp. 37–43.

[8] P.M. Vasilenko. *Methodology of developing analytical functional models of mechanical systems* (machines and machine units), Kiev, 1980.

[9] P.M. Vasilenko. *Introduction to agricultural mechanics*. Kiev, Agricultural Education, 1996.

[10] A. Vilde and A. Rucis. Development of agricultural mechanics. Engineering for Rural Development, 2012, pp. 67–73.

Parameter identification in vibrating non-homogeneous functionally graded Timoshenko beams

Ljubov Feklistova[1], **Helle Hein**[2]

Institute of Computer Science, University of Tartu
Tartu, Estonia
[1]*ljubov.feklistova@ut.ee*, [2]*helle.hein@ut.ee*

Abstract. In the present paper the determination of parameters in axially functionally graded Timoshenko beams is considered. The modal analysis method using the Haar wavelets is applied for calculating the data patterns. A combined approaches using the Haar wavelets, artificial neural networks and/or random forest are applied to solve the identification problems. The effectiveness of the proposed methods is evaluated with the aid of numerical experiments. The advantage of the methods lies in the ability to make fast and accurate predictions.

Keywords: *Haar wavelets, functionally graded material, Timoshenko theory, neural networks, random forest.*

1. Introduction

Large number of papers are devoted to the free vibration analysis of homogeneous Euler-Bernoulli and Timoshenko beams; however, considerably less research has been undertaken on the buckling of non-uniform Timoshenko beams and axially functionally graded (FG) beams due to the complexity of the problem. The buckling of the functionally graded Euler-Bernoulli beam has been analyzed in [1]. Filipich, Rosales et al. used Fourier series and the Timoshenko beam theory to calculate the exact values of natural frequencies [2]. Gunda, Gupta et al. studied the free vibration of uniform isotropic Timoshenko beams with geometric nonlinearity and all possible boundary conditions using the finite element method (FEM) and the harmonic balance method [3]. An alternative approach was proposed by Liao and Zhong in [4]: the nonlinear flexural vibration of tapered Timoshenko beams were calculated with the aid of the differential quadrature method. Yihua, Li et al. scrutinized the vibration of Timoshenko beams on a non-linear elastic foundation using a weak form of the quadrate element method and noticed that the foundation parameter affects conspicuously the fundamental frequency of the beams [5]. Yesilce, Demirdag et al. obtained the frequencies and mode shapes for the free vibration of the multi-span Timoshenko beam with multiple spring-mass systems with a different number of spans and spring-masses in different locations [6]. Mohd and Dawe were the first who started studying buckling using the FEM; however, the object of the research was thin laminated shell [7]. The critical buckling load of axially non-uniform beams with elastic boundary conditions were studied by Huang and Luo: they transformed the governing equation with varying coefficients into a system of linear algebraic equations with unknown coefficients and obtained the characteristic equation for the critical buckling loads [8].The determination of the buckling load using neural networks in cylindrical shells has been studied by Waszczyszyn and Bartczak [9]. They studied the cylindrical shells with geometrical imperfection and used the imperfection parameters at inputs of the neural networks for predicting the buckling load. In the present paper, the critical buckling load in vibrating Timoshenko beams is studied by the neural networks and random forest.

2. Buckling of functionally graded Timoshenko beam

Consider an axially graded Timoshenko beam of length L with a variable cross-section area $A(x)$ subjected to compressive load P. Applying the Hamilton's principle, the following equations can be derived

$$\frac{\partial}{\partial x}\left[E(x)I(x)\frac{\partial\tilde{\theta}}{\partial x}\right]+kG(x)A(x)\left(\frac{\partial w}{\partial x}-\tilde{\theta}\right)-\varrho(x)I(x)\frac{\partial^2\tilde{\theta}}{\partial t^2}=0, \tag{1}$$

$$\frac{\partial}{\partial x}\left[kG(x)A(x)\left(\frac{\partial w}{\partial x}-\tilde{\theta}\right)\right]-\frac{\partial}{\partial x}\left(P\frac{\partial w}{\partial x}\right)-\varrho(x)A(x)\frac{\partial^2 w}{\partial t^2}=0. \tag{2}$$

In (1) and (2), $\tilde{\theta}(x,t)$ and $w(x,t)$ are the bending rotation and the transverse displacement depending on the longitudinal coordinate x and time t; $E(x)$ and $G(x)$ are the Young's and shear moduli, respectively; $I(x)$ is the moment of inertia; $\varrho(x)$ is the mass density and k is the shear correction factor which depends on the shape of the cross-section. Assuming sinusoidal variations of the transverse displacement and bending rotation with a circular frequency ω, equations (1) and (2) can be presented as:

$$\frac{d}{dx}\left[E(x)I(x)\frac{d\theta}{dx}\right]+kG(x)A(x)\left(\frac{dW}{dx}-\theta\right)+\varrho(x)I(x)\theta=0, \tag{3}$$

$$\frac{d}{dx}\left[kG(x)A(x)\left(\frac{dW}{dx}-\theta\right)\right]-\frac{d}{dx}\left(P\frac{dW}{dx}\right)+\varrho(x)A(x)\omega^2W(x)=0. \tag{4}$$

From equations (3) and (4) the equation for determining the critical buckling load can be obtained:

$$\frac{d^2}{dx^2}\left[E(x)I(x)\frac{d\theta}{dx}\right]+P\frac{d}{dx}\left[\theta(x)-\frac{1}{kG(x)A(x)}\frac{d}{dx}[E(x)I(x)]\frac{d\theta}{dx}\right]=0. \tag{5}$$

In the present paper, it is assumed that the functions $E(x),\varrho(x),A(x)$ and $I(x)$ take the following form:

$$E(x)=E_0E_1(x),\rho(x)=\rho_0\rho_1(x),A(x)=A_0A_1(x),I(x)=I_0I_1(x), \tag{6}$$

where $E_0=E(0),\varrho_0=\varrho(0),A_0=A(0)$ and $I_0=I(0)$. Introducing the following dimensionless parameters:

$$\tilde{x}=\frac{x}{L},\varpi^2=\frac{\varrho_0A_0L^4}{E_0I_0}\omega^2,s^2=\frac{2r^2(1+\nu)}{k},r^2=\frac{I_0}{A_0L^2},\lambda=\frac{PL^2}{E_0I_0} \tag{7}$$

and taking into account $\omega=0$ the system of equations (3) and (4) takes the form:

$$\begin{gathered}\frac{d}{d\tilde{x}}\left[E_1(\tilde{x})I_1(\tilde{x})\frac{d\theta}{d\tilde{x}}\right]+s^{-2}E_1(\tilde{x})A_1(\tilde{x})\left(\frac{dW}{d\tilde{x}}-\theta(\tilde{x})\right)=0,\\ s^{-2}\frac{d}{d\tilde{x}}\left[E_1(\tilde{x})A_1(\tilde{x})\left(\frac{dW}{d\tilde{x}}-\theta(\tilde{x})\right)\right]-\lambda\frac{d^2W}{d\tilde{x}}=0.\end{gathered} \tag{8}$$

The critical buckling load is closely related to the end supports of the beam. The expressions for the beam with clamped ends can be presented as follows

$$W(0)=\theta(0)=W(1)=\theta. \tag{9}$$

To solve the system of equations (8) with boundary conditions (9), the procedure described in [11] was applied. In this paper, it is also assumed that the material properties of the FG beam vary along the axis of the beam with the following power law relation [12]:

$$E_1(\tilde{x}) = Y_0\tilde{x}^n + 1, Y_0 = E_a/E_z - 1, \tag{10}$$

where $E_a = 70$ GPa and $E_z = 200$ GPa correspond to the Young's moduli of aluminium and zirconia, respectively. The cross-section of the beam and the moment of inertia are assumed to vary along the axis as following:

$$\mathrm{A}_1(\tilde{x}) = 1 - c\tilde{x}, I_1(\tilde{x}) = (1 - c\tilde{x})^3, \tag{11}$$

where c is the taper ratio of the beam.

3. Haar wavelets

The wavelet transform has been implemented in the parameter detection as well as in the structural health monitoring due to the fact that the wavelet transform does not require the analysis of the complete structure and has the ability to reveal some hidden parts of the data. The Haar wavelet family is a group of square waves [11]:

$$h_i(x) = \begin{cases} 1, & x \in \left[\frac{k}{m}, \frac{2k+1}{2m}\right] \\ -1, & x \in \left[\frac{2k+1}{m}, \frac{k+1}{m}\right] \\ 0, & elsewhere, \end{cases} \tag{12}$$

where m is the index of dilatation and it is equal to $2j; j = 0,1,\ldots,J$ indicates the level of the wavelet; $k = 0,1,\ldots,m-1$ is the translation parameter. Integer J determines the maximal level of resolution. Index i is calculated according to the formula: $i = m + k + 1$. Any function $y(x)$, which is square integrable in the interval [0,1], can be expanded into a Haar series with an infinite number of terms:

$$y(x) = \sum_{i=0}^{\infty} c_i h_i(x), \tag{13}$$

where the Haar coefficients are determined in a such way that the integral square error ε is minimized

$$\varepsilon = \int_0^1 \left[y(x) - \sum_{i=1}^{m} c_i h_i(x) \right]^2 dx. \tag{14}$$

The Haar functions $h_i(x)$ can be calculated in the collocation points: $x_l = (l - 0.5)/2M$, where $l = 1,2,\ldots,2M$. The matrix $H(i,l) = h_i(x_l)$, which is associated with the Haar wavelets, can be presented as following

$$H(i,l) = \begin{vmatrix} h_1(x_1) & \ldots & h_1(x_{2M}) \\ \ldots & \ldots & \ldots \\ h_{2M}(x_1) & \ldots & h_{2M}(x_{2M}) \end{vmatrix} = H. \tag{15}$$

Both matrices H and H^{-1} are calculated once and contain zeros. In the present work the Haar transform is applied to the transverse displacement and bending rotation to calculate the pattern set to train the machine learning methods.

4. Numerical examples

Case study 1. Firstly, the buckling load was predicted by two independent machine learning methods: the artificial neural networks (ANNs) and the random forest (RF). More specifically, the feedforward ANN had only one hidden layer since only one parameter had to be predicted; the Elliot symmetric sigmoid was used as a transfer function. In the case of the RF, the ensemble had 27 trees and the number of the predictors at nodes of the trees was equal to approximately three forth of the elements in the pattern. In both methods, the same datasets were used. The training dataset consisted of 79 training patterns; each pattern contained 16 Haar coefficients and the buckling load. In the test dataset, there were ten patterns which were not shown to the systems in advance. Each system was tested hundred times; the average results of the all runs are shown in Table 1. In order to compare the results of two different methods, the mean square error (MSE) was calculated.

Case study 2. Secondly, two parameters, the axially tapered constant c and the buckling load, were predicted by the same machine learning methods using the datasets described in the previous case study. Importantly, the ANN contained two hidden layers. In the case of the RF, the axially tapered constant was predicted by the ensemble of 18 trees and the buckling load was predicted by the ensemble of five trees only; the number of the predictors at nodes was ten and eight, respectively.

The results of the predictions are shown in Table 2, where the mean square error was calculated for two parameters together.

Table 1. Prediction of the buckling load.

Exact	Predictions by NNs		Predictions by RF	
λ	λ	MSE	λ	MSE
0.09	0.0902	0.0019	0.0863	0.0408
0.16	0.1594	0.0040	0.1545	0.0344
0.21	0.2082	0.0086	0.2089	0.0054
0.34	0.3403	0.0007	0.3370	0.0088
0.40	0.3997	0.0007	0.4033	0.0081
0.45	0.4496	0.0009	0.4487	0.0029
0.57	0.5708	0.0014	0.5679	0.0037
0.60	0.6005	0.0009	0.5985	0.0024
0.76	0.7608	0.0010	0.7586	0.0029
0.87	0.8730	0.0035	0.8712	0.0013

5. Summary

Two machine learning methods were applied to solve the inverse problem of buckling: the conventional feedforward backpropagation ANN and the novel random forest method. The buckling load and/or axially tapered constant were predicted. Both methods are fast, computationally efficient, and accurate: the mean square errors of the predictions were generally less than one per cent, but in the case of ANNs, the error was always less than one per cent. Therefore, both methods can serve as a good reference for the future numerical research on buckling.

Table 2. Prediction of the axially tapered constant and the buckling load.

Exact		**Predicted by ANNs**			**Predicted by RF**		
c	λ	c	λ	**MSE**	c	λ	**MSE**
10.1013	0.0900	10.0868	0.0915	0.0014	10.1386	0.0858	0.0037
9.3135	0.1600	9.3113	0.1599	0.0002	9.3782	0.1547	0.0070
8.7458	0.2100	8.7405	0.2115	0.0006	8.7517	0.2099	0.0007
7.1660	0.3400	7.1616	0.3405	0.0006	7.1848	0.3359	0.0027
6.4002	0.4000	6.3980	0.4001	0.0003	6.3673	0.4009	0.0051
5.7625	0.4500	5.7510	0.4505	0.0020	5.8005	0.4496	0.0066
4.2550	0.5700	4.2668	0.5691	0.0028	4.2736	0.5659	0.0044
3.8869	0.6000	3.8989	0.5994	0.0031	3.9073	0.5978	0.0052
2.0276	0.7600	2.0300	0.7612	0.0012	2.0663	0.7583	0.0179
0.9146	0.8700	0.9026	0.8703	0.0095	0.9044	0.8701	0.0081

Acknowledgement

This research was financially supported by the ESF under Grant ETF 8830 and IUT34-4.

References

[1] J. Rychlewska. Buckling Analysis of Axially Functionally Graded Beams. *Journal of Applied Mathematics and Computational Mechanics*, Vol. 13, 2014, pp. 103–108.

[2] C.P. Filipich and M.B.R.H. Cortinez. Natural Frequencies of a Timoshenko Beam: Exact values by means of a generalized solution. *Mecanica Computacional*, Vol. 14, 1994, pp. 134–143.

[3] J.B. Gunda, R.K. Gupta, G.R. Janardhan and G.V. Rao. Large Amplitude Vibration Analysis Of Composite Beams: Simple Closed-Form Solutions. *Composite Structures*, Vol. 93, 2011, pp. 870–879.

[4] Liao, M. and Zhong, H. Nonlinear Vibration Analysis of Tapered Timoshenko Beams. *Chaos, Solitons & Fractals*, Vol. 36, 2008, pp. 1267–1272.

[5] M. Yihua, O. Li and Z. Hongzhi. Vibration Analysis of Timoshenko Beams on a Nonlinear Elastic Foundation. *Tsinghua Science and Technology*, Vol. 14, No. 3, 2009, pp. 322–326.

[6] Y. Yesilce, O. Demirdag and S. Catal. Free Vibrations of Multi-Span Timoshenko Beam Carrying Multiple Spring-Mass Systems. *International Journal of Mechanical Sciences,* Vol. 50, 2008, pp. 995–1003.

[7] S. Mohd and D.J. Dawe. Buckling and Vibration of Thin Laminated Composite. Prismatic Shell Structures, *Composite Structures*, Vol. 25, 1993, pp. 353–362.

[8] Y. Huang and Q. Luo. A Simple Method to Determine the Critical Buckling Loads for Axially Inhomogeneous Beams With Elastic Restraint. *Computers & Mathematics with Applications*, Vol. 61, 2011, pp. 2510–2517.

[9] Z. Waszczyszyn and M. Bartczak. Neural Prediction of Buckling Loads of Cylindrical Shells with Geometrical Imperfection. *International Journal of Non-Linear Mechanics*, Vol. 37, 2002, pp. 763–775.

[10] Ü. Lepik and H. Hein. *Haar Wavelets, with Applications*. Springer, 2014, 212 p.

[11] A. Shahba, R. Attarnejad, M.T. Marvi and S. Hajilar. Free Vibration and Stability Analysis of Axially Functionally Graded Tapered Timoshenko Beams with Classical and Non-Classical Boundary Conditions. *Composites: Part B*, Vol. 42, 2011, pp. 801–808.

Optimal design and analysis of structures via fuzzy stochastic procedures

Zdeněk Kala
Department of Structural Mechanics, Brno University of Technology
Brno, Czech Republic
kala.z@fce.vutbr.cz

Abstract. The presented paper deals with the fuzzy stochastic reliability verification of a steel member designed according to the European Design Standards. The structural reliability of a steel strut is verified by a fuzzy-probabilistic method. If interpretable information was provided by experiments, thus input material and geometrical characteristics of the calculation model could be considered to be random quantities. Fuzzy numbers were considered in the cases where statistic data were incomplete. The output quantity of calculation model is the fuzzy reliability index. Fuzzy and stochastic uncertainties of both input and output quantities of calculation models are discussed.

Keywords: *strut, steel, imperfection, verification, fuzzy, target reliability, optimization.*

1. Introduction

Long-term interest in probabilistic reliability assessment of building structures is given by the possibility of clear expression of random variable characteristics of the problems solved. Thus, the probabilistic approach enables of comprehend a random interaction of often mutually antagonistic parameters. The principle of a steel structure design according to EUROCODES Standards is based on the calculation of design resistance. The design resistance is a function of characteristic values of material characteristics, and of nominal values of geometrical characteristics, and of partial safety factors. Real material and geometrical charactersitics are not constants, but they are random quantities. Basic parameters of hot-rolled steel members are yield strength, and geometrical characteristics. In this case it is possible to exploit the large amount of experimentally obtained information [1, 2]. Statistical information on initial imperfections of member curvature, system imperfections, and joint stiffness is relatively less.

The real resistance is a random quantity higher than the design resistance with high probability. The output of probabilistic methods is usually the quantitative description of reliability degree, whether in form of failure probability P_f, or of the reliability index β. The structure reliability is usually being analyzed by comparison of probability failure P_f, and of target probability failure P_t. An alternative approach is a comparison of the reliability index β and of target reliability index β_t.

The aim of this paper is to analyze the influence of fuzzy uncertainty of input random variables on the fuzzy uncertainty of the misalignment of reliability index β. Statistical characteristics of all material and geometrical quantities influencing the resistance are known, except the shape and size of initial curvature of the member axis. The shape of one half-wave of the sine function with amplitude e_0 was considered in compliance with [3, 4]. The zero mean value and skewness can be assigned, to great extent of certitude, to amplitude e_0, but to determine the standard deviation and kurtosis, there is little relevant information.

2. Verification of the procedures of structural stability design

2.1. Design resistance according to EUROCODE 3

The reliability problem of compressed member of I-beam profile IPE 200 was studied applying an analysis of the failure probability misalignment [5]. The design resistance of the strut according to the unified European concept of EUROCODE 3 [6] is given as:

$$R_d = \frac{\chi_b f_{yk} A_n}{\gamma_{M1}} = \frac{0.597 \cdot 235\text{MPa} \cdot 2.7248 \cdot 10^{-3}\text{m}^2}{1.0} = 382.3\ \text{kN} \tag{1}$$

A compressed strut loaded by permanent action G combined with single variable action Q was considered. The design load action F_d can be expressed by:

$$F_d = \gamma_G G_k + \gamma_Q Q_k \tag{2}$$

It was assumed that the strut was designed for economic design (maximum exploitation): $F_d = R_d$. The partial safety factors $\gamma_G = 1.35$ and $\gamma_Q = 1.5$ were considered according to [7]. The characteristic values G_k and Q_k can be determined according to (2) in dependence on the chosen ratio $\delta = Q_k/(G_k + Q_k)$ [5].

2.2. Probabilistic analysis of reliability

For permanent action G, the Gaussian density function with mean value $m_G = G_k$ and standard deviation $0.1 m_G$ is assumed. For variable action Q, Gumbel-max density function with mean value $m_Q = 0.6 Q_k$ and standard deviation $S_Q = 0.21 Q_k$ is considered [5]. The analysis of the member reliability is based on the condition:

$$G = R - (G + Q) > 0. \tag{3}$$

The random R is calculated for random input material and geometrical characteristics from Tab. 1. The resistance was calculated, according to [8] in the form (4).

$$R = -\frac{\sqrt{A^2 Q^2 + 2AF_{cr}W_z\left(|e_0|F_{cr} - f_y W_z\right) + F_{cr}^2 W_z^2} - AQ - F_{cr}W_z}{2W_z}, \tag{4}$$

where

$$Q = |e_0|F_{cr} + f_y W_z, \tag{5}$$

$$A = 2t_2 b + (h - 2t_2)t_1, \tag{6}$$

$$F_{cr} = \pi^2 \frac{EI_z}{L^2}, \tag{7}$$

$$I_z = \frac{t^2 b^3 + (h - 2t_2)t_1^3}{12}, \tag{8}$$

$$W_z = \frac{I_z}{b/2}, \tag{9}$$

where E is Young's modulus, $L = 2.1\text{m}$ is the strut length, h is the cross-section height, b is the cross-section width, t_1 is the web thickness, t_2 is the flange thickness, F_{cr} is Euler's critical force (buckling load) and I_z is second moment of area arround minor axis z.

2.3. Input quantities

The statistical material and geometrical characteristics of profile IPE 200 were considered according to results of experimental research [1]. The influence of residual stress was not taken into consideration in the numerical study. Statistical characteristics of Young's modulus E are considered according to two independently performed experimental researches [9], see Table 1.

With certainty it can be presumed that the positive and negative realizations of e_0 occur with the same frequency. Based on the symmetry of the IPE 200 profile, it can be assumed that the mean value of e_0 is equal to zero (because by averaging of all shapes of initial curvature, an ideally straight of buckling) is obtained, and that the standard skewness is equal to zero (histogram is symmetrical) [10]. The standard deviation can be calculated, based on assumption that 95% of random observations lie within the tolerance limits of the standard EN 10034. The knowledge on standard kurtosis is lacking completely, therefore the standard kurtosis is considered as a fuzzy number.

Table 1. Input random imperfections.

Symbol	Value	Density	Mean	Standard deviation
h	Cross–section height	Histogram	220.22 mm	0.975 mm
b	Flange width	Histogram	111.49 mm	1.093 mm
t_1	Web thickness	Histogram	6.225 mm	0.247 mm
t_2	Flange thickness	Histogram	9.136 mm	0.421 mm
E	Modulus of elasticity	Gauss	210 GPa	12.6 GPa
f_y	Yield Strength	Histogram	297.3 MPa	16.8 MPa
e_0	Initial curvature	Hermite	0	–

For modelling $e_{0,}$ the Hermite four-parametric probability density function was chosen, the parameters of which are mean value, standard deviation, standard skewness and standard kurtosis. The kurtosis is given as a symmetric fuzzy number, see Fig. 1. Standard deviation is designated on the assumption that 95% of the realizations of the amplitude of initial imperfection e_0 are found within the tolerance limits ⟨-3.15 mm; 3.15 mm⟩ of the standard EN 10034. As the standard kurtosis is a fuzzy number, also the standard deviation is a fuzzy number, see Fig. 1. The fuzzy number of standard deviation e_0 was evaluated using the general extension principle [11, 12].

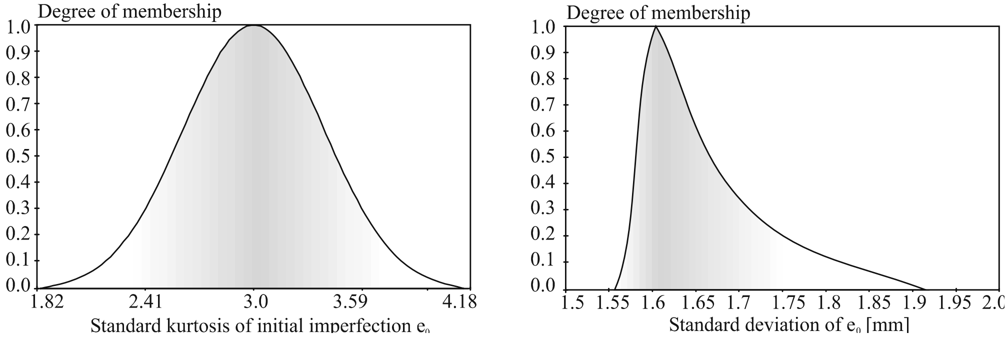

Fig. 1. Fuzzy numbers of standard kurtosis and standard deviation of e_0.

2.4. Fuzzy stochastic analysis of reliability

The reliability assessment was evaluated using the reliability index β according to Comell, defined as $\beta = m_G/S_G$, where m_G is average value, and S_G is standard deviation of the random quantity G in (3). The reliability index β is related to P_f by $P_f = \Phi(-\beta)$, where Φ is the cumulative distribution function of the standardized Normal distribution [7]. In effect, it was proceeded so that the realizations of standard kurtosis were evaluated on behalf of the so-called α-cuts. Twenty cuts of the so-called α-cut method were utilized. A closed interval of standard kurtosis forms a pair with each α-cut. One value of the realization of standard kurtosis (end point of closed interval) forms a pair with one value of standard deviation of the Hermite probability density function of e_0. As soon as the Hermite probability density function of e_0 is known, so all the random quantities in Table 1 are known, and reliability index β can be calculated. Reliability index β was calculated using 500 values of the numerical simulation method Latin Hypercube Sampling [13, 14]. The result is the fuzzy number of β. This process is repeated for $\delta = 0, 0.1, \ldots, 1$.The fuzzy number for β is presented in Fig. 2.

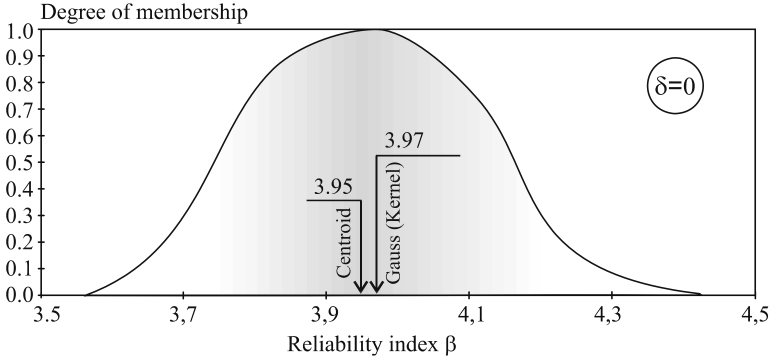

Fig. 2. Membership function of fuzzy reliability index β for $\delta = 0.0$.

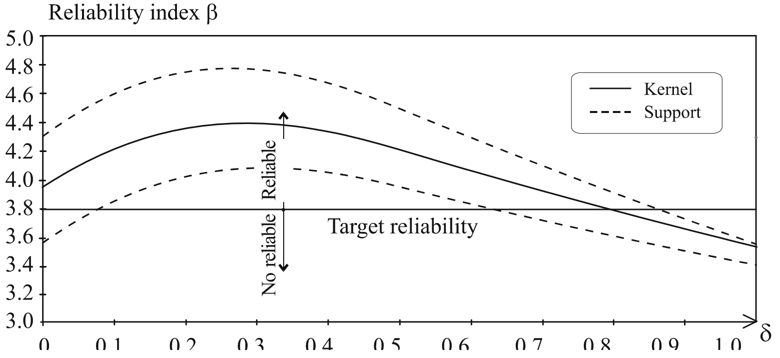

Fig. 3. Support and kernel of fuzzy reliability index β.

3. Conclusion

The results of the studies point out to misalignment of reliability index β. The low value of β means low reliability of the design according to EUROCODE 3. Very low values β were obtained for $\delta = 0$ and $\delta = 1$. The fuzzy numbers β were obtained for fixed values $\delta = 0, 0.1, \ldots, 1$. The high fuzzy uncertainty of reliability index β is evident. The fuzzy uncertainty β was caused by the fuzzy uncertainty of kurtosis of the random amplitude of initial curvature e_0. The problem solved demonstrates the proportion of fuzzy and stochastic uncertainties concerning the reliability of one member. Fuzzy uncertainties of input data, and of calculation processes can predominate the stochastic uncertainties substantially, if a complicated structure with numerous members is considered. If the fuzzy uncertainties are significant, the concentration on the reliability analysis with application of probabilistic methods only can be insufficient.

Acknowledgment

The article was elaborated within the framework of projects of FAST-S-15-2913.

References

[1] J. Melcher, Z. Kala, M. Holický, M. Fajkus and L. Rozlívka. Design Characteristics of Structural Steels Based on Statistical Analysis of Metallurgical Products. *Journal of Constructional Steel Research*, Vol. 60, No. 3–5, 2004, pp. 795–808.

[2] J. Gottvald and Z. Kala. Sensitivity Analysis of Tangential Digging Forces of the Bucket Wheel Excavator SchRs 1320 for Different Terraces. *Journal of Civil Engineering and Management*, Vol. 18, No. 5, 2012, pp. 609–620.

[3] A. Taras and R. Greiner. New Design Curves for Lateral-torsional Buckling-Proposal Based on a Consistent Derivation. *Journal of Constructional Steel Research*, Vol. 66, No. 5, 2010, pp. 648–663.

[4] C. Rebelo, N. Lopes, L. Simões da Silva, D. Nethercot, and P.M.M. Vila Rea. Statistical Evaluation of the Lateral-torsional Buckling Resistance of Steel I-beams, Part 1: Variability of the Eurocode 3 resistance model. *Journal of Constructional Steel Research*, Vol. 65, 2009, pp. 818–831.

[5] Z. Kala. Stability Problems of Steel Structures in the Presence of Stochastic and Fuzzy Uncertainty. *Thin-Walled Structures*, Vol. 45, No. 10–11, 2007, pp. 861–865.

[6] EN 1993-1-1, Eurocode 3: Design of Steel Structures. Part 1-1. General Rules and Rules for Buildings. CEN, Brussels, 2004.

[7] EN 1990, Eurocode-Basic of Structural Design. CEN, Brussels, 2002.

[8] Z. Kala. Sensitivity Assessment of Steel Members under Compression. *Engineering Structures*, Vol. 31, No. 6, 2009, pp. 1344–1348.

[9] G.C. Soares. Uncertainty Modelling in Plate Buckling. *Structural Safety*, Vol. 5, No. 1, 1988, pp. 17–34.

[10] Z. Kala. Elastic Lateral-torsional Buckling of Simply Supported Hot-rolled Steel I-beams with Random Imperfections. *Procedia Engineering*, Vol. 57, pp. 504–514.

[11] L.H. Zadeh. Fuzzy Sets. *Information and Control*, Vol. 8, No. 3, 1965, pp. 338–353.

[12] B. Möller and U. Reuter. *Uncertainty Forecasting in Engineering*. Springer Press, 2007, 202 p.

[13] M.D. McKey, W.J. Conover, and R.J. Beckman. A Comparison of the Three Methods of Selecting Values of Input Variables in the Analysis of Output from a Computer Code. *Technometrics*, Vol. 21, No. 2, 1979, pp. 239–245.

[14] R.C. Iman and W.J. Conover. Small Sample Sensitivity Analysis Techniques for Computer Models with an Application to Risk Assessment. *Communications in Statistics – Theory and Methods*, Vol. 9, No. 17, 1980, pp. 1749–1842.

Study of the ultrafine-grains intrinsic nanostructure refinement by severe plastic deformation of copper alloys

Lembit Kommel[1], Renno Veinthal[2], Valdek Mikli[3], Andrei Dedov[4]

Department of Materials Engineering
Tallinn University of Technology
Tallinn, Estonia
[1]*lembit.kommel@ttu.ee,* [2]*renno.veinthal@ttu.ee,*
[3]*valdek.mikli@ttu.ee,* [4]*andrei.dedov@ttu.ee*

Abstract. This article presents our take on the area of ultrafine-grains (UFG) intrinsic nanomeasures pillars production by severe plastic deformation (SPD) and this effect on properties of CuCrS energy alloy. The nanaomeasures pillars inside of ultra-fine grains are prepared by equal channel angular pressig (ECAP) with additional hard cyclic viscoplastic deformation (HCVD) and tension loading. These structural formings in the UFG microstructure were studied by TEM and SEM investigations. With compare to conventional UFG structure this material shows increased plasticity but lowered tensile strength and hardness. The tribological testing in sliding contact metal-graphite disk under electric current show that the wear resistance was increased or wear rate decreased significantly by increased hardness, dislocation density and wear testing parameters (current density and normal compression stress) stability. The effect of optimized thermo-mechanical processing parameters and strain amplitude as well cycles number at HCVD on the UFG intrinsic nanaostructure and strength of CuCrS energy alloy is investigared.

Keywords: *ultrafine-grained microstructure, nanopillars, electrical conductivity, wear resistance.*

1. Introduction

Bulk poycrystalline metals and alloys microstructure is a key factor which determine the mechanical, physical, chemical and tribological properties in surrounding media. A brief overview of the severe plastic deformation (SPD) processes available at present is given in [1]. The scientific grounds and techniques for metallic materials processing through a combination of high hydrostatic pressure and simple shear deformation were worked out by P.W. Bridgman [2]. It is a well-known, that the grain refinement effect on properties of polycrystalline metals is more pronounced at low temperatures. The materials with UFG or nanocrystalline (NC) microstructure, processed via SPD techniques have high hardness and tensile strength immediately after processing but these superior strength properties are not stabile by time and temperature increase [1, 3–5]. Unfortunately, such UFG and easy NC materials electrical conductivity is lower than coarse grained (CG) materials have [6–8]. For improve of strength and electrical conduction properties concurrently the suitable heat treatment [6–7] or thermo-mechanical working [8] can be used. The electrical conduction is possible to increase via suitable microstructure processing by use of the hard cyclic viscoplastic deformation (HCVD) at optimized stress-strain loadings [9]. By this method the electrical conductivity of commercially pure copper was increased up to 103% IACS, but the tensile strength, hardness and Young’s module were decreased slightly. The diffusion-controlled phase transformation of Zr – Nb alloys (for energy production) take place in as-cast alloy and by diffusionless mechanism in severely deformed by high pressure torsion (HPT) nanocrystalline alloy at effective temperature of 700 °C [10]. After SPD the radiation tolerance was increased. By this the phase transition during HPT of $\mathrm{Cu}-\mathrm{Co}$ alloys led to increase of the Co particles dissolution in pure Cu matrix [11]. The grain boundary (GB) films phenomena in Al-Zn alloys at HPT is studied in [12, 13]. The formation of GB films and layers give to UFG metals and $\mathrm{Al}-\mathrm{Zn}$ alloys unique plastic as well superductility properties.

2. Problem formulation

The materials for electrical and electronic industries can have combination with both high strength and electrical conductivity (for wires and cables) and good wear resistance (for electrical contact materials). In works [5–7] is sown that electrical conductivity correlated with hardness and in works [8, 9] is shown that the electrical conductivity depend on dislocation density but not only at hardness. For receive materials with high strength and good electrical properties is the challenging for scientists in the field of materials engineering as well as materials science. In this work, we are developing a new method for intrinsic nanostructure formation in view of nanopillars in UFG-s. Such material has high electrical conductivity, good mechanical strenght and hardness as well superior wear resistance under electrical current conduction on sliding surface of alloy with graphite disk.

2.1. Problem dissolve

It is known that SPD processing accompanies with thermo-mechanical processing is the key for receive such desirable materials for electrical and electronic industries. For optimize of the mechanical, physical, chemical and tribological proprties of the SPD processed UFG and NC materials the suitable heat treatment can be used [6–8]. In this study for materials testing and properties optimization we used samples from $\mathrm{Cu}-0.68\mathrm{Cr}-0.02\mathrm{S}$ energy alloy for electrical industry use. This alloy after castin in purified argon environment and forged at 800 °C was heat treated for microstructure recrystallization at 1000 °C for 2 h with water quencing and at follows was send to ECAP for 6 passes by B_c route. Arfter ECAP the tension compression samples were cut off and at follows worked by HCVD.

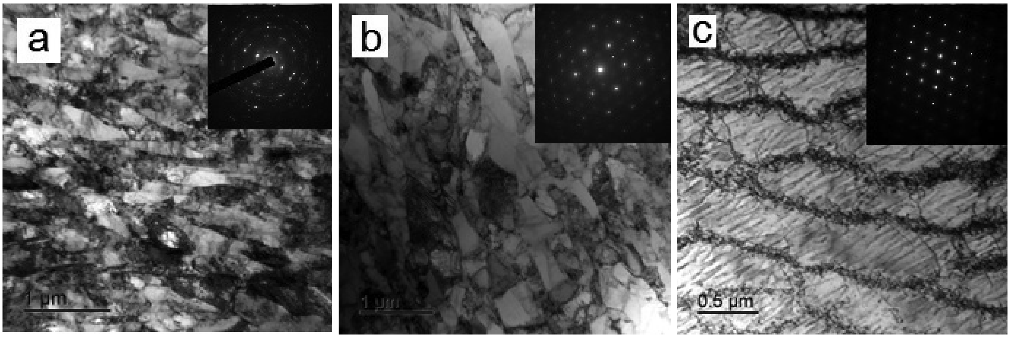

Fig. 1. UFG microstructure of CuCrS alloy processed by ECAP for 6 passes by Bc route (a), processed by ECAP+HCVD for 5 test series at strain amplitudes of $\pm 0.2\%, \pm 0.5\%, \pm 1.0\%, \pm 1.5\%$, and $\pm 2.0\%$ for 20 cycles, respectively (b) and HCVD processed at 5 test series at strain amplitudes of $\pm 0.2\%, \pm 0.5\%, \pm 1.0\%, \pm 1.5\%$, and $\pm 2.0\%$ for 20 cycles, respectively (c).

Three sampes were worked by HCVD without prliminary working by ECAP. In TEM pictures (Fig. 1.) is shown UFG microstructures after ECAP (a), after ECAP followed HCVD (b) and after HCVD (c) only.

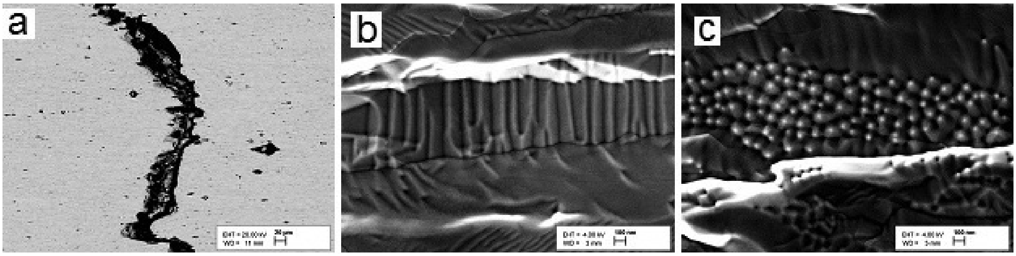

Fig. 2. SEM microgrphs showing the microcracks forming in the necking region of UFG alloy after ECAP+HCVD and followed tension (a). The nanopillars in longitudinal (b) and in srocc-section (c) in UF grains are shown.

In SEM pictures (Fig. 2) is shown the microcrack in necking region crossed with tension test sample longitudinal axis (a). Near this zone the formed nanaomeasures pillars were formed, which are oriented in longitudinal (b) and in cross-section (c) to the UF grains. Before microstructure study by SEM the diamond grounded surface was worked by Precision Etching Coated System at 9 kV and 400 mA for 30 minutes. As is shown in SEM pictures (Fig. 2b, Fig. 2c) the pillars diameter is lower then 100 nm and their length is about 700 − 800 nm. The pillars situated parallel to each other in the UF grains which are presented in Fig. 1b. In (Fig. 3a) TEM image showing featureless wetting layer [12, 13] wich gives unique plastic behavior for high strength material. UFG microstructure, studied by SEM-EDS (Fig. 3b) shows the nanosizes Cr and S particles in the Cu matrix. The Cr particles sizes were about ∼50 nm and maximal size was hot higher then ∼100 nm. For comparison, in as-cast alloy [8] the Cr particles in Cu matrix have dimensiona about ∼1 μm. Such particle size decreasing during SPD processing via diffusion induced phase transformation is described in works [10, 11]. The ECAP processed samples for micro-mechanical properties, electrical conductivity as well wear testing were subjected to heat treatment with step of 100 ℃ at temperatures up to 850 ℃ for 1 h. The HCVD samples were not heat treated and were tested for wear rate immediately after processing.

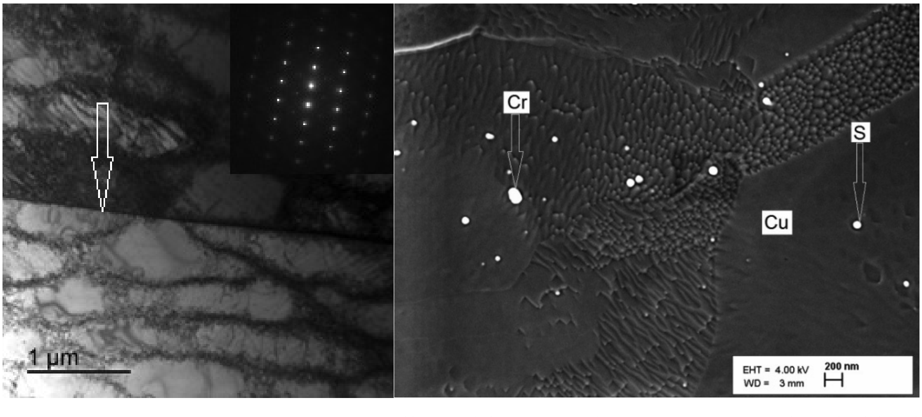

Fig. 3. TEM picture of HCVD CuCrS alloy with UFG microstructure (a) devided by layer and SEM picture (b) shows the nanosizes Cr and S particles in the Cu matrix.

The results of wear rate study are presented in graph (Fig. 4a) up to 650 ℃ only as the wear rate of samples heated at 750 ℃ and 850 ℃ were about 10–15 times higher and these results are not shown in graphic. The wear rate of samples after ECAP (20) and ECAP followed HCVD sample 20(H) (see Fig. 4a) have wery large difference, about 2 times. It means, that UFG microstructure with nanaopillars in UF grains increase wear resistance of material. In graphic (Fig. 4b) are present results of ECAP processed UFG Cu alloy hardness and electrical conductivity evolution during heat treatment. As is shown in graphic the ECAP processed samples have maximal hardness but minimal electrical conduction at 20 ℃. By increase heat treatment temperature the hardness took decrease and electrical conductivity increase and receive the maximal electrical conduction at 450 ℃ [5–8]. The maximal electrical conductivity has CuCr alloy after ECAP followed heat treatment [8] and it was 93.4% IACS. The maximal ultimate tensile strength of 790–840 MPa and electrical conductivity of 81– 85% IACS for CuCr alloy was receiv in [7]. In the present study the tension strength was studied on large samples with stepped cross-section areas by INCTRON and on minisamples with lengt of 12,5 mm which were cut off from large samples after HCVD processing. The minisamples were tested by Tension System Mechmesin MDD MK2 Stand at tension speed of 0.4 mm/min. The results (Fig. 4c) shows that the tension stress was maximal after ECAP withou heat treatmen procedures. At followed heat treatment the tensile strength was decreased and elongation increased. The Young module was maximal for ECAP+HCVD samples (N7, N1, N5) and decreased in samples after heat treatment.

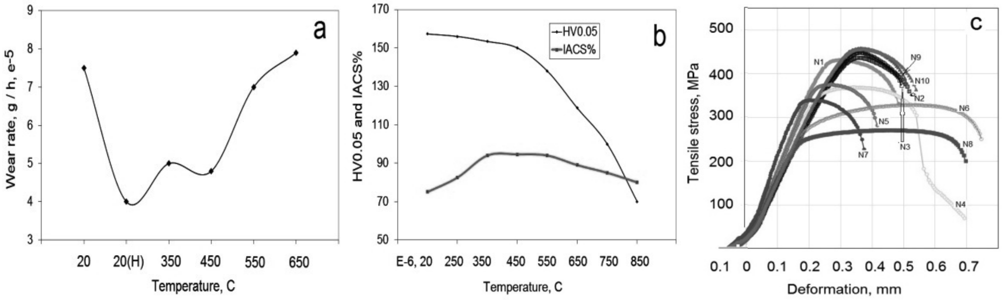

Fig. 4. Wear rate (a), hardness v. electrical conductivity (b) and tensile stress (c) dependence from heat treatment temperature and thermomechanical processing parameters of CuCrS energy alloy. In (c) ECAP (N2, N9, N10), ECAP+HCVD (N1, N4, N5, N7) and heat treated samples (N6, N8) tensile stress for deformation in mm on test part length of 2.5 mm.

2.2. Conclusions

The microstructure of the $\mathrm{Cu}-0.68\mathrm{Cr}-0.2\mathrm{S}$ alloy processed by ECAP, ECAP+HCVD and HCVD only was characterized by TEM and SEM.

Nano-pillars having dimeters lower then ~ 100 nm and heights of $\sim 700-800$ nm. The nanaopillars were prepared by HCVD in the ECAP processed alloy near fracture microcrack formed.

The wear resistance was maximal in the samples with nano-pillars in UF grains. Wear rate increase with material hardness decrease as well during electrical sarks forming by normal load (compression stress) decrease.

The tested alloy electrical conductivity was ~94% IACS and tensile strength was ~450 MPa, respectively.

At follows the micromechanical properties of nanopillars we plan to investigate via nanaoindentation by AFM use.

References

[1] Y. Estrin and A. Vinogradov. Extreme grain eefinement by severe plastic deformation: A wealth of challenging science. *Acta Materialia*, Vol. 61, 2013, pp. 782–817.

[2] P.W. Bridgman. On Torsion Combined with Compression. *Journal of Applied Physics,* Vol 14, 1943, pp. 273–283.

[3] L. Kommel, E. Kimmari, M. Saarna and M. Viljus. Processing and properties of bulk ultrafine-grained pure niobium. *Journal of Materials Science*, Vol. 48, No. 13, 2013, pp. 4723–4729.

[4] O.F. Higuera-Cobos, J.A. Berrios-Ortiz and J.M. Cabrera. Texture and fatigue behavior of ultrafine grained copper produced by ECAP. *Materials Science & Engineering,* A 609, 2014, pp. 273–282.

[5] D.V. Shangina, N.R. Bochvar and S.V. Dobatkin. The effect of alloying with hafnium on the thermal stability of chromium bronze after severe plastic deformation. *Journal of Materials Science*, Vol. 47, No. 22, pp. 7764–7769.

[6] K.X. Wei, W. Wei, F. Wang, Q.B. Du, I.V. Alexandrov and J. Hu. Microstructure, mecanical properties and electrical conductivity of industrial Cu-0.5%Cr alloy processed by severe plastic deformation. *Materials Science & Engineering,* A 528, 2011, pp. 1478–1484.

[7] R.K. Islamgaliev, K.M. Nesterov, J. Bourgon, Y. Champion and R.Z. Valiev. Nanostructured Cu-Cr alloy with high strength and electrical conductivity. *Journal of Applied Physics,* Vol. 115, 2014, pp. 194301–1943014.

[8] L. Kommel, and A. Pokatilov. Electrical conductivity and mechanical properties of Cu-0.7wt% Cr and Cu-1.0wt% Cr alloys processed by severe plastic deformation. *Material Science & Engineering*, Vol. 63, 2014, pp. 0121691–0121697.

[9] L. Kommel. Properties development of ultrafine-grained copper under hard cyclic viscoplastic deformation. *Materials Letters*, Vol. 64, 2010, pp. 1580–1582.

[10] B.B. Straumal, A.S. Gornakova, A.A. Mazilkin, O.B. Fabrichnaya, M.J. Krigel, B. Baretzky, J.-Z. Jiang, and S.V. Dobatkin. Phase transformation in the severely plastically deformed deformed Zr-Nb alloys. *Materials Letters*, Vol. 81, 2012, pp. 225–228.

[11] B.B. Straumal, A.R. Kilmametinov, Y. Ivanisenko, L. Kurmanaeva, B. Baretzky, Y.O. Kucheev, P. Zieba, A. Korneva and D.A. Molodov. Phase transition during high pressure torsion of Cu-Co alloys. *Materials Letters*, Vol. 118, 2014, pp. 111–114.

[12] N.Q. Chinh, R.Z. Valiev, X. Sauvage, G. Varg, K. Havancsak, M. Kawasaki, B.B. Straumal and T.G. Langdon. Grain boundary phenomena in a ultrafine-grained Al-Zn alloy with improved mechanical behavior for micro-devices. *Advanced Engineering Materials*, Vol. 16, No. 8, 2014, pp. 1000–1009.

[13] B.B. Straumal, X. Sauvage, B. Baretzky, A.A. Mazilkin and R.Z. Valiev. Grain boundary films in Al-Zn alloys after high pressure torsion. *Scripta Materialia*, Vol. 70, 2014, pp. 59–62.

Stability of two-stepped beams with cracks

Tiina Kraav[1], **Jaan Lellep**[2]

Institute of Mathematics, University of Tartu
Tartu, Estonia
[1]*tiina.kraav@ut.ee*, [2]*jaan.lellep@ut.ee*

Abstract. A stability analysis is developed for two-stepped beams subjected to the axial pressure. The beams under consideration are elastically fixed at the end with loading and pinned or clamped at the root section. The elastic supports are located at the intermediate cross sections as well. It is assumed that the cross sectios where the thickness changes rapidly are weakened by cracks or crack-like defects. The influence of cracks on the buckling load is modelled by the method of distributed line springs. Numerical results are presented for two-stepped cantilevers elastically fixed at the loaded end.

Keywords: *beam, stability, crack, elasticity, line spring.*

1. Introduction

The problem of stability of structural elements is an essential problem not only in the structural mechanics but in the various branches of technology.

During their exploitation structural elements often have cracks and crack-like defects which should be taken into account when assessing the strength or the stability of the whole structure.

The stability of cracked member was studied by Chondros, Dimarogonas, Yao [1], Skrinar [7], Li [6] making use of the "massless rotational spring method". This method was successfully employed by many investigators for studying beams, plates and shells with defects. In the previous paper the authors have studied the stability of elastically supported cantilever beams with cracks [4] and the critical buckling load of a beam resting on an elastic foundation [3].

In the present paper a buckling analysis will be developed for the investigating of the influence of cracks on the critical buckling of two-stepped beams. The beams are clamped at one end and elastically fixed at the another end. The elastic supports can be located at the intermediate cross sections as well.

2. Formulation of the problem

A stepped beam subjected to the axial pressure load P is studied. It is assumed that the beam has rectangular cross sections of constant width b whereas the other dimension h called height is piece wise constant (Fig. 1). We will study the case

$$h = \begin{cases} h_0, & x \in (0, a_1), \\ h_1, & x \in (a_1, a_2), \\ h_2, & x \in (a_2, l) \end{cases} \tag{1}$$

in the greater detail. Here the $0x$-axis coincides with the axis of undeformed beam, the origin of coordinates being at the fixed end. The end of the beam where $x = 0$ is simply supported or clamped whereas the other end $(x = l)$ is elastically supported. Elastic

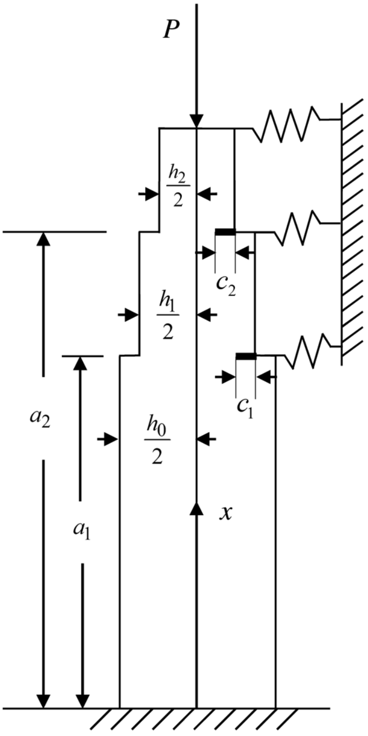

Fig. 1. A two-stepped beam.

supports are located at $x = a_1$ and $x = a_2$, as well. The rigidities of these supports are μ_1, μ_2 and μ, respectively. Evidently, the case $\mu_i = 0$ corresponds to the case where the support at $x = a_i$ is lacking.

It is assumed that at the cross sections $x = a_i$ $(i = 1, 2)$ where the height of the cross section changes rapidly defects or cracks of depth c_i are located. These cracks are treated as flaws, no attention will be paid to the extension of cracks.

The aim of the paper is to elucidate the influence of critical buckling loads on the parameters of cracks whereas the cracks are treated as stable surface cracks.

3. Critical buckling load

Assuming that the material of the beam under consideration is a linear elastic material one can present the equilibrium equation of a beam element as (Farshad [2], Simitses [8], Lellep and Kraav [4])

$$M'' - Pv'' = 0$$

where M is the bending moment and v the displacement in the transverse direction. The Hooke's law furnishes the relation (see [4, 5])

$$M = -EI_jv'' \qquad (2)$$

for $x \in (a_j, a_{j+1})$. Here $I_j = bh_j^3/12$ and E is the Young modulus. Substituting (2) in the equilibrium equation leads to the equation

$$v'''' + \frac{\lambda_j^2}{l^2} v'' = 0 \tag{3}$$

for $x \in (a_j, a_{j+1})$. In (3) the notation

$$\lambda_j = \sqrt{\frac{12Pl^2}{Ebh_j^3}} \tag{4}$$

is introduced. Note that the equation (3) is to be integrated for detached regions (a_j, a_{j+1}). Thus one can present the general solution of (3) for $x \in (a_j, a_{j+1})$ as

$$v = A_j \cos \lambda_j \xi + B_j \sin \lambda_j \xi + C_j \, \xi + D_j \tag{5}$$

where for $j = 0, 1, 2$ and $\xi = x/l$.

The boundary conditions are at $x = 0$

$$v(0) = 0, v'(0) = 0 \tag{6}$$

for clamped end and

$$v(0) = 0, v''(0) = 0 \tag{7}$$

for the simply supported edge. At the another edge one has

$$v''(l) = 0, v'''(l) + \lambda_n^2 v'(l) = \mu v(l). \tag{8}$$

At the cross sections where the thickness h changes rapidly the shear force Q is discontinuous. The jump of the shear force is equal to the reaction of the support. Thus

$$[Q(a_j)] = \mu_j v(a_j) \tag{9}$$

for $j = 1, 2$. According to the equilibrium equations $Q = M'$. In (9) and henceforth the square brackets denote finite jumps of corresponding quantities at the given point. Instead of (9) one can write

$$[EIv'''(a_j)] = \mu_j v(a_j) \tag{10}$$

where $I(a_j + 0) = I_j$ and $I(a_j - 0) = I_{j-1}$.

Due to the continuity of the bending moment one has

$$[EIv''(a_j)] = 0 \tag{11}$$

for $j = 1, 2$.

The influence of cracks on the stability of beams is modeled similarly to that in papers by Lellep and Kraav [3, 4], also Chondros, Dimarogonas, Yao [1].

According to this concept the displacement v is continuous but

$$[v'(a_j)] = 6\pi \overline{h_j} f(s_j) v''(a_j + 0) \tag{12}$$

where $\overline{h_j} = \min(h_j, h_{j-1})$ and

$$\begin{aligned} f(s_j) = 1.86s^2 - 3.95s^3 + 16.37s^4 - 37.23s^5 + 76.81s^6 - 126.9s^7 + 172s^8 \\ -143.97s^9 + 66.56s^{10}. \end{aligned} \tag{13}$$

4. Two-stepped cantilever

Let us consider the case of a two-stepped cantilever beam in a greater detail. Let us assume that the intermediate supports are lacking and that the beam is elastically fixed at $x = l$ and clamped at $x = 0$.

Now $\mu_1 = \mu_2 = 0$ and the set of intermediate conditions can be presented as

$$\begin{gathered}
v(a-0) = v(a+0), \\
v'(a-0) = v'(a+0) - 6\pi\overline{h_2}f(s_1)v''(a+0), \\
\frac{v''(a-0)}{\lambda_0^2} = \frac{v''(a+0)}{\lambda_1^2}, \\
\frac{v'''(a-0)}{\lambda_0^2} = \frac{v'''(a+0)}{\lambda_1^2}, \\
v(b-0) = v(b+0), \\
v'(b-0) = v'(b+0) - 6\pi\overline{h_3}f(s_2)v''(b+0), \\
\frac{v''(b-0)}{\lambda_1^2} = \frac{v''(b+0)}{\lambda_2^2}, \\
\frac{v'''(b-0)}{\lambda_1^2} = \frac{v'''(b+0)}{\lambda_2^2}
\end{gathered} \tag{14}$$

where the notation $a = a_1, b = a_2$ is used.

The appropriate boundary conditions are presented by (6) and (8). The system of equations (6), (8), (14) is a linear homogeneous algebraic system with respect to unknowns A_j, B_j, C_j, D_j $(j = 1, 2, 3)$. The system consists of twelve linear homogeneous equations with determinant Δ. It is known that the system has a non-trivial solution if and only if its determinant vanishes.

However, it is reasonable to use the boundary conditions (7), (8) separately. This enables to eliminate the unknowns

$$\begin{aligned}
D_1 &= -A_1, \\
C_1 &= -\lambda_0 B_1, \\
B_3 &= -A_3\frac{\cos\lambda_2}{\sin\lambda_2}, \\
D_3 &= C_1\left(\frac{\lambda_2^2}{\mu} - 1\right).
\end{aligned} \tag{15}$$

Taking (15) into account one can present the determinant Δ of the system (14) as

$$\Delta= \tag{16}$$

$$\begin{vmatrix}
\cos\lambda_0\alpha - 1 & \cos\lambda_1\alpha & 0 & \sin\lambda_0\alpha - \lambda_0\alpha & -\sin\lambda_1\alpha & -\alpha & 0 & -1 \\
0 & \cos\lambda_1\beta & -\dfrac{\sin\lambda_2(1-\beta)}{\sin\lambda_2} & 0 & \sin\lambda_1\beta & \beta & 1-\beta-\dfrac{\lambda_2^2}{\mu} & 1 \\
\lambda_0\sin\lambda_0\alpha & \begin{matrix} k\lambda_1^2\cos\lambda_1\alpha - \\ \lambda_1\sin\lambda_1\alpha \end{matrix} & 0 & -\lambda_0\cos\lambda_0\alpha + \lambda_0 & \begin{matrix} k_1\lambda_1^2\sin\lambda_1\alpha + \\ \lambda_2\cos\lambda_1\alpha \end{matrix} & 1 & 0 & 0 \\
0 & \lambda_1\sin\lambda_1\beta & \begin{matrix} \dfrac{k_2\lambda_2^2\sin\lambda_2(1-\beta)}{\sin\lambda_2} - \\ \dfrac{\cos\lambda_2(1-\beta)}{\sin\lambda_2} \end{matrix} & 0 & -\lambda_1\cos\lambda_1\beta & -1 & 1 & 0 \\
\cos\lambda_0\alpha & -\cos\lambda_1\alpha & 0 & \sin\lambda_0\alpha & -\sin\lambda_1\alpha & 0 & 0 & 0 \\
0 & \cos\lambda_1\beta & -\dfrac{\sin\lambda_2(1-\beta)}{\sin\lambda_2} & 0 & \sin\lambda_1\beta & 0 & 0 & 0 \\
\lambda_0\sin\lambda_0\alpha & -\lambda_1\sin\lambda_1\alpha & 0 & -\lambda_0\cos\lambda_0\alpha & \lambda_1\cos\lambda_1\alpha & 0 & 0 & 0 \\
0 & \lambda_1\sin\lambda_1\beta & -\dfrac{\lambda_2\cos\lambda_2(1-\beta)}{\sin\lambda_2} & 0 & -\lambda_1\cos\lambda_1\beta & 0 & 0 & 0
\end{vmatrix}$$

Here the notation

$$k_j = 6\pi \bar{h}_j f(s_j) \tag{17}$$

is used.

5. Numerical results and discussion

The equation $\Delta = 0$ is solved numerically with respect to the critical buckling load P. It easily follows from (4) that

$$\lambda_j = \lambda_0 \frac{h_0^3}{h_j^3} \tag{18}$$

for $j = 1, 2$. Thus it is sufficient to determine only one eigenvalue, for instance, λ_0. The others can be calculated via λ_0.

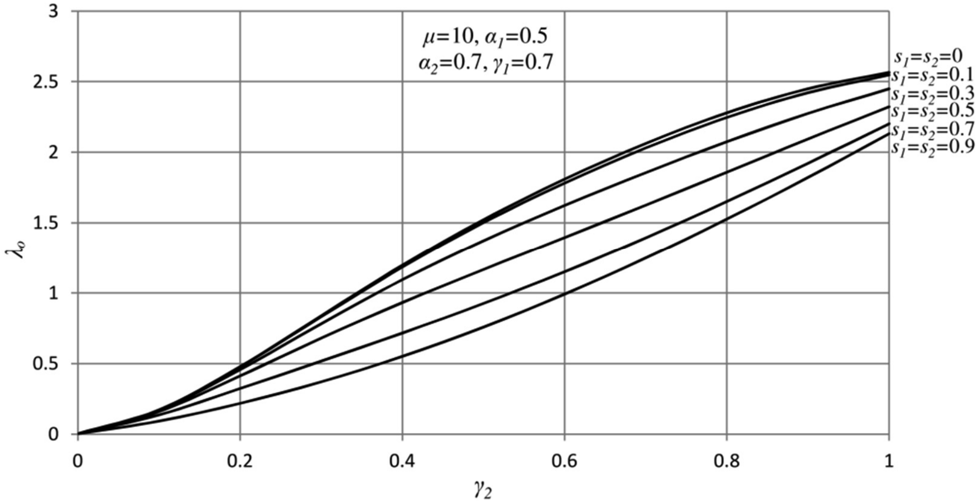

Fig. 2. Buckling of a two-stepped beam.

The results of calculations are presented in Fig. 2–3. In Fig. 2 the relationships between λ_0 and the thickness $\gamma_2 = h_2 / h_0$ is shown for different values of the crack length s. Here $s = s_1 = s_2$, $a_1 = 0.5l$, $a_2 = 0.7l$, $\mu = 10$ and $h_1 = 0.7h_0$. It can be seen from Fig. 2 that the critical buckling load (the eigenvalue λ_0) monotonically increases together with the thickness γ_2, as might be expected. It also reveals from Fig. 2 that the shorter is the crack the higher is the value of the critical buckling load for each value of γ_2.

Calculations carried out showed that in the case where $a_1 = a_2$ the obtained results concerning one-stepped beams in the case $\mu = 0$ (see Lellep, Kraav [4], Lellep, Sakkov [5]).

Similar results are presented for $a_1 = 0.3l$, in Fig. 3. Here $a_2 = 0.7l$, $\mu = 10$ and $h_1 = 0.7h_0$.

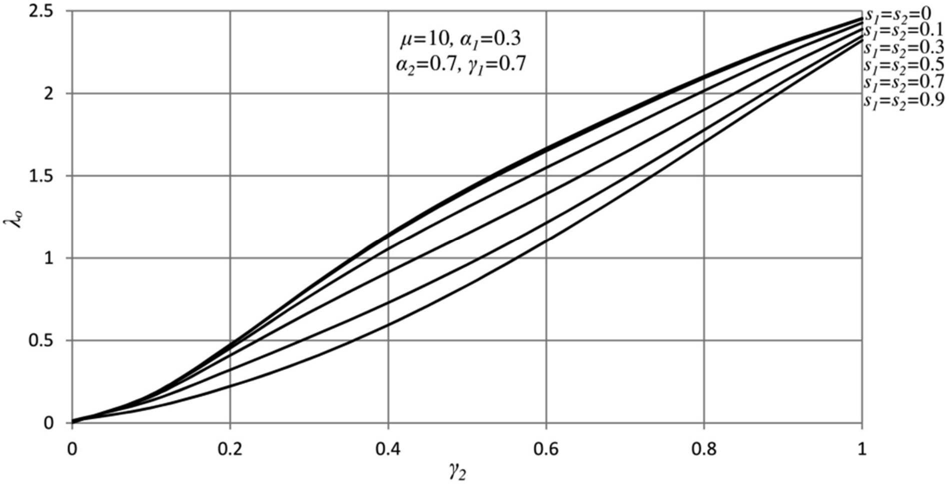

Fig. 3. Buckling of a two-stepped beam.

6. Concluding remarks

The stability of elastic beams and columns was studied. The beams under consideration have stepped cross section and are weakened by cracks or crack-like defects. The method developed above is applicable for beams with various end conditions. The case where one end of the beam is clamped and the other elastically supported is studied in a greater detail. It was shown that the obtained results coincide with earlier results if the stiffness of the support at the loaded edge tends to zero, as might be expected.

Acknowledgements

The supports from the grant No. 9110 “Optimization of structural elements” and from the Institutional Research Funding IUT20-57 of the Ministry of Education and Research of Estonia are gratefully acknowledged.

References

[1] T.J. Chondros, A.D. Dimarogonas and J. Yao. Vibration of a beam with a breathening crack. *Journal of Sound and Vibration*, Vol. 239, 2001, pp. 57–67.

[2] M. Farshad. *Stability of Structures*. Elsevier, 1994, 425 p.

[3] T. Kraav and J. Lellep. Buckling of beams and columns on elastic foundation. *In: Lellep, J. Puman, E. (Ed-s) Optimization and Analysis of Structures*, Tartu, 2013, pp. 52–58.

[4] J. Lellep and T. Kraav. Elastic buckling of stepped beams with cracks. *Recent Researches in Hydrology, Geology and Continuum Mechanics*, WSEAS, Cambridge, 2011, pp. 11–16.

[5] J. Lellep and E. Sakkov. Buckling of stepped composite columns. *Mechanics of Composite Materials,* Vol. 42, No. 1, 2006, pp. 63–72.

[6] Q.S. Li. Buckling of multi-step non-uniform beams with elastically restrained boundary conditions. *Journal of Constructional Steel Researche*, Vol. 57, 2001, pp. 753–777.

[7] M. Skrinar. On critical buckling load estimation for slender transversely cracked beam-columns by the application of a simple computational model. *Computational Materials Science*, Vol. 43, 2008, pp. 190–198.

[8] G.J. Simitses. *An Introduction to the Elastic Stability of Structures.* Prentice-Hall, INC., 1976, 253 p.

Extension of Kübler's model for analysis of growth stresses in tree disc

Jakub Kõo[1], **Jaak Valgur**[2]

Estonian University of Life Sciences
Tartu, Estonia
[1]*jakub.koo@emu.ee,*

Abstract. The layer growing/removing method for determination of residual stresses in orthotropic non-homogeneous discs has been applied as an extension of Kübler's model for analysis of growth stresses in the tree disc. The extended model permits to take account of the orthotropic characteristics and the layered structure of the tree disc. As an illustrative example, growth stresses are calculated in a disc of spruce wood from initial (maturation) stress measured on its free outer surface.

Keywords: *residual stress, orthotropic non-homogeneous disc, layer growing/removing method, growth stresses in tree disc, Kübler's model.*

1. Introduction

Growth stresses are stresses that develop in the wood of growing plants. Growth stresses are residual stresses, which means that they are not caused by external forces, e.g. by the wind load. Growth stresses are initiated in the cambium as it adds each new layer of wood to the stem. There is no consensus about how exactly growth stresses are generated. The two main hypotheses are the hypothesis of lignin swelling [11] and the hypothesis of cellulose tension [3]. The former hypothesis states that deposition of encrusting lignin between cellulose fibrils causes the transverse expansion of wood cells; the latter hypothesis states that tensile stresses arise from the contraction of cellulose in the process of maturation.

Growth stresses act both to prestress tree stems in order to increase their resistance to bending moments caused by external forces and self-weight [8], [9], as well as to reorient stems and branches [1]. High levels of growth stresses are implicated in end splitting of logs, deflection at sawing and deformation of boards as they are released during sawing operations. For predicting growth stresses from experimentally measured natural frequencies of a tree disc, it is necessary to know the effects of the stresses [5]. Thus, growth stress analysis would have both scientific and technological significance.

Several analytical models have been developed in order to calculate growth stresses in the stem at the local level. Among them the most commonly quoted one is the model of Kübler [1], [6], [8]–[10], in which radial and circumferential growth stresses in a tree disc can be written in the form

$$\sigma_{r2} = \bar{\sigma}_{\theta 2} \ln \frac{r}{r_2}, \qquad \sigma_{\theta 2} = \bar{\sigma}_{\theta 2} \left[1 + \ln \frac{r}{r_2} \right], \tag{1}$$

where $\bar{\sigma}_{\theta 2}$ is constant peripheral initial (maturation) circumferential stress. The distance from the pith is denoted by r and the radius of disc, by r_2.

Note that growth stresses cannot be measured directly, whereas strains are comparatively easy to asses. As stresses near tree surface are within the proportional limit of elasticity, they can be calculated from measured strains. For this reason, initial stresses in Kübler's equations (1) are sometimes expressed in terms of directly measurable initial (maturation) strains [6].

It is not difficult to establish analogy between Kübler's equations and more common equations of the layer growing/removing method for determination of residual stresses in orthotropic non-homogeneous discs [7]. In the present study such analogy is used for the extension of Kübler's model in terms of taking account of the layered structure and orthotropic characteristics of the tree disc.

2. An extension of Kübler's model

Following the generalized algorithm of layer growing/removing methods for discs [7], consider a thin layer growing on the outer contour of a multilayered disc with a central hole (Fig. 1). Let the number of the initial layers be k, the radius of the free stationary contour r_0, and the radius of the interface of the initial and growth regions r_k. The layers are numbered starting from the layer adjacent to the free surface of the initial region, in the direction of growth. Let the total number of disc layers be n and the radius of the free contour of the growth region r_n. Polar coordinates r, θ are used.

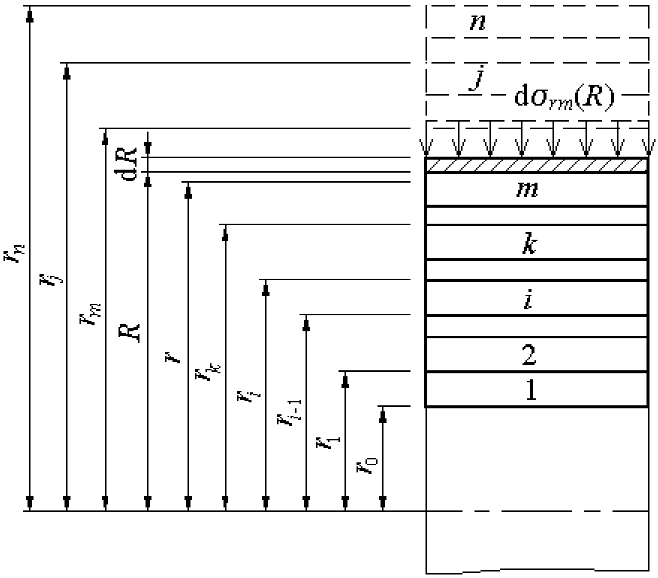

Fig. 1. Layer-growing on the outer contour of a multilayered disc.

According to the generalized algorithm, residual stresses in the layer m of the coating can be calculated as the sum of initial and additional stresses:

$$\sigma_{\theta m}(r) = \bar{\sigma}_{\theta m}(r) + \sigma^{*}_{\theta m(m)}(r) + \sum_{j=m+1}^{n} \sigma^{*}_{\theta m(j)}(r),$$
$$\sigma_{rm}(r) = \sigma^{*}_{rm(m)}(r) + \sum_{j=m+1}^{n} \sigma^{*}_{rm(j)}(r), \qquad (2)$$
$$m = k+1, k+2, \ldots, n,$$

where $\bar{\sigma}_{\theta m}(r)$ is initial circumferential stress in the layer m, and $\sigma^*_{rm(\ )}(r)$ and $\sigma^*_{\theta m(\ )}(r)$ are additional stresses in the layer m, arising during the growth of this layer (index (m)) or in any successive layer j (index (j)).

Initial (maturation) stress $\bar{\sigma}_{\theta m}(r$ in the differential surface layer dR and the additional stresses $\sigma^*_{rm(m)}(r)$ and $\sigma^*_{\theta m(m)}(r)$ can be expressed by strain $\tilde{\varepsilon}_{\theta 1(m)}(r_0, r)$ measured on the stationary surface $(r = r_0)$ as follows:

$$\bar{\sigma}_{\theta m}(r) = \frac{E_{\theta 1}}{2}\frac{a_m r^{2k_m} - b_m}{r^{k_m}}\frac{d\tilde{\varepsilon}_{\theta 1(m)}(r_0, r)}{dr}, \tag{3}$$

$$\begin{aligned} \sigma^*_{rm(m)}(r) &= \frac{E_{\theta 1}}{2}\left(a_m r^{k_m - 1} - b_m r^{-k_m - 1}\right)\tilde{\varepsilon}_{\theta 1(m)}(r_0, r), \\ \sigma^*_{\theta m(m)}(r) &= \frac{k_m E_{\theta 1}}{2}\left(a_m r^{k_m - 1} + b_m r^{-k_m - 1}\right)\tilde{\varepsilon}_{\theta 1(m)}(r_0, r), \end{aligned} \tag{4}$$

where

$$\tilde{\varepsilon}_{\theta 1(m)}(r_0, r) = \varepsilon_{\theta 1(m)}(r_0, r_m) - \varepsilon_{\theta 1(m)}(r_0, r)$$

is the change of the circumferential strain measured on the free contour of the initial region $(r = r_0)$ during the growth of the layer m in the interval $r \le R \le r_m$.

Constants a_m and b_m in equations (3) and (4) are calculated recurrently:

$$\begin{aligned} a_1 &= k_1^{-1} r_0^{1-k_1}, \qquad b_1 = k_1^{-1} r_0^{1+k_1}, \\ a_i &= \frac{1}{2}\Bigg[a_{i-1}\left(\frac{k_{i-1}}{k_i}\frac{E_{\theta i}}{E_{\theta i-1}} - \frac{\mu_{ri-1}}{k_i}\frac{E_{\theta i}}{E_{ri-1}} + \mu_{ri}k_i + 1\right) r_{i-1}^{k_{i-1}-k_i} \\ &\qquad + b_{i-1}\left(\frac{k_{i-1}}{k_i}\frac{E_{\theta i}}{E_{\theta i-1}} + \frac{\mu_{ri-1}}{k_i}\frac{E_{\theta i}}{E_{ri-1}} - \mu_{ri}k_i - 1\right) r_{i-1}^{-k_{i-1}-k_i}\Bigg], \\ b_i &= a_i r_{i-1}^{2k_i} - a_{i-1} r_{i-1}^{k_{i-1}+k_i} + b_{i-1} r_{i-1}^{k_i - k_{i-1}}, \qquad i = 2,3,\dots,m. \end{aligned} \tag{5}$$

where $E_{\theta i}, E_{ri}$ and μ_{ri} are the orthotropic modules of elasticity and the Poisson's ratio of the i-th layer, respectively. The degree of orthotropy of this layer is $k_i = \sqrt{E_{\theta i}/E_{ri}}$.

Additional stresses in the layer m, arising during the growth of the layer j $(j > m)$, are calculated according to equations (4):

$$\begin{aligned} \sigma^*_{rm(j)}(r) &= \frac{E_{\theta 1}}{2}\left(a_m r^{k_m - 1} - b_m r^{-k_m - 1}\right)\tilde{\varepsilon}_{\theta 1(j)}(r_0, r_{j-1}), \\ \sigma^*_{\theta m(j)}(r) &= \frac{k_m E_{\theta 1}}{2}\left(a_m r^{k_m - 1} + b_m r^{-k_m - 1}\right)\tilde{\varepsilon}_{\theta 1(j)}(r_0, r_{j-1}), \end{aligned} \tag{6}$$

where $\tilde{\varepsilon}_{\theta 1(j)}(r_0, r_{j-1}) = \varepsilon_{\theta 1(j)}(r_0, r_j) - \varepsilon_{\theta 1(j)}(r_0, r_{j-1})$ is the change of the circumferential strain measured on the free contour of the initial region $(r = r_0)$ during the growth of the layer j $(r_{j-1} \le R \le r_j)$.

By solving equation (3) with respect to the derivative of strain and by integrating in the limits $r \le R \le r_m$, we obtain a formula for calculating the change of strain from the initial stress measured on the moving surface of the growth region:

$$\tilde{\varepsilon}_{\theta 1(m)}(r_0, r) = -\frac{2}{E_{\theta 1}}\int_r^{r_m}\frac{\bar{\sigma}_{\theta m}(R)R^{k_m}}{a_m R^{2k_m} - b_m}dR. \tag{7}$$

The change of the strain $\tilde{\varepsilon}_{\theta 1(j)}(r_0, r_{j-1})$ on the free contour of the initial region, arising from the growth of the layer j $(j > m)$, can be calculated by means of equation (7) taking $r = r_{j-1}$ and $m = j$.

Equations (2)–(7) form a unique algorithm of layer growing/removing methods for orthotropic non-homogeneous discs (including tree discs) [5], allowing, in particular, calculation of growth stresses, during free growth, on the outer surface of the whole disc $(r = r_0)$ from initial (maturation) stress on the moving outer surface measured, e.g. by the stress release method [12]. Thus, it is possible to consider equations (2)–(7) as an extension of Kübler's model. Indeed, for initial data $E = const, \mu = const, \bar{\sigma}_{\theta 2} = const$ equations (1) follow from extended Kübler's model (2)–(7).

3. An illustrative computational example and discussion

Using the computer program RS-DISC+ (see [7]), an illustrative example is realized. In this example, residual growth stresses are computed for a solid disc $(r_0 = 0)$ of spruce wood, considered to be multilayered (annual rings), assuming that disc growth occurs at the constant initial stress $\bar{\sigma}_{\theta m} = 3$ MPa for early wood and at $\bar{\sigma}_{\theta m+1} = 5$ MPa for late wood. The total number of layers is $n = 31$, the core radius is $r_1 = 1.5$mm, the final radius is $r_{31} = 56$ mm. The elastic constants are [2], [4]: $E_{\theta 1} = E_{r1} = 100$ MPa, $\mu_{r1} = 0.33$ for the core and $E_{\theta m} = 300$ MPa, $E_{rm} = 500$ MPa, $\mu_{rm} = 0.33$ for early wood and $E_{\theta m+1} = 450$ MPa, $E_{rm+1} = 700$ MPa, $\mu_{rm+1} = 0.33$ for late wood.

For comparison, growth stresses are calculated from Kübler's equations (1) for the mean value of maturation stresses $\bar{\sigma}_{\theta 2} = 4$ MPa for early and late wood. The results of comparative calculations are presented in Fig. 2. It follows from Fig. 2 that growth stresses reach their absolute maximum near the pith. For the growth region $r_1 \le r \le r_2$, Kübler's homogeneous isotropic model yields results coinciding approximately with the results obtained from the extended model (2)–(7). In the pith $(r_1, r \to 0)$, according to Kübler's original model (1), stresses increase infinitely. On the other hand, according to the extended model (2)–(7), growth stresses in the pith region ($0 \le r \le r_1 = 1.5$ mm) have finite values $\sigma_{r1} = \sigma_{\theta 1} = -14.48$ MPa.

4. Conclusions

The above example of the use of extended Kübler's model shows that reasonable predictions of the growth stress distribution can be obtained by using governing equations of the layer growing method. The extended model permits to take account of the orthotropic characteristics and layered structure of the tree stem as well as to avoid the singularity of stresses in the pith.

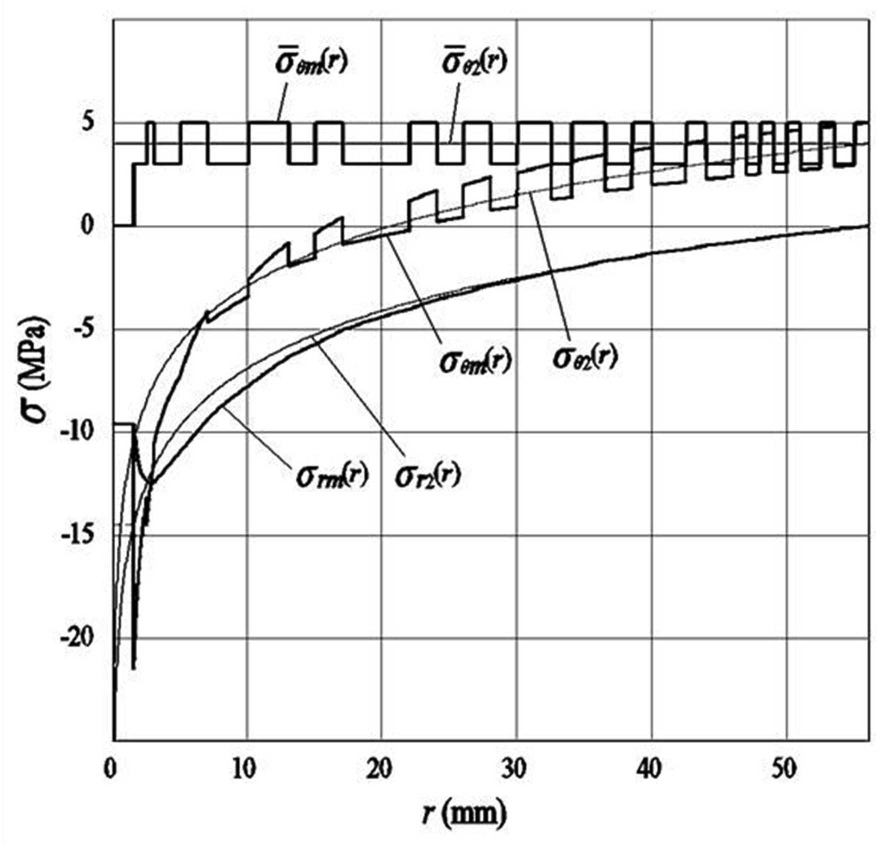

Fig. 2. Comparison of the growth stress distributions predicted by Kübler's original model (1) (thin lines) and by extended Kübler's model (2)–(7) (thick lines).

References

[1] R.R. Archer. *Growth stresses and strains in trees*. Springer-Verlag, Berlin Heidelberg, 1987, 240 p.

[2] E.K. Ashkenazi. *Anisotropy of the Wood and Wood Materials*. Lesnaya promyshlennost, Moscow, 1978, 224 p. (in Russian).

[3] R.K. Bamber. Origin of growth stresses. *Forpride Digest*, Vol. 8, No. 1, 1978, pp. 75–96.

[4] J. Bodig, B.A. Jayne. *Mechanics of Wood and Wood Composites*. Van Nostrand Reinhold, New York, 1982, 712 p.

[5] W. Kang, N.-H. Lee, S. Pang, W.Y. Chung. Free vibration of polar orthotropic circular plates with elastic growth stresses and drying stresses. *Applied Acoustics*, Vol. 69, No. 6, 2008, pp. 985–993.

[6] H. Kubler. Growth Stresses in Trees and Related Wood Properties. *Forestry Abstracts*, Vol. 48, No. 3, 1987, pp. 131–189.

[7] J., Kõo and J. Valgur. Layer growing/removing method for determination of residual stresses in thin orthotropic inhomogeneous discs. *Material Science Forum*, Vols. 524-525, 2006, pp. 659–664.

[8] H. Kübler. Studien über Wachstumsspannungen des Holzes. Erste Mitteilung: Die Ursache der Wachstumsspannungen und die Spannungen quer zur Faserrichtung. *European Journal of Wood and Wood Products*, Vol. 17, No. 1, 1959, pp. 1–9.

[9] H. Kübler. Studien über Wachstumsspannungen des Holzes. Zweite Mitteilung: Die Spannungen in Faserrichtung. *European Journal of Wood and Wood Products*, Vol. 17, No. 2, 1959, pp. 44–54.

[10] C. Mattheck, H. Kubler. *Wood – The Internal Optimization of Trees*. Springer-Verlag, Berlin, 1995, 129 p.

[11] E. Münch. Statik und Dynamik des schraubigen Baues der Zellwand besonders des Druck- und Zugholzes. *Flora*, Vol. 32, 1938, pp. 357–424.

[12] Y. Sasaki, T. Okuyama and Y. Kikata. The evolution process of the growth stress in the tree: the surface stresses on the tree. *Mokuzai Gakkaishi*, Vol. 24, No. 3, 1978, pp. 149–157.

Evaluation of plywood sandwich panels with rigid PU foam-cores and various configurations of stiffeners

Edgars Labans[1], **Gints Jekabsons, Kaspars Kalniņš**[2]
Institute of Materials and Structures, Riga Technical University,
Riga, Latvia
[1]*edgars.labans@rtu.lv,* [2]*kaspars.kalnins@sigmanet.lv*

Kaspars Zudrags, Sanita Rudzite
Forest Sector Competence Centre,
Riga, Latvia,

Mikelis Kirpluks, Ugis Cabulis
Latvian State Institute of Wood Chemistry,
Riga, Latvia

Abstract. Current paper deals with numerical analysis and optimisation of the mechanical and thermal behaviour of rib-stiffened sandwich panels with plywood and PU foam core constituents. The effect of the skin and rib thicknesses and core density on mechanical and thermal properties has been analysed. Sandwich panel stiffness and of effective thermal conductivity were acquired by means of numerical models in ANSYS software. Parametrical optimisation of the cross section dimensions and material properties was performed to found the best trade-off between stiffness, structural weight and thermal properties. Comparing optimised sandwich structures with tradition plywood boards it is possible to found equivalent stiffness sandwich panels with weight reduction up to 35% and effective thermal conductivity of $0.029\,\mathrm{W/m\cdot k}$ (reference to 0.12 for solid plywood board). In addition Pareto optimality front between structure weight and stiffness (comparing to solid plywood) and effective thermal conductivity has been constructed.

Keywords: *plywood sandwich structures, weight optimisation, stiffness, thermal conductivity.*

1. Introduction

Widely used in all fields of engineering plywood boards has good mechanical properties/weight ratio comparing with other conventional materials like steel or reinforced concrete. However for thick plywood boards there is still significantly high density and corresponding costs to other board materials. Large thickness plywood boards are especially ineffective as large span decking structures. In such case sandwich concept of replacing solid core to lightweight and cost effective stiffener/foam core could serve as useful alternative to reduce weight and cost of the inner layer material. Most extensive theoretical base on sandwich design is summarised in great detail [1, 2].

Considering that there is several design variables for sandwich panel cross-section, the optimization allows to track the most efficient combinations of these variables. Advantages of stiffness and weight optimisation for sandwich panels with weak foam cores are described in several research articles [3–5]. Optimisation of the rib-stiffened panels without any core filler is given in previous research by Labans and Kalnins [6] where clear weight saving of more than 60% comparing with reference plywood boards has been achieved. In additional optimisation results were experimentally validated by making 4-point bending tests on panel prototypes. Novel contribution to design and optimisation of plywood based sandwich panels also has been provided in several recent articles [7, 8, 9].

In current research foam core was introduced mainly to address one shot manufacturing process of the sandwich panels with rib-stiffened core. Additional benefits of the foam core filler are improved shear rigidity of the core and consistent quality of sound/vibration and thermal insulation. Therefore trade-off between mechanical and thermal properties should be found.

2. Materials and methods

2.1. Numerical modelling

Mechanical and thermal responses have been acquired by the means of numerical models based on Finite Element Method (FEM). Commercial software ANSYS [10] has been employed for this purposes. Combined shell and solid element types have been combined for stiffness calculations with 4-node SHELL181 elements and 8-node SOLID185 elements. For the purposes of further validation of the shell elements 4-point bending load appliance scheme were applied with the distance between load appliance points of 300 mm and distance between supports of 1100 mm (distances according to EN789[11]). Simply supported boundary conditions were applied at the nodes of both sandwich panel ends. Nodes with coupled vertical displacement were used for simulating of linear bending loads. Multi-layered element structure involves taking into account stiffness effect due to material orientation in the layer of every single ply in given cross-section. Approximate thickness of one layer is 1.3 mm. Mechanical properties of plywood veneer determined in previous study [12] are as follows elastic modulus in longitudinal direction $E_L = 17$ GPa; elastic modulus in radial and transversal direction $E_R = E_T = 0.5$ GPa; shear modulus $G_{RT} = 0.04$ GPa, $G_{LR} = G_{LT} = 0.7$ GPa; Poisson's ratio $v_{RT} = 0.5$ GPa, $v_{LR} = v_{LT} = 0.035$ and density of $630\ \mathrm{kg/m^3}$. Mesh density with cube size of $10\ \mathrm{mm}$ has been assigned to the structure as shown in Fig. 1.

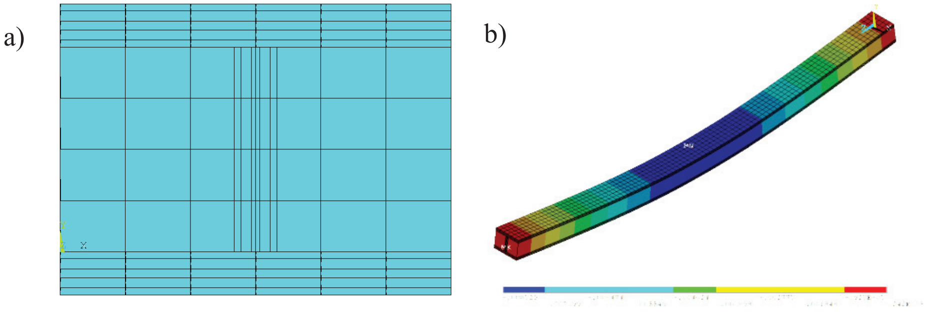

Fig.1. a) - mesh pattern and b) - deformed shape of the panel section.

As a foam filler rigid PU foam has been applied. Rigid PU foams are one of the most effective thermal insulation material available on market with thermal conductivity of $18 - 28\ \mathrm{mW/(m{\cdot}K)}$ [2, 13]. Low thermal conductivity, closed-cell structure, low water adsorption and moisture permeability, and relatively high compressive strength make this material competitive with polystyrene foams (XPS and EPS) despite higher price [10]. The linear relation between modulus of elasticity and density is given in Fig. 2c.

Thermal model of the cross-section numerically represented in 2D model with PLANE55 elements. Steady state analysis with loads applied as temperature on lower and upper nodes of the mesh. Mesh pattern and heat flow is also shown in Fig. 2.

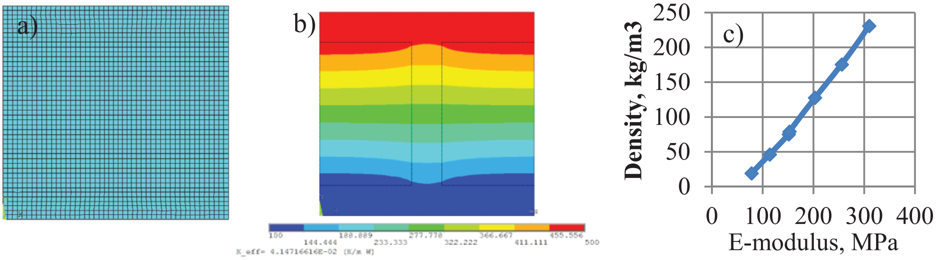

Fig.2. a) - mesh pattern; b) -nodal temperatures at thermal equilibrium; c) – density and modulus of elasticity curve.

As the result of the thermal simulation – the sum of heat flow magnitudes from base nodes are extracted and thermal conductivity k is calculated by Fourier's law (1):

$$k = \frac{d \cdot q''}{A \cdot \Delta T} \tag{1}$$

where d is thickness of the sandwich, q''- heat flux, A- sandwich base area and ΔT temperature difference between upper and lower plate.

2.2. Optimisation

The cross section of a corrugate panel has been characterised with five design variables (Table 1). Separate parameter assigned for core density P_5, which has linear relation with foam mechanical properties.

The design space and parametrical increment for the variables are given in Table 1. In the case of plywood core, core wall thickness is expressed by the number of plies. Acquired response parameters resulting from numerical calculations are maximum deflection at the middle of span and mass of the panel calculated by means of densities. Effective thermal conductivity has been extracted by running the same design of experiments exclusively for thermal 2D model.

Table 1. Design variables.

Parameter	Lower bound	Upper bound	Step	Units
Number of surface plies - P_1	3	7	2	-
Number of stiffener plies –P_2	3	7	2	-
Stiffeners distance– P_3	10	80	10	mm
Total section height – P_4	30	70	-	mm
Foam E-modulus – P_5	75	300	-	MPa

In the present research a sequential space filling design based on Latin Hypercube with Means Square error criterion has been evaluated by the in house EdaOpt software [14]. All responses have been approximated employing Adaptive Basis Function Construction (ABFC) approach proposed by [15].

3. Results and discussion

3.1. Equivalent stiffness sandwich panel design

For efficient evaluation mechanical and thermal properties of sandwich panels were compared with conventional plywood boards. It is commonly known that sandwich panel thickness could be raised to increase bending stiffness without any significant weight penalty. Therefore in the first optimisation step combinations of variables have been selected. This guarantee deflection restrain not to over exceed values obtained from numerical analysis of conventional plywood board. Relative mass indicator is obtained dividing sandwich panel mass by mass of plywood board of the same stiffness.

Table 2. Optimised sandwich panels in comparison with conventional plywood.

	Equivalent of 30 mm plywood	**Equivalent of 40 mm plywood**	**Equivalent of 50 mm plywood**
Cross-section parameter values	$P_1 = 5; P_2 = 3; P_3 = 56;$ $P_4 = 33; P_5 = 75$	$P_1 = 5; P_2 = 5; P_3 = 74;$ $P_4 = 48; P_5 = 75$	$P_1 = 5; P_2 = 3; P_3 = 68; P_4 = 63; P_5 = 75$
Relative mass, %	47.8	40.9	32.3
Relative thermal conductivity, %	28.3	25.1	21.4

Analysing results summarised in Table 2 it could be stated that advantage of sandwich panels increases gradually by increasing thickness. Due to exploitation considerations surface thickness of the sandwich panel with 33 mm section height has been raised to 5 layer. For all sandwich panels types the most efficient strategy to increase stiffness is by increasing the section height using 3-layer stiffeners and foam filler with low density. In case of the sandwich panel with the largest section height, variables P_3 and P_4 reached the boundaries of design space. Therefore it has been considered useful to run the same optimisation task for sandwich panels with foam core only (without stiffeners). Results of this optimisation are shown in Table 3.

Table 3. Optimised sandwich panels (without stiffeners) in comparison with solid plywood.

	Equivalent to 30 mm plywood	**Equivalent to 40 mm plywood**	**Equivalent to 50 mm plywood**
Cross-section parameter values	$P_1 = 5; P_4 = 34; P_5 = 75$	$P_1 = 5; P_4 = 53; P_5 = 75$	$P_1 = 5;\ P_4 = 70;\ P_5 = 121$
Relative mass, %	47.1	34.1	35.5
Relative thermal conductivity, %	25.3	21.7	24.7

From both types of sandwich structures it is clearly seen that increasing section thickness is more efficient than raising density and thus mechanical properties of the foam. In the last column of Table 3 foam properties were increased due to the reason that section height variable reached upper boundary.

3.2. Pareto optimality front

Overall efficiency of plywood sandwich panels has been demonstrated by formulating 3D Pareto optimization problem where maximization of relative stiffness ΔS is done simultaneously by minimizing the relative mass ΔM and relative thermal conductivity ΔK of the panel (Fig. 3 and 4). Relative values is acquired dividing numerically calculated conventional plywood board deflection and thermal conductivity with corresponding values of sandwich panel with the same length and thickness, under the same loading conditions. Relative mass is acquired by dividing sandwich panel mass with solid plywood panel mass.

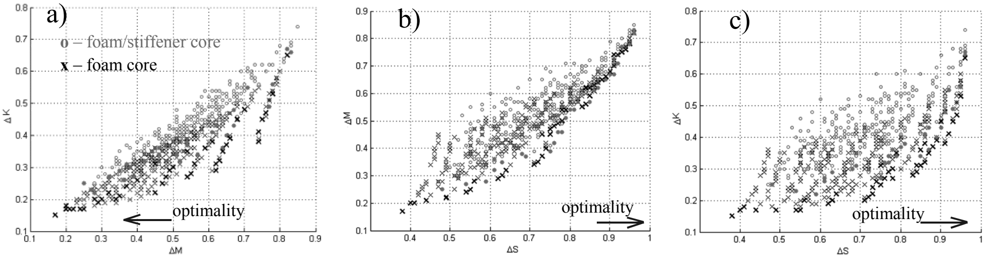

Fig. 3. Graphic representation of Pareto optimality between each of two responses.

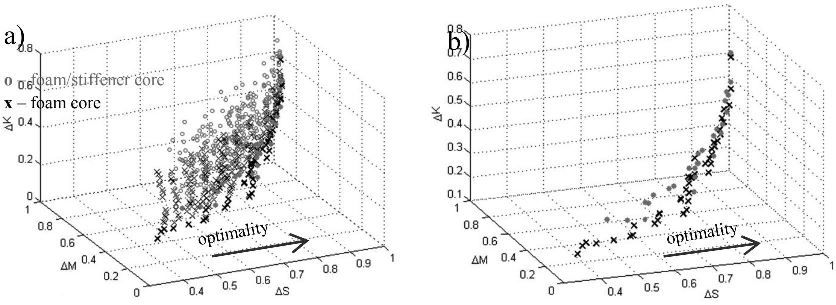

Fig. 4. Graphic representation of Pareto optimality between three responses a) – all data points; b) –only points on Pareto front.

From Fig. 3 and 4 it is seen that both core types has similar stiffness/mass ratio. Most of the marked points (pints on the Pareto front) in Fig. 3b have matching positions. However sandwich panels with foam core has better relative thermal conductivity and stiffness and mass ratio (Fig. 3b, Fig. 3c). Pareto front of sandwich panels with without stiffeners is significantly closer to optimality point.

4. Conclusions

Performing parametrical optimisation on sandwich panels with plywood surfaces and PU foam core the optimal combinations of the variables granting the same stiffness as for plywood reference panel have been found. The largest mass and thermal conductivity benefits has sandwich structures with highest cross-section thickness. Solid plywood board with thickness of 50 mm could be successfully replaced by the same stiffness sandwich panel with 63 mm thickness, but possessing only 32.3% of the reference panel`s mass and approximately 5-fold decreased effective thermal conductivity. Due to the fact that PU foam, made of renewable components, has linear modulus/density ratio increment of sandwich thickness is more efficient than use of higher density foam core.

Pareto optimality front for all three numerical responses has been constructed to assess field of possible optimisation outputs. General trend observed in Pareto front shows that sandwich panels with foam core filler outperform panels with additional stiffeners especially comparing effective thermal conductivity.

Acknowledgements

The research has received funding from Latvia state research program under grant agreement "Innovative and multifunctional composite materials for sustainable buildings (IMATEH)". Research was also partially supported by Forest Sector Competence Centre and Investment and Development Agency of Latvia according agreement No. L-KC-11-004.

References

[1] H.G. Allen. *Analysis and Design of Structural Sandwich Panels*. Pergamon Press, Oxford, 1969.
[2] D. Zenkert. *An Introduction to Sandwich Construction*. EMAS, London, 1995.
[3] J.M. Whitney. A local model for bending of weak core sandwich plates. *Journal of Sandwich Structures and Materials,* Vol. 3, 2001, pp. 269–288.
[4] T. Kawasaki, M. Zhang, Q. Wang, K. Komatsu and S. Kawai. Elastic moduli and stiffness optimization in four-point bending of wood-based sandwich panel for use as structural insulated walls and floors. *Journal of Wood Science,* Vol. 52, No. 4, 2006, pp. 302–310.
[5] S.R. Swanson and J. Kim. Optimization of sandwich beams for concentrated loads. *Journal of Sandwich Structures and Materials,* Vol. 4, 2002, pp. 273–293.
[6] E. Labans and K. Kalniņš. Experimental Validation of the Stiffness Optimisation for Plywood Sandwich Panels with Rib-Stiffened Core. *Wood Research*, 2014, Vol. 59, No. 4, pp. 793–802.
[7] J. Sliseris, G. Frolovs, K. Rocens and V. Goremikins. Optimal design of GFRP-plywood variable stiffness plate. *Procedia Engineering*, 2013, 1060 p.
[8] S. Banerjee and D. Bhattacharyya. Optimal design of sandwich panels made of wood veneer hollow cores. *Composites Science and Technology,* Vol. 71, No. 4, 2011, pp. 425–432.
[9] F. Negro, C. Cremonini, R. Zanuttini, M. Properzi and F. Pichelin. A new wood-based lightweight composite for boatbuilding. *Wood Research,* Vol. 56, No. 2, 2011, pp. 257–266.
[10] ANSYS Help Manual of the ANSYS *Version 13.0 2013.*
[11] EN 789:2004. Timber structures. Test methods. Determination of mechanical properties .of wood based panels. European Committee for Standardization (CEN), Brussels.
[12] E. Labans, K. Kalnins and O. Ozolins. Experimental and Numerical Identification of Veneers Mechanical Properties. *RTU Construction science* –11.V. Riga, 2010, pp. 38–43.

[13] M. Kirpluks, U. Cabulis, V. Zeltins, L. Stiebra and A.A. Avots. Rigid Polyurethane Foam Thermal Insulation Protected with Mineral Intumescent Mat, *AUTEX Research Journal*, Vol. 14, No. 4, December 2014.

[14] J. Auziņš and A. Januševskis. *Eksperimentu plānošana un analīze*. Riga, RTU publishing. 2007, 208 p. (in Latvian).

[15] G. Jekabsons. Adaptive Basis Function Construction: an approach for adaptive building of sparse polynomial regression models. *Machine Learning,* Yagang Zhang (Ed.), In-Tech, 2010, pp. 127–156.

Free vibrations of elastic laminated arches

Jaan Lellep[1], **Alexander Liyvapuu**[2]

Institute of Mathematics, University of Tartu
Tartu, Estonia
[1]*jaan.lellep@ut.ee*, [2]*liyvapuu@ut.ee*

Abstract. Vibrations of elastic arches made of inhomogeneous materials are studied. The case of laminated formed by laminae made from different materials are investigated in the greater detail. The laminates may have internal defects. The influence of geometrical and physical parameters on the eigenfrequencies of arches simply supported at the both ends is assessed numerically.

Keywords*:* *elasticity, laminate, composite material, natural vibrations, arch.*

1. Introduction

Due to their high stiffness and strength and other mechanical properties compared to the weight the composite and laminate structures have gained popularity during last decades. This involves the need for investigation of the behaviour of structures made of composites and laminates. The foundation of the mechanics of composite materials are presented in the books by Herakovich [10], Jones [11], Daniel [8].

Thin-walled plate and shell structures are treated by Collar and Springer [12], Reddy [14], Vinson and Sierakowski [16], Qatu [13].

The vibrations and stability of structural elements containing cracks and other defects have deserved the attention of many researchers. However, the most of attention is paid to the vibrations of beams (see Dimarogonas [1], Nandwana and Maiti [6], Nahvi and Jabbari [5], Kisa and Brandon [2], Zheng and Kessissoglou [7]).

Lellep and Kägo [3] investigated the influence of defects on the eigenfrequencies of elastic stretched strips. In the previous paper by the authors free vibrations of elastic arches, made of homogeneous materials, are studied.

In the present paper the results of the previous study [4] are extended to the case of arches made of composite and laminate materials.

2. Problem formulation and basic assumptions

Vibrations of an elastic arch will be considered. The arch is simply supported at the edges $\varphi = 0$ and $\beta = 0$ (Fig. 1).

Here and henceforth φ stands for the current angle defining the position of a cross section of the arch. It is assumed that the arch has a constant radius R and that the cross section of the arch is rectangular with the width b and total height (thickness) $H = const.$

The cross section of the arch consists of layers with thickness h_j $(j = 0, 1, \dots, n)$. Each layer is assumed to be an elastic layer with material parameters ϱ_j (density), E_j (Young modulus), ν_j (Poisson's ratio). The layers are treated as orthotropic laminae consisting of a matrix material and of uniformly embedded fibers. However, in the case an orthotropic lamina these engineering constants are not independent.

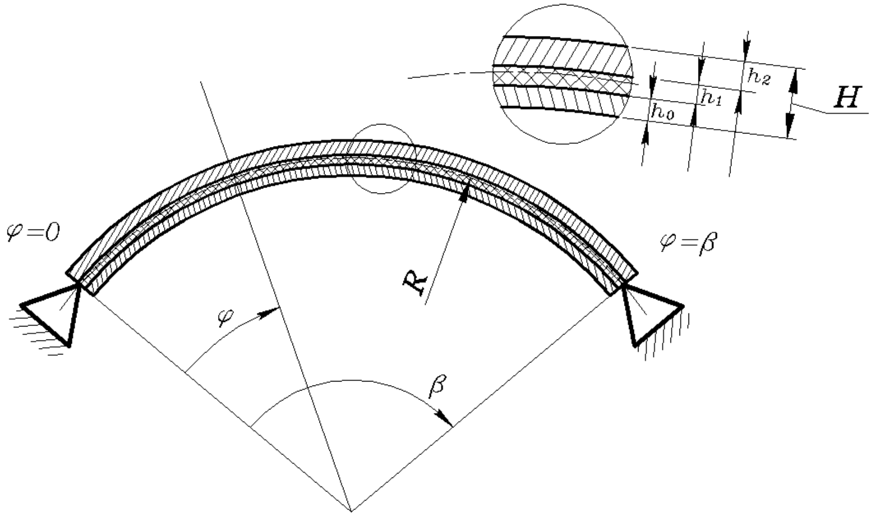

Fig. 1. Geometry of a laminated arch.

For a plane stress situation one has (see Gürdal, Haftka, Hajela [9])

$$\frac{\nu_{12}}{E_1}=\frac{\nu_{21}}{E_2}. \tag{1}$$

3. Governing equations

In the theory of laminated elastic plates the physical relations can be presented as see Kollar and Springer [12], Reddy [14], Vinson and Sierakowski [16])

$$N = A\varepsilon + B\varkappa \tag{2}$$

and

$$M = B\varepsilon + D\varkappa \tag{3}$$

Here N and M stand for vectors of membrane forces and principal moments, respectively, whereas ε and $\varkappa$ are corresponding vectors of strain components and curvatures.
The elements of matrices A, B and D can be calculated as (Vinson and Sierakowski [16])

$$\begin{aligned} A_{ij} &= \sum_{k=1}^{n} Q_{ij}^{(k)}\left(z_k - z_{k-1}\right), \\ B_{ij} &= \frac{1}{2}\sum_{k=1}^{n} Q_{ij}^{(k)}\left(z_k^2 - z_{k-1}^2\right), \\ D_{ij} &= \frac{1}{3}\sum_{k=1}^{n} Q_{ij}^{(k)}\left(z_k^3 - z_{k-1}^3\right), \end{aligned} \tag{4}$$

where $|z_k - z_{k-1}| = h_k$.

In the case of laminate for which each lamina is reinforced with a unidirectional array of fibers one has

$$Q_{11}^{(k)} = \frac{E_1^{(k)}}{1-\nu_{12}^{(k)}\nu_{21}^{(k)}}, \quad Q_{12}^{(k)} = \frac{\nu_{12}^{(k)}E_2^{(k)}}{1-\nu_{12}^{(k)}\nu_{21}^{(k)}}, \quad Q_{22}^{(k)} = \frac{E_2^{(k)}}{1-\nu_{12}^{(k)}\nu_{21}^{(k)}}, \tag{5}$$

where the superscript (k) indicates the number of lamina.

In the case of beams and arches the quantities Also the vectors ε and $\varkappa$ are one-dimensional strain components.

These can be expressed as

$$\varepsilon = \frac{1}{R}(U' + W), \qquad \varkappa = -\frac{1}{R^2}(-U' + W''), \tag{6}$$

where prims denote the differentiation with respect to the angle φ. Here U and W stand for the displacements of the middle surface in the circumferential and transverse directions, respectively.

The Hooke's law furnishes with (2), (3) and (6) the relations

$$N = \frac{A}{R}(U' + W) + \frac{B}{R^2}(U' - W'') \tag{7}$$

and

$$M = \frac{B}{R}(U' + W) + \frac{D}{R^2}(U' - W''). \tag{8}$$

In the present paper is it assumed that there is no extension of the middle surface of the arch. Therefore, one can take $\varepsilon = 0$ and $U' = -W$.

Thus

$$\varkappa = -\frac{1}{R^2}(W + W''). \tag{9}$$

and

$$M = -\frac{D}{R^2}(W + W''). \tag{10}$$

The equilibrium conditions of an element of the arch can be put into the form (see Soedel [15], Lellep and Liyvapuu [4])

$$M'' + M + R^2\left(p - \mu\ddot{W}\right) = 0, \tag{11}$$

where μ stands for the mass per unit length of the arch and dots denote the differentiation with respect to time t.

4. Eigenfrequencies of the arch without defects

For determination of eigenfrequencies of free vibrations of the arch one has to solve the governing equations (10), (11) and satisfy corresponding boundary conditions.

In the case of an arch simply supported at both edges the boundary requirements are at $\varphi = 0$

$$W(0;t) = 0, \quad M(0,t) = 0 \tag{12}$$

and at $\varphi = \beta$

$$W(\beta;t) = 0, \quad M(\beta,t) = 0. \tag{13}$$

Substituting (10) in (11) and taking into account that in the case of free vibrations $p = 0$ one has

$$\frac{D}{R^2}(W^{IV} + 2W'' + W) + \bar{\varrho}R^2\ddot{W} = 0, \tag{14}$$

where $\bar{\varrho}$ is the mass per unit area of the middle surface of the arch.

Looking for solution (14) it is reasonable to assume that (see Lellep and Liyvapuu [4], Soedel [15])

$$W(\varphi, t) = w(\varphi)\sin\omega t \tag{15}$$

Where the first term in the product is a function of the coordinate φ only and the second term depends on time t.

$$W'(\varphi, t) = w'(\varphi)\sin\omega t,$$

$$W''(\varphi, t) = w''(\varphi)\sin\omega t, \tag{16}$$

$$W'''(\varphi, t) = w'''(\varphi)\sin\omega t,$$

$$\ddot{W} = -w(\varphi)\sin\omega t \cdot \omega^2.$$

Substituting (15), (16) in (14) one obtains an ordinary differential equation of the fourth order. The general solution on this equation is

$$w = C_1\cosh\mu\varphi + C_2\sinh\mu\varphi + C_3\cos\nu\varphi + C_4\sin\nu\varphi, \tag{17}$$

where C_1, C_2, C_3 and C_4 are arbitrary constants and

$$\mu = \sqrt{1 - \omega R^2\sqrt{\frac{\bar{\varrho}}{D}}}, \quad \nu = \sqrt{1 + \omega R^2\sqrt{\frac{\bar{\varrho}}{D}}}. \tag{18}$$

The boundary conditions for the deflection and bending moment (12), (13) infer the requirements

$$w(0) = 0, \qquad w''(0) = 0 \tag{19}$$

and

$$w(\beta) = 0, \qquad w''(\beta) = 0. \tag{20}$$

Conditions (19), (20) with (17) lead to the linear algebraic system with determinant

$$\begin{vmatrix} \sinh\mu\beta & \sin\nu\beta \\ \mu^2\sinh\mu\beta & -\nu^2\sin\nu\beta \end{vmatrix} = 0. \tag{21}$$

It follows from (18) and (21) that

$$\omega = \pm\sqrt{\frac{D}{\bar{\varrho}}} \cdot \frac{\pi^2k^2 - \beta^2}{\beta^2R^2}, \tag{22}$$

where $k = 1, 2, \dots$.

5. Numerical results and discussion

The results of calculations are presented in Fig. 2–Fig. 5 and Table 1.

The obtained results correspond to the three-layers arch with thicknesses h_0, h_1, h_2. Materials of layers are shown in Table 1.

Table1. Materials of different layers.

	E, Pa	ϱ, kg/m^3	ν
Steel	$2.1\cdot10^{11}$	7865	0.3
Aluminium	$7\cdot10^{9}$	2700	0.35
Polystirol	$1.5\cdot10^{9}$	30	0.1

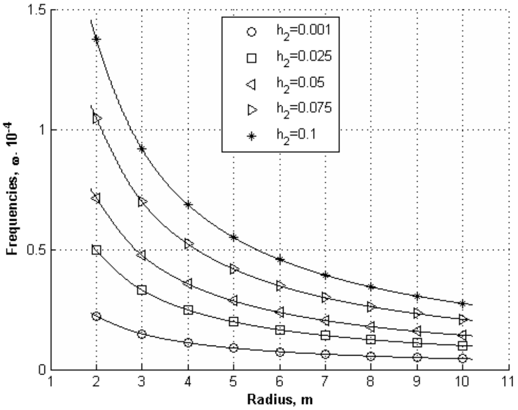

Fig. 2. Dependence on thickness of steel layer.

In Fig.2 – Fig.4 the succession of materials is: aluminium, polystirol, steel. The values of natural frequencies versus the radius of the arch are depicted in Fig. 2. The thicknesses of layers $h_0 = h_1 = 0.01 = const$.

It can be seen from Fig. 2 that the natural frequency decreases with increasing the radius.

The natural frequencies versus the angle β are presented in Fig. 3.

Here $h_0 = h_1 = h_2 = 0.01$.

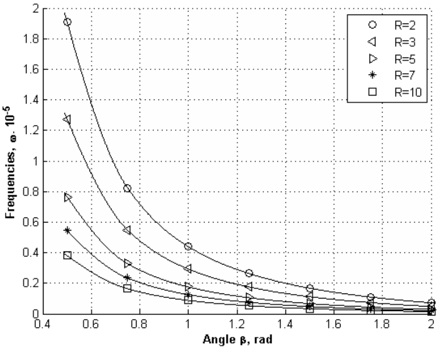

Fig. 3. Natural frequency versus the angle β.

The influence of the natural frequency on the ratio of thicknesses is presented in Fig.4 (here $h_0 + h_2 = 0.01$; $h_1 = 0.01$).

In Fig. 5 the natural frequencies of the arch are presented in the cases of different order of stacking the layers with steel (S), polystirol (P) and aluminium (A).

Here $h_0 = h_1 = h_2 = 0.01$. Three curves presented in Fig. 5 correspond to the combination of layers P-A-S, S-P-A and A-S-P, respectively. It can bee seen from Fig. 5 that the lowest values of the natural frequency correspond to the succession S-P-A.

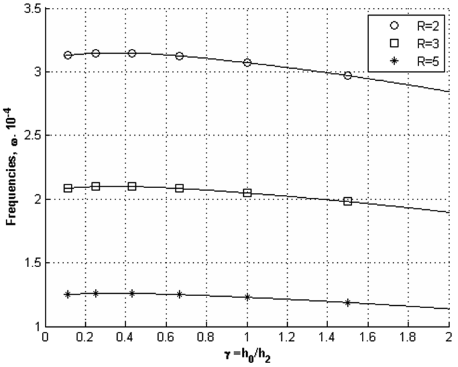

Fig. 4. Natural frequency versus the ratio of thicknesses of layers.

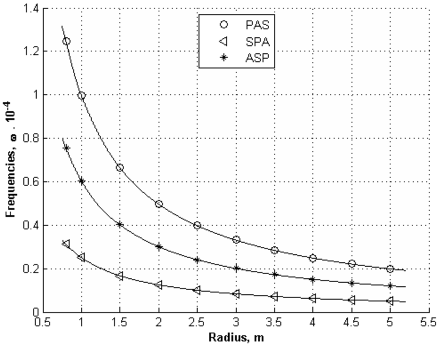

Fig. 5. The natural frequency versus the order of stacking of materials.

6. Concluding remarks

A method for determination of frequencies of natural vibrations of laminated arches was developed. The arches under consideration are made of multi-layered composite materials and may have internal defects. The case where the both edges of the arch are simply supported is studied in a greater detail. The sensitivity of the natural frequency on the thicknesses and physical parameters of different layers was established. The method developed above can be extended for the case of an arch with stepped thickness.

Acknowledgements

The partial support from the Estonian Science Foundation Grant ETF 9110 “Optimization of structural elements” and from Institutional research funding IUT20-57 of the Estonian Ministry of Education and Research is gratefully acknowledged.

References

[1] A.D. Dimaragonas. Vibration of ckracked structures: a state of the art review. *Engineering Fracture Mechanics*, Vol. 3, No. 12, 2009, pp. 831–857.

[2] M. Kisa and J. Brandon. The effects of closure cracks on the dynamics of a cracked cantilever beam. *Journal of Sound and Vibration*, Vol. 1, No. 238, 2000, pp. 1–18.

[3] J. Lellep and E. Kägo. Vibrations of elastic stretched strips with cracks. *International Journal of Mechanics*, Vol. 1, No. 5, 2011, pp. 27–34.

[4] J. Lellep and A. Liyvapuu. Natural vibrations of elastic arches with cracks. *In: J. Lellep, E. Puman (Eds), Optimization and Analysis of Structures*, Tartu, 2013, pp. 64–69.

[5] H. Nahvi and M. Jabbari. Crack detection in beams using experimental modal data and finite element model, *Journal of Sound and Vibration*, Vol. 3, No. 203, 1997, pp. 435–446.

[6] B.P. Nandwana and S.K. Maiti. Detection of location and size of a crack in stepped cantilever beams. *Journal of Sound and Vibration*, Vol. 3, No. 203, 1997, pp. 435–446.

[7] D.Y. Zheng and N.J. Kessissoglou. Free vibration analysis of a cracked beam by finite element method. *Journal of Sound and Vibration,* Vol. 3, No. 273, 2004, pp. 457–475.

[8] I.M. Daniel and O. Ishai. *Engineering Mechanics of Composite Materials*. Oxford University Press, 2006, 363 p.

[9] Z. Gürdal, R.T. Haftka and P. Hajela. *Design and Optimization of Laminated Composite Materials*. Wiley, New York, 1999, 337 p.

[10] C.T. Herakovich. *Mechanics of Fibrous Composites*. Wiley, New York, 1998, 140 p.

[11] R.M. Jones. *Mechanics of Composite Materials*. Taylor and Francis, Philadelphia, 1999, 519 p.

[12] L. Kollar and G.S. Springer. *Mechanics of Composite Structures*. Cambridge University Press, Cambridge, 2003, 481 p.

[13] M.S. Qatu. *Vibrations of Laminated Shells and Plates*. Elsevier, New-York, 2004, 409 p.

[14] J.N. Reddy. *Mechanics of Laminated Composite Plates and Shells. Theory and Analysis*. CRC Press, 2004, 782 p.

[15] W. Soedel. *Vibration of Shells and Plates*. Marcel Dekker, New-York, 2004, 553 p.

[16] J. Vinson and R.L. Sierakowski. *The Behavior of Structures Composed of Composite Materials*. Kluwer, 2002, 435 p.

Asymmetric blast loading of inelastic circular plates

Jaan Lellep[1], **Annely Mürk**[2]

Institute of Mathematics, University of Tartu
Tartu, Estonia
[1]jaan.lellep@ut.ee, [2]annely.murk@ut.ee

Abstract. Dynamic plastic response of a circular plate to a local blast loading is studied. The plate made of a perfect plastic material is subjected to a concentrated loading with blast-type load intensity. An approximate theoretical procedure is developed for evaluation of residual deflections. The method is used in the case of a plate loaded by an asymmetrical single load.

Keywords: *circular plate, plasticity, blast loading.*

1. Introduction

In the theory of inelastic structures approximate methods of solution are of great importance (see Gupta [1], Jones [2]). In the previous papers by the authors ([4], [5]) a method of determination of residual deflections of circular plates subjected to the asymmetric imulsive loading was developed. The method was accommodated to the case of a rectangular impulse and a concentrated loading in [5]. This approach is based on the method of mode form motions (see Martin [6], Nurick, Martin [7], Jones [2]). In the present paper the case of a blast loaded circular plate is studied in a great detail under the assumtpion that the load is applied asymmetrically.

2. Basic assumptions

Inelastic deformations of a circular plate subjected to impact and blast loadings will be considered. It is assumed that the plate is made of an ideal plastic material obeying the square yield condition ABCD (Fig. 1).

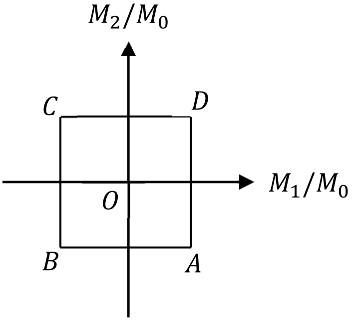

Fig. 1. The yield condition.

Let the yield moment of the plate with thickness h be $M_0 = \sigma_0 h^2/4$ where σ_0 is the yield stress of the material. Although the stress state of an element of the plate is defined by the moments M_1, M_2, M_{12} and shear forces Q_1, Q_2 it is assumed that the shear forces can be treated as reactions and the plasticity of the plate is controlled by the principlal moments M_1, M_2 only.

Let the plate be loaded by a concentrated force P applied at the point O_1 of the plate. The magnitude of the concentrated loading

$$P = \begin{cases} pe^{-\beta t}, & t \in [0, t_1] \\ 0, & t > t_1 \end{cases}, \tag{1}$$

where p and β are given constants and t stands for current time instant. According to (1) the loading is applied abruptly at the initial moment and it is removed at $t = t_1$. The subsequent motion of the plate for $t > t_1$ is due to the inertia. Note that in the case of small values of p and relatively great values of t_1 the plate can reach its permanent position at $t = T < t_1$. However, in the following the attention is paid to the loadings where $T > t_1$.

An approximate method for determination of residual deflections will be developed. Tis method is based on the extension of the principle of virtual velocities. Folloving Jones [2] it is assumed that at each time instant

$$\dot{D}_i = \dot{A}_e \tag{2}$$

where $\dot{D}_i$ stands for the dissipation rate of the internal energy and $\dot{A}_e$ is the power of external loads.

Evidently, in the case of moderate loadings the displacement rate can be presented as

$$\dot{W} = \dot{W}_0(t)\left(1 - \frac{r}{r_*(\theta)}\right). \tag{3}$$

Here r and θ denote polar radius and polar angle, respectively, provided the origin of polar coordinates is located at the point of O_1 where the point load is applied. The deflection rate at this point is denoted by $\dot{W}_0(t)$ whereas the dots denote the differention with respect to time t.

Let the distance between O_1 and the center of the circle of radius R be a. In (3) the curve $r = r_*(\theta)$ denotes the boundary of the plate. Making use of the cartesian coordinates one can write

$$\begin{aligned} x &= r_* \cos\theta, \\ y &= r_* \sin\theta. \end{aligned} \tag{4}$$

Thus the function $r_*(\theta)$ can be determined as

$$r_* = a\cos\theta + \sqrt{R^2 - a^2\sin^2\theta}, \tag{5}$$

3. Internal dissipation and external power

The velocity field (3) with (5) indicates that a yield line fan with its apex at O_1 is formed during the deformation process. It is assuming that the plate is of piece wise constant thickness

$$h = \begin{cases} h_0, & r \in [0, r_1] \\ h_1, & r \in [r_1, r_*] \end{cases} \tag{6}$$

One has to take into account that the yield moment

$$M_0 = \begin{cases} M_{00}, & r \in (0, r_1) \\ M_{01}, & r \in (r_1, r_*) \end{cases} \tag{7}$$

It can be shown that (see Kaliszky [3], Skrzypek and Hetnarski [8], Lellep and Mürk [4]) the internal energy dissipation by forming a continuous yield line fan can be calculated as

$$\dot{D}_i = \dot{W}_0 \sum_{j=0}^{1} M_{0j} \int_{r_j}^{r_{j+1}} \int_{0}^{2\pi} \frac{1}{r_*}\left(1 + \frac{r_*'^2}{r_*^2}\right) d\theta dr \tag{8}$$

Here the following notation is introduced

$$r_*' = -a\sin\theta \mp \frac{2a^2 \sin\theta \cos\theta}{\sqrt{R^2 - a^2 \sin^2\theta}}. \tag{9}$$

Evidently, the initial forces caused by the acceleration $\ddot{W}$ can be considered as external forces. Thus the power of external forces is

$$\dot{A}_e = P\dot{W}_0 - \mu\dot{W}_0\ddot{W}_0 \sum_{j=0}^{1} \int_{0}^{2\pi} \int_{r_j}^{r_{j+1}} h_j \left(1 - \frac{r}{r_*}\right)^2 r\, dr d\theta, \tag{10}$$

where μ stands for the material density and $\ddot{W}_0 = (d\dot{W}_0)/dt$.

4. Determination of deflections

Making use of the equality (2) with (8)-(10) leads to the equation

$$\begin{aligned} pe^{-\beta t} - \mu\dot{W}_0\ddot{W}_0 \sum_{j=0}^{1} \int_{0}^{2\pi} \int_{r_j}^{r_{j+1}} h_j \left(1 - \frac{r}{r_*}\right)^2 r\, dr d\theta = \\ = \dot{W}_0 \sum_{j=0}^{1} M_{0j} \int_{r_j}^{r_{j+1}} \int_{0}^{2\pi} \frac{1}{r_*}\left(1 + \frac{r_*'^2}{r_*^2}\right) d\theta dr. \end{aligned} \tag{11}$$

Calculating the integrals in (11) one obtains

$$\ddot{W}_0 = \frac{pe^{-\beta t} - \sum_{j=0}^{1} \int_0^{2\pi} M_{0j}\left(r_{j+1} - r_j\right)\frac{1}{r_*}\left(1 + \frac{r_*'^2}{r_*^2}\right) d\theta}{\mu \sum_{j=0}^{1} \int_0^{2\pi} h_j \left[\frac{1}{2}\left(r_{j+1}^2 - r_j^2\right) - \frac{2}{3r_*}\left(r_{j+1}^3 - r_j^3\right) + \frac{1}{4r_*^2}\left(r_{j+1}^4 - r_j^4\right)\right] d\theta}. \tag{12}$$

It can be seen from (12) that $\ddot{W}_0 \neq const$, as might be expected. For the second stage of motion after removing the loading the acceleration can be obtained by taking $P = 0$ in (12). Now $\ddot{W}_0 = const$. It is reasonable to present (12) in the form

$$\mu\ddot{W}_0 = \frac{pe^{-\beta t} - B}{A}, \tag{13}$$

where A, B are constants defined by (12). Integrating (13) with respect to time gives

$$\mu A\dot{W}_0 = -\frac{p}{\beta}e^{-\beta t} + \frac{p}{\beta} - Bt \tag{14}$$

for the first stage of deformation and

$$\mu A\dot{W}_0 = -\frac{p}{\beta}e^{-\beta t_1} + \frac{p}{\beta} - Bt \tag{15}$$

for the final stage of deformation for $t \in [\, t_1, t_2]$.

Integrating (14) and (15) once again and satisfying the initial condition $W_0(0) = 0$ and the continuity of W_0 at $t = t_1$ yields

$$\mu A W_0 = \frac{p}{\beta^2}e^{-\beta t} - \frac{p}{\beta^2} + \frac{p}{\beta}t - B\frac{t^2}{2} \tag{16}$$

for $t \in [\, 0, t_1]$ and

$$\mu A W_0 = \frac{p}{\beta}(1 - e^{-\beta t_1})(t - t_1) + \frac{p}{\beta^2}e^{-\beta t_1} - \frac{p}{\beta^2} + \frac{p}{\beta}t_1 - B\frac{t^2}{2} \tag{17}$$

for $t \in [\, t_1, t_2]$. The motion of the plate ceases at the time instant $t = t_2$ when $\dot{W}_0(t_2) = 0$. It follows from (15) that

$$t_2 = \frac{p}{B\beta}(1 - e^{-\beta t_1}). \tag{18}$$

The maximal residual deflections can be defined according to (17), (18) as

$$W_1 = \frac{1}{\mu A}\left\{\frac{p}{\beta}(1 - e^{-\beta t_1})(t_2 - t_1) - \frac{p}{2B\beta^2}\left(1 - e^{-\beta t_1}\right)^2 + \frac{p}{\beta^2}\left(e^{-\beta t_1} - 1\right) - \frac{p}{\beta}t_1,\right. \tag{19}$$

where $W_1 = W_0(t_2)$.

5. Numerical results and discussion

The quantities A, B, also t_1 and the maximal residual deflection W_1 are calculated numerically. The results of calculations are presented in Fig. 2 and Fig. 3. Here the notation

$$n = \frac{P(0)}{2\pi M_0 R}\sqrt{R^2 - a^2} \tag{20}$$

is used. In Fig. 2 maximal permanent deflections of a circular plate of constant thickness are presented for $\beta = 0.1$. Different curves in Fig. 2 correspond to different values of the parameter $\alpha = a/R$. Here $t_1 = 1.93$ and $n = 1.1$. The influence of maximal residual deflections on the duration of the loading phase is depicted in Fig. 3. Different curves in Fig. 3 correspond to different values of loading. Here $\beta = 0.4$ and $a = 0.7R$. Calculations carried out showed that in the case of relatively low loadings the motion of the plate can cease together with the onset of unloading. This means that the inertial motion does not take place and the relationship between W_1 and t_1 is interrupted at the point where $t_2 = t_1$ in Fig. 3.

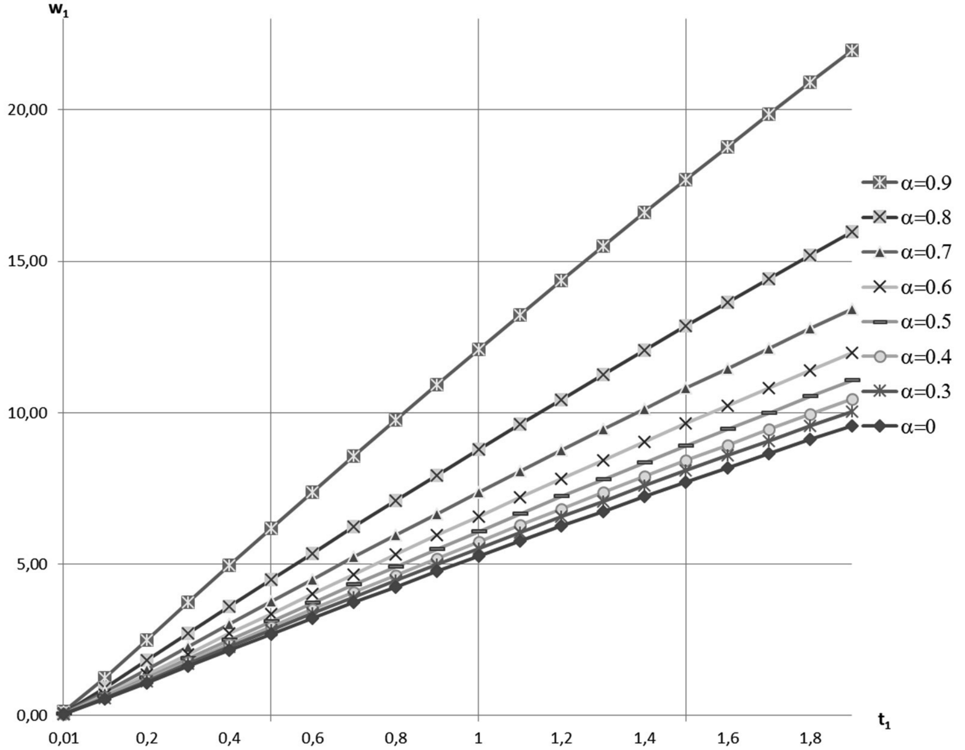

Fig. 2. Maximal permanent deflection versus the t_1.

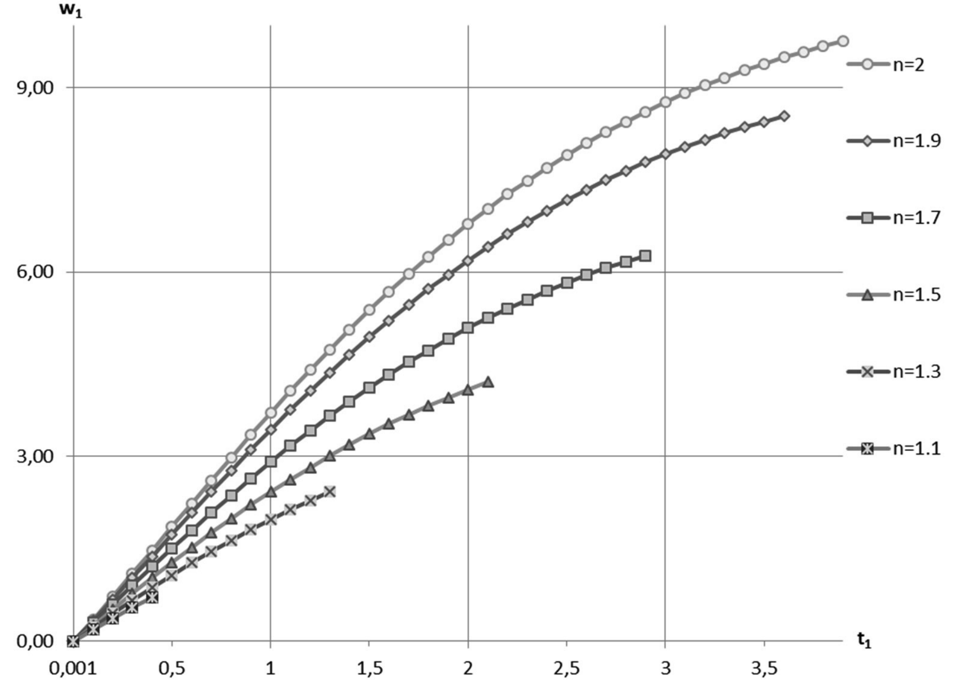

Fig. 3. Maximal permanent deflection depending on the load intensity.

6. Conclusions

An approximate theoretical procedure is developed for determination of residual deflections of circular plates loaded by concentrated forces. Calculations carried out showed that the lower is the load level during the loading stage the shorter is the total response time. Although the plate of piece wise constant thickness is treated in a detail the method can be easily extended for plates with variable thickness and for functionally graded materials. The approach prescribed above can be accommodated for the case of distributed loading.

Acknowledgements

The supports from the Estonian Science Foundation through the Grant ETF9110 and from the Institutional research funding IUT20-57 of the Estonian Ministry of Education and Research are acknowledged.

References

[1] N.K. Gupta. *Plasticity and Impact Mechanics*. Wiley, New York, 1993, 522 p.
[2] N. Jones. *Structural Impact*. CUP, Cambridge, 2011, 604 p.
[3] S. Kaliszky. *Plasticity. Theory and Engineering Applications.* Elsevier, Amsterdam, 1989, 505 p.
[4] J. Lellep and A. Mürk. Asymmetric dynamic plastic behaviour of circular plates. *In: J. Lellep, E. Puman (Eds), Optimization and Analysis of Structures*, Tartu, 2013, pp. 70–75.
[5] J. Lellep and A. Mürk. Impact loading of stepped circular plates. *Structures under Shock and Impact*, WIT Press, Vol. 13, 2014, pp. 3–11.
[6] J.B. Martin. *Plasticity*. MIT Press, 1975, 931 p.
[7] G.N. Nurick and J.B. Martin. Deformation of thin plates subjected to impulsive loading – a review. Part I. Theoretical considerations. *International Journal of Impact Engineering*, 1989, Vol.8, No. 2, pp. 159–169.
[8] J. Skrzypek and R. B. Hetnarski. *Plasticity and Creep*. CRC Press, 1993, 542 p.

Optimal design of cylindrical shells with elastic and rigid supports

Jaan Lellep[1], **Annika Paltsepp**[2]

Institute of Mathematics, University of Tartu
Tartu, Estonia
[1]*jaan.lellep@ut.ee,* [2]*annika.paltsepp@emu.ee*

Abstract. A large deflection analysis of inelastic circular cylindrical shells resting on elastic and rigid ring supports is developed. Optimal positions of internal supports are determined so that the integral deflection of the shell attains the minimal value. The shell is loaded by the uniform internal pressure and the axial dead load. The material of the shell is a fiber-reinforced quasi-homogeneous material obeying the yield condition suggested by Lance and Robinson.

Keywords: *cylindrical shell, optimization, additional support.*

1. Introduction

It is well known that the compliance of cylindrical shells can be decreased with the aid of stiffeners, rib-reinforcement and intermediate ring supports [1, 2]. Evidently, it is reasonable to define the positions of intermediate supports so that corresponding cost functions attain the minimum value. Optimal design of inelastic cylindrical shells with stiffeners and intermediate supports was investigated by Cinquini and Kouam [4], Lellep [7], Lellep and Paltsepp [8].

Similar problems regarding to optimization of rigid plastic beams with additional supports have been solved by Mróz and Rozvany [9] and Prager and Rozvany [10].

In the present paper a general approach is developed for determination of intermediate supports for inelastic geometrically non-linear cylindrical shells subjected to the internal pressure and the axial dead load. The intermediate supports can be both, the absolutely rigid or elastic supports. Numerical results have been obtained for inelastic shells clamped at the left-hand end and elastically supported at the other end. The additional support is assumed to be an ideal rigid support.

2. Basic assumptions and equations

The post-yield behavior of a circular cylindrical shell will be studied. The shell is loaded by the distributed internal pressure loading of intensity $P(x)$ and by the tension N applied at the right hand end of the tube. Let the origin of the coordinate axis $0x$ be located at the left hand end of the shell (Fig.1). The left end of the shell is simply supported or clamped whereas the cross-sections $x = s$ and $x = l$ are elastically supported with the rigidities of supports μ_s and μ, respectively.

It is assumed that the location of the intermediate support is not fixed. We are looking for the best position of this support so that the flexibility of the tube is as small as possible. However, one can not say what is the best measure of structural flexibility. In the present paper for this purpose the functional to be minimized

$$J = \int_0^l W^r \, dx + G(M(x_0), Q(x_1), W'(x_2), s) \tag{1}$$

will be used. Here $W = W(x)$ stands for the transverse deflection of the shell and M is the bending moment, Q – shear force. In what follows we are looking for the minimum of (1) so that the equilibrium equations with boundary and intermediate conditions, the associated gradientality law with the yield condition, also the inequalities

$$P - P_0 \geq 0, \qquad P - P_1 \geq 0 \tag{2}$$

are satisfied.

Here P_0 and P_1 stand for the load carring capacity of the left-hand and right-hand parts of the shell, respectively.

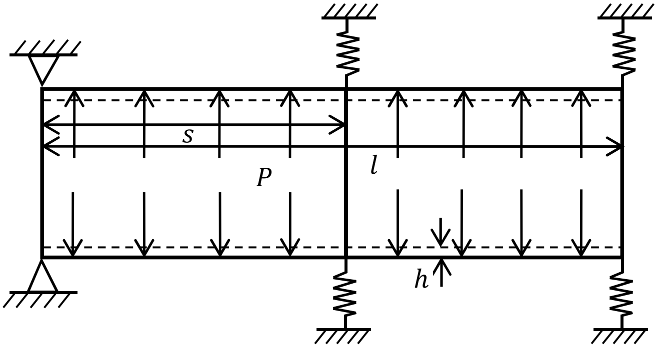

Fig. 1. A shell with additional support.

In (1) G is a given function and x_0, x_1, x_2 fixed points on the interval $(0, l)$ whereas r is a real number. The cost function (1) admits to study different problems from the unique point of view. If, for instance, the first term is absent in (1) and $G = M(x_0)$ then the problem consists in the minimization of the bending moment at $x = x_0$. Alternatively, if $G = 0$ and $r = 1$, one has to minimize the mean deflection of the shell.

It is assumed that the material of the shell is an ideal rigid plastic material obeying the piece wise linear yield condition suggested by Lance and Robinson [6] for a unidirectionally reinforced material. An approximation to be used in the present paper can be defined by inequalities

$$|M| \leq \frac{\alpha}{k} M_0, \qquad |N_2| \leq k N_0 \tag{3}$$

where N_2 is the hoop force and

$$M_0 = \sigma_0 h H, \qquad N_0 = 2\sigma_0 h, \qquad \alpha = \frac{\sigma_1}{\sigma_0}. \tag{4}$$

Here σ_1 and σ_0 stand for the yield stresses of the fibers and matrix, respectively. It is assumed herein that the shell wall is of sandwich-type with thickness H and h being the thickness of carrying layers.

As it might be expected the exact yield surface strongly depends on the orientation of fibers in the matrix material. In the present paper study two particular cases of the reinforcement will be considered. These are the axial reinforcement when fibers are directed along the axis of the tube (in this case the parameter $k = 1$) and the hoop reinforcement, respectively. In the latter case the attribute $k = \alpha$.

The equilibrium equations of a shell element can be presented as (see Kaliszky [5], Chakrabarty [3], Lellep and Paltsepp [8]) $N_1 = N$ and

$$\frac{dM}{dx} = Q \tag{5}$$

and

$$\frac{dQ}{dx} = N_1 \frac{d^2W}{dx^2} - \frac{N_2}{R} + P \tag{6}$$

where $N_1 = N$, N_2 are the membrane forces and Q the shear force. Note that (5) and (6) hold good under the condition of axial symmetry.

Boundary conditions are at the left-hand end

$$M(0) = 0, \qquad W(0) = 0 \tag{7}$$

in the case of the simply supported edge,

$$M(0) = \frac{\alpha}{k} M_0, \qquad W(0) = 0 \tag{8}$$

in the case of clamped end and at the right end

$$M(l) = 0, \; Q(l) = \mu W(l). \tag{9}$$

At the intermediate point $x = s$ one has

$$[Q(s)] = \mu_s W(s), \qquad M(s) = M_0 \frac{\alpha}{k}, \tag{10}$$

where square brackets denote finite jumps of corresponding variables.

Thus

$$[Q(s)] = Q(s+0) - Q(s-0). \tag{11}$$

3. Limit loads

Evidently, the onset of plastic yielding is associated with the kinematically admissible velocity field prescribed in Fig. 2. According to Fig. 2 at cross-sections $x = 0$ (in the case of a clamped edge) and $x = s$, also at $x = a$ plastic hinges are located. Thus

$$M(0) = \frac{\alpha}{k} M_0, \qquad M(a) = -\frac{\alpha}{k} M_0, \qquad M(s) = \frac{\alpha}{k} M_0, \qquad Q(a) = 0. \tag{12}$$

The refined analysis shows that the stress-strain state of the shell corresponds to yield regime

$$N_2 = kN_0 \tag{13}$$

for each $x \in (0, l)$. It can be shown that (see Lellep and Paltsepp [8], Chakrabarty [3]) $W''(x) = 0$ between the hinges. Thus according to (5), (6), (13) one has

$$\frac{d^2M}{dx^2} = -\frac{kN_0}{R} + P. \tag{14}$$

Integrating (14) for $x \in (0, s)$ and satisfying (12) one obtains

$$M = \frac{1}{2}\left(P - \frac{kN_0}{R}\right)(x-a)^2 - M_0 \frac{\alpha}{k}. \tag{15}$$

Due to the first requirement in (12)

$$P_0 = \frac{kN_0}{R} + \frac{4\alpha}{a^2 k} M_0. \tag{16}$$

Similarly one can see that

$$M = \frac{1}{2}\left(P - \frac{kN_0}{R}\right)(x - l)^2 \tag{17}$$

for $x \in (s, l)$. Thus $a = s/2$ and

$$P_1 = \frac{kN_0}{R} + \frac{2M_0\alpha}{k(s - l)^2}. \tag{18}$$

4. Stress-strain state of the shell

In the post-yield stage the flow regime (13) holds good for each $x \in (0, l)$. However, in the regions $a_j \le x \le b_j$ the stress-strain state of the shell corresponds to the intersections of faces of the yield surface (3).

In the regions

$$M = \frac{\alpha}{k} M_0, \qquad NW'' - \frac{kN_0}{R} + P = 0. \tag{19}$$

Outside of the regions (a_j, b_j) $W'' = 0$.

Integrating the equations (5), (6) and taking (7)–(13), (19) into account one has the distribution of shear forces

$$Q = \begin{cases} \left(P - \dfrac{kN_0}{R}\right)(x - a_0), & x \in (0, a_0), \\ 0, & x \in (a_0, b_0), \\ \left(P - \dfrac{kN_0}{R}\right)(x - b_0), & x \in (b_0, s), \end{cases} \tag{20}$$

for $x \in (0, s)$ and

$$Q = \begin{cases} \left(P - \dfrac{kN_0}{R}\right)(x - a_1), & x \in (s, a_1), \\ 0, & x \in (a_1, b_1), \\ \left(P - \dfrac{kN_0}{R}\right)(x - b_1), & x \in (b_1, l), \end{cases} \tag{21}$$

for $x \in (s, l)$. Integrating once more leads to the distribution of radial bending moments

$$M = \begin{cases} \dfrac{1}{2}\left(P - \dfrac{kN_0}{R}\right)(x - a_0)^2 - M_0\dfrac{\alpha}{k}, & x \in (0, a_0), \\ -M_0\dfrac{\alpha}{k}, & x \in (a_0, b_0), \\ \dfrac{1}{2}\left(P - \dfrac{kN_0}{R}\right)(x - b_0)^2 - M_0\dfrac{\alpha}{k}, & x \in (b_0, s), \end{cases} \tag{22}$$

for $x \in (0, s)$ and

$$M = \begin{cases} \frac{1}{2}\left(P - \frac{kN_0}{R}\right)(x - a_1)^2 - M_0\frac{\alpha}{k}, & x \in (s, a_1), \\ -M_0\frac{\alpha}{k}, & x \in (a_1, b_1), \\ \frac{1}{2}\left(P - \frac{kN_0}{R}\right)(x - b_1)^2 - M_0\frac{\alpha}{k}, & x \in (b_1, l) \end{cases} \tag{23}$$

for $x \in (s, l)$.

It is worthwhile to mention that (20)–(23) hold good equally in the cases when the left-hand end of the shell is clamped or simply supported. Moreover, one can use these relations for both, axial and hoop reinforcement of materials.

For determination of deflections one can use (5), (6) with (20)–(23). Substituting (13) and (20)–(21) in (6) one can see that

$$\frac{d^2W}{dx^2} = \begin{cases} \frac{1}{N}\left(\frac{kN_0}{R} - P\right), & x \in (a_j, b_j), \\ 0, & x \,\overline{\in}\, (a_j, b_j). \end{cases} \tag{24}$$

Integrating (24) and satisfying the boundary conditions (8)–(10) one easily obtains for $x \in (0, s)$

$$\frac{dW}{dx} = \begin{cases} A_0, & x \in (0, a_0), \\ \left(P - \frac{kN_0}{R}\right)(x - a_0) + A_0, & x \in (a_0, b_0), \\ B_0, & x \in (b_0, s), \end{cases} \tag{25}$$

where due to the continuity of the displacement derivate at $x = b_0$ (here A_0, B_0 are arbitrary constants)

$$B_0 = A_0 + \left(P - \frac{kN_0}{R}\right)(b_0 - a_0). \tag{26}$$

The integration of (25) yields the displacement field

$$W = \begin{cases} A_0x, & x \in (0, a_0), \\ \frac{1}{2}\left(P - \frac{kN_0}{R}\right)(x - a_0)^2 + A_0x, & x \in (a_0, b_0), \\ B_0(x - s) + \frac{1}{\mu_s}[Q(s)], & x \in (b_0, s), \end{cases} \tag{27}$$

where boundary conditions (8) and (10) are taken into account. Since the deflection is continuous at $x = b_0$ one has

$$A_0 = \frac{1}{s}\left(P - \frac{kN_0}{R}\right)\left\{\frac{1}{\mu_s}(b_0 - a_1) - \frac{1}{2}(b_0 - a_0)(2s - a_0 - b_0)\right\}. \tag{28}$$

In the similar way accounting for (24) one obtains for $x \in (s, l)$

$$\frac{dW}{dx} = \begin{cases} A_1, & x \in (s, a_1), \\ \left(P - \frac{kN_0}{R}\right)(x - a_1) + A_1, & x \in (a_1, b_1), \\ B_1, & x \in (b_1, l), \end{cases} \tag{29}$$

where A_1, B_1 are arbitrary constants. Making use of the continuity of the deflection slope at $x = b_1$ one can see that

$$B_1 = A_1 + \left(P - \frac{kN_0}{R}\right)(b_1 - a_1). \tag{30}$$

Substituting (30) in (29) and integrating with requirements (9), (10) leads to the deflection distribution

$$W = \begin{cases} A_1(x - s) + \dfrac{[Q(s)]}{\mu_s}, & x \in (s, a_1), \\ \dfrac{1}{2}\left(P - \dfrac{kN_0}{R}\right)(x - a_1)^2 + A_1(x - s) + \dfrac{[Q(s)]}{\mu_s}, & x \in (a_1, b_1), \\ \left(\left(P - \dfrac{kN_0}{R}\right)(b_1 - a_1) + A_1\right)(x - l) + \dfrac{Q(l)}{\mu}, & x \in (b_1, l). \end{cases} \tag{31}$$

Due to the continuity of the deflection W at $x = b_1$ on has

$$A_1 = \frac{1}{l - s}\left\{\frac{1}{\mu}(l - b_1) - \frac{1}{\mu_s}(b_0 - a_1) + \frac{1}{2}(a_1 + b_1 - 2l)\right\}\left(P - \frac{kN_0}{R}\right). \tag{32}$$

The relations (22), (23) with (8)–(10) furnish the same expressions for quantities a_j, b_j $(j = 0,1)$ as in the case of rigid supports (see Lellep and Paltsepp [8]).

5. Optimal location of the intermediate support

Let us consider the case where $G = 0$ and $r = 1$ in (1) in a greater detail. Making use of (26)–(32) one can present the cost function as

$$\begin{aligned} J = {} & \frac{1}{2}A_0 b_0^2 - \frac{1}{2}B_0(b_0 - s)^2 + \frac{1}{2}A_1\{(b_1 - s)^2 - (b_1 - l)^2\} \\ & + \frac{1}{6}\left(P - \frac{kN_0}{R}\right)\{(b_0 - a_0)^3 + (b_1 - a_1)^3 + (b_1 - a_1)(l - b_1)\} \\ & + \frac{[Q(s)]}{\mu_s}(b_1 - b_0) + \frac{Q(l)}{\mu}(l - b_1), \end{aligned} \tag{33}$$

where $[Q(s)]$ and $Q(l)$ can be defined from (21) and A_0, B_0, A_1 are given by (26), (28), (32).

The constrained minimization problem with cost function (33) and constraints (2) is solved numerically. Evidently, the current problem involves as a particular case the problem of optimal location of absolutely rigid supports treated earlier by the authors [8]. In the case of rigid supports μ_s or μ (or both) tend to infinity. In this case corresponding terms in (33) vanish.

The results of calculations are presented in Fig. 2–Fig. 5.

Fig. 2–Fig. 5 correspond to $\omega = 8$; $n_1 = 0.1$; $\alpha = k = 1$. In Fig. 4–Fig. 5 $s = 0.6$. The distributions of displacements and bending moments are presented in Fig. 2 and Fig. 3, respectively for different locations of the intermediate support.

The deflections and the bending moments versus the pressure loading are depicted in Fig. 4 and Fig. 5. Here $s = 0.6$. It can be seen from Fig. 4, 5 that the values of the moment and the transverse deflection increase with the loading, as might be expected.

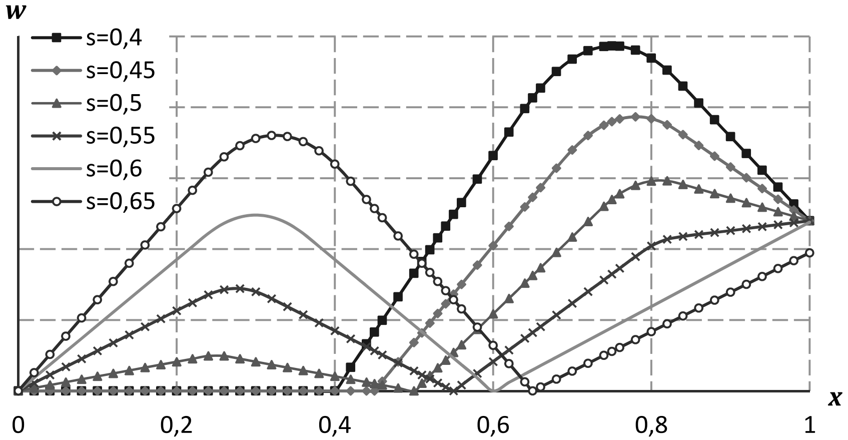

Fig. 2. Deflections of the shell for different values of s.

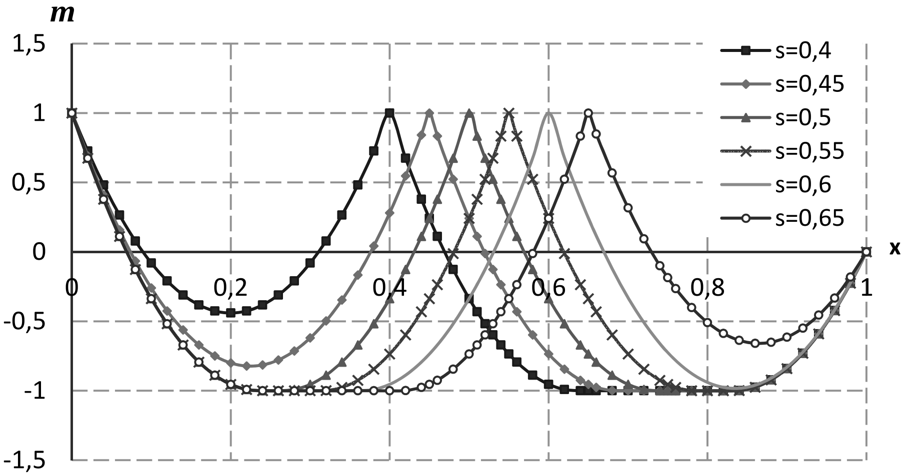

Fig. 3. Bending moments of the shell for different values of s.

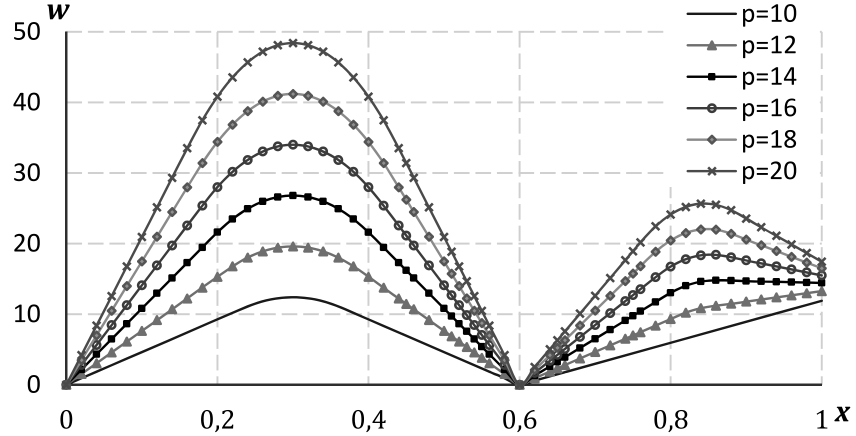

Fig. 4. Deflections for different loadings.

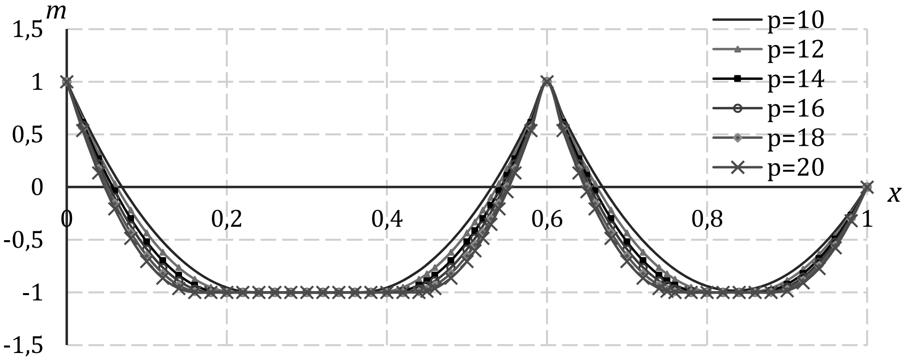

Fig. 5. Bending moments for different loadings.

6. Concluding remarks

A method for optimization of cylindrical shells with additional supports is developed. The supports may be elastic or absolutely rigid supports.

The optimization problem is posed in the general form so that the previously treated problems with rigid supports are particular cases the obtained results coincide with the earlier results.

Acknowledgements

The supports from the grant ETF9110 “Optimization of structural elements” and from the institutional research funding IUT20-57 of the Ministry of Education and Research are gratefully acknowledged.

References

[1] N.V. Banichuk. *Problems and Methods of Optimal Structural Design*. Plenum Press, New York, 1983, 313 p.

[2] A. Biron. Limit analysis of cylindrical shells with longitudinal rib reinforcements, *International Journal of Solids and Structures*, Vol. 6, No. 7, 1970, pp. 893–908.

[3] J. Chakrabarty. *Theory of Plasticity*. Elsevier, 2006, 895 p.

[4] C. Cinquini and M. Kouam. Optimal plastic design of stiffened shells. *International Journal of Solids and Structures*, Vol. 19, No. 9, 1983, pp. 773–783.

[5] S. Kaliszky. *Plasticity. Theory and Engineering Applications*. Elsevier, Amsterdam, 1989, 505 p.

[6] R.H. Lance and D.V. Robinson. Limit analysis of ductile fiber-reinforced structures. *Journal of Engineering Mechanics, Proceedings of ASCE*, Vol. 98, No. 1, 1972, pp. 195–209.

[7] J. Lellep. Optimal location of additional supports for plastic cylindrical shells subjected to impulsive loading. *International Journal of Non-Linear Mechanics*, Vol. 19, No.4, 1984, pp. 323–330.

[8] J. Lellep and A. Paltsepp. Optimization of inelastic cylindrical shells with internal supports, *Structural and Multidisciplinary Optimization*, Vol. 41, No. 6, 2010, pp. 841–852.

[9] Z. Mroz and G. Rozvany. Optimal design of structures with variable support positions. *Journal of Optimization. Theory and Applications*, Vol. 15, No. 1, 1975, pp. 85–101.

[10] W. Prager and G. Rozvany. Plastic design of beams: optimal locations of supports and steps in yield moment. *International Journal of Mechanical Sciences*, Vol. 17, No. 10, 1975, pp. 627–631.

Elastic plastic bending of annular plates

Jaan Lellep[1], Julia Polikarpus[2]

Institute of Mathematics, University of Tartu
Tartu, Estonia
[1]jaan.lellep@ut.ee, [2]julia.polikarpus@ut.ee

Abstract. Bending of annular plates subjected to uniformly distributed transverse pressure is studied. The plates are simply supported at the outer edge and absolutely free at the inner edge. The plates are made of an ideal elastic plastic material which obeys Tresca's yield condition and the associated flow law. The exact solution for the bending problem satisfying the equilibrium equations, yield condition and the gradientality law is derived.

Keywords: *annular plate, inelastic bending, plasticity.*

1. Introduction

The estimation of the displacement field of axisymmetric plates prior to the collapse state has been the concern of several authors (see Onat, Haythornthwaite [6]; Hodge [3]; Save, Massonet, Saxcé [8]; Cooper and Shifrin [1]). Sherbourne and Srivastava [9], also Tekinalp [10] developed solution techniques for circular plates subjected to the transverse loading in the case of materials obeying the Tresca's yield condition, Turvey [11], Eason [2] focused their attention to the Mises material. In the previous paper by the authors [5] axisymmetric deformations of circular plates are studied under the assumption that the material is an elastic plastic one and it obeys the diamond yield condition on the plane of principal moments. In [4] annular plates are treated.

In the present paper the elastic plastic bending of annular plates is investigated in the case of a Tresca's material. The plates under consideration are loaded by the uniform transverse pressure. The plates are simply supported at the outer edge and free at the inner edge. The analysis is based on a geometrically linear model, large deflections are not considered in the present study.

2. Problem formulation

Elastic plastic deformations of an annular plate with radii a and R will be studied. The plate is subjected to the distributed transverse loading of intensity $P = P(r)$, where r is the current radius. Assume that the outer edge is simply supported whereas the inner edge of the plate is completely free. Therefore, at the outer edge the transverse deflection W and the radial bending moment M_1 must vanish. The radial bending moment is zero at the inner edge, as well. Thus, the boundary conditions are at the outer edge

$$W(R) = 0, \quad M_1(R) = 0 \tag{1}$$

and at the inner edge

$$M_1(a) = 0, \quad Q(a) = 0 \tag{2}$$

where Q is the shear force. Note that the hoop moment M_2 can take arbitrary values at the both edges. For the sake of simplicity it is assumed that the cross sections of the plate are of sandwich type. Thus the plate consists of two rims of thickness h and of the core material between them. Let the total thickness of the plate be H.

The aim of the paper is to determine the distributions of bending moments M_1, M_2 and the transverse deflection W for each value of the transverse load. It is expected that in the range of low loadings the plate is fully elastic and with the subsequent increase of the load level elastic plastic deformations occur.

3. Elastic stage of deformation

In the case of low stress level the plate remains elastic and the Hooke's law holds good. The latter can be presented as (see Reddy [7], Hodge [3])

$$\begin{aligned} M_1 &= D(\varkappa_1 + \nu\varkappa_2) \\ M_2 &= D(\varkappa_2 + \nu\varkappa_1) \end{aligned} \tag{3}$$

where $\varkappa_1, \varkappa_2$ stand for curvatures in the radial and circumferential directions, e. g.

$$\varkappa_1 = -\frac{d^2W}{dr^2}, \varkappa_2 = -\frac{1}{r}\frac{dW}{dr}. \tag{4}$$

In (3) D is the stiffness of the plate. In the case of a sandwich plate

$$D = \frac{EhH^2}{2(1-\nu^2)}. \tag{5}$$

where E is the Young's modulus and ν – the Poisson's ratio.
The stresses are coupled with external loads by the equilibrium equations (Save et al [8])

$$\frac{d}{dr}(rM_1) - M_2 - rQ = 0 \tag{6}$$

and

$$\frac{d}{dr}(rQ) = -P(r)r. \tag{7}$$

In the present paper it is assumed that $P(r) = const$. This admits to integrate the last equation. The solution of (7) satisfying the boundary condition (2) can be presented as

$$Q = -\frac{P(r^2 - a^2)}{2r}. \tag{8}$$

Differentiating (6) and substituting (7) and (3), (4) in (6) leads to the known plate bending equation

$$D\frac{d}{dr}\left\{r\frac{d}{dr}\left[\frac{1}{r}\frac{d}{dr}\left(r\frac{dW}{dr}\right)\right]\right\} = rP \tag{9}$$

whose general solution satisfying (1) is

$$W = \frac{P(r^4 - R^4)}{64D} + C_1(r^2 \ln r - R^2 \ln R) + C_2(r^2 - R^2) + C_3 \ln\frac{r}{R}, \tag{10}$$

C_1–C_3 being arbitrary constants.

However, calculating the shear force Q from (6) making use of (3), (4), (10) and comparing with (8) one can see that

$$C_1 = -\frac{Pa^2}{8D}. \tag{11}$$

Substituting (10) in (3) one can determine the bending moments

$$M_1 = -\frac{Pr^2\,(3+\nu)}{16} + \frac{Pa^2[2(1+\nu)\ln r + 3 + \nu]}{8} - D\left[2C_2(1+\nu) + \frac{C_3(\nu-1)}{r^2}\right] \tag{12}$$

and

$$\begin{gathered} M_2 = -\frac{Pr^2\,(1+3\nu)}{16} + \frac{Pa^2[2(1+\nu)\ln r + 1 + 3\nu]}{8} - \\ -D\left[2C_2(1+\nu) + \frac{C_3(1-\nu)}{r^2}\right]. \end{gathered} \tag{13}$$

Applying the boundary conditions (1), (2) to (12) one can define

$$\begin{aligned} C_2 &= \frac{P}{32D(1+\nu)(R^2-a^2)}\{(3+\nu)(a^4-R^4) \\ &+2a^2[(R^2-a^2)[2(1+\nu)\ln a + 3 + \nu] - 2R^2(1+\nu)(\ln a - \ln R)]\}, \\ C_3 &= \frac{Pa^2R^2[(3+\nu)(R^2-a^2) + 4a^2(1+\nu)(\ln a - \ln R)]}{16D(\nu-1)(R^2-a^2)}. \end{aligned} \tag{14}$$

4. Elastic plastic stage of deformation

The plate remains pure elastic until the stress profile lies entirely inside the Tresca's yield hexagon (Fig. 1). During the elastic stage the inequalities

$$|M_1| \le M_0,\ |M_2| \le M_0,\ |M_1 - M_2| \le M_0 \tag{15}$$

are satisfied as strict inequalities.

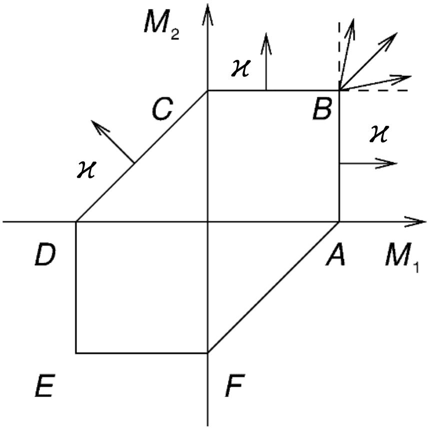

Fig. 1. Tresca's yield hexagon.

The elastic plastic stage begins at the load level $P = P_1$ when the stress profile reaches to the yield locus. The analysis shows that the stress profile reaches to the side $M_2 = M_0$ of the yield hexagon.

The maximum of the hoop moment is achieved at the inner edge of the plate and the quantity P_1 can be calculated from the equation $M_2(a) = M_0$. Therefore,

$$P_1 = \frac{8M_0(R^2 - a^2)}{R^4(3+\nu) + 4a^2R^2[(1+\nu)(\ln a - \ln R) - 1] + a^4(1-\nu)}. \tag{16}$$

During the elastic plastic stage the plate is divided into two parts. In the inner part (a, y) plastic deformations take place whereas the region (y, R) remains elastic. Let us consider the regions separately.

4.1. Plastic region, $r \in (a, y)$

For $r \in (a, y)$ the stress profile lies on the side $M_2 = M_0$ of the yield hexagon (Fig. 1). Substituting $M_2 = M_0$ in (6) and taking (8) into account one obtains for $r \in (a, y)$

$$rM_1 - rM_0 + \frac{P}{2}\left(\frac{r^3}{3} - a^2 r\right) = C, \tag{17}$$

C being an arbitrary constant. Due to the boundary condition (2)

$$C = -aM_0 - \frac{Pa^3}{3} \tag{18}$$

and (17) can be put into the form

$$M_1 = \frac{r-a}{r}\left[M_0 - \frac{P(r^2 + ar - 2a^2)}{6}\right]. \tag{19}$$

It is worthwhile to emphasize that (19) holds good for $r \in [a, y]$.
In the plastic region the associated flow law must be taken into account. The latter means that the vector of strain rate components is normal to the yield surface. However, in the frameworks of the linear theory of plasticity and proportional loading the flow law can be integrated with respect to time and therefore, one can use the gradientality law in the form where strain rates are replaced with corresponding strain components. In the general case this theory, called deformation-type theory of plasticity, leads to approximate solutions.

In the case of the horizontal side BC of the yield hexagon (Fig. 1) according to the gradientality law one has $\varkappa_1 = 0, \varkappa_2 \geq 0$. Thus, $d^2\, W/dr^2 = 0$ and

$$W = Ar + B \tag{20}$$

where A and B are arbitrary constants.

4.2. Elastic region, $r \in (y, R)$

In the elastic region of the plate the relations (10)–(13) hold good. However, (14) is not valid. For determination of unknown constants C_2, C_3 and A, B one can use the boundary conditions at $r = R$, also the continuity requirements of quantities W, dW/dr, M_1, M_2 at $r = y$.

The requirements $M_1(R) = 0$ and $M_2(y) = M_0$ give with the help of (12), (13)

$$-\frac{PR^2\,(3+\nu)}{16} + \frac{Pa^2[2(1+\nu)\ln R + 3 + \nu]}{8} - D\left[2C_2(1+\nu) + \frac{C_3(\nu - 1)}{R^2}\right] = 0 \tag{21}$$

and

$$-\frac{Py^2\,(1+3\nu)}{16}+\frac{Pa^2[2(1+\nu)\ln r+1+3\nu]}{8}-D\left[2C_2(1+\nu)+\frac{C_3(1-\nu)}{y^2}\right] \tag{22}$$
$$=M_0.$$

The continuity of the radial bending moment at $r = y$ with (12) and (19) furnishes the relation

$$-\frac{Py^2\,(3+\nu)}{16}+\frac{Pa^2[2(1+\nu)\ln y+3+\nu]}{8}-D\left[2C_2(1+\nu)+\frac{C_3(\nu-1)}{y^2}\right]-$$
$$-\frac{y-a}{y}\left[M_0-\frac{P(y^2+ay-2a^2)}{6}\right]=0. \tag{23}$$

Due to the continuity of the deflection and its slope one has making use of (10) and (20)

$$A=\frac{Py^3}{16D}-\frac{Pa^2y(2\ln y+1)}{8D}+2C_2y+\frac{C_3}{y} \tag{24}$$

and

$$\frac{P(y^4-R^4)}{64D}-\frac{Pa^2(y^2\ln y-R^2\ln R)}{8D}+C_2(y^2-R^2)+C_3\ln\frac{y}{R}-Ay-B=0. \tag{25}$$

From (21), (22) one can easily define

$$C_2=\frac{-Py^3(1+3\nu)+6Pa^2y[(\nu+1)\ln y+\nu]+12M_0(a-2y)+4Pa^3}{48D(1+\nu)y}$$
$$C_3=\frac{y[Py^3(1+3\nu)-6Pa^2y(1+\nu)+8a(3M_0+Pa^2)]}{48D(\nu-1)}. \tag{26}$$

The equation (25) admits to define

$$B=\frac{P[-3y^4+8a^2y^2(\ln y+1)-R^2(R^2-8a^2\ln R)]}{64D}-$$
$$-(y^2+R^2)C_2+\left(\ln\frac{y}{R}-1\right)C_3. \tag{27}$$

Substituting C_2, C_3 from (26) in (23) one obtains the equation

$$\frac{PR^2\,(3+\nu)}{16D}-\frac{Pa^2[2(1+\nu)\ln R+3+\nu]}{8D}+$$
$$+\frac{-Py^3(1+3\nu)+6Pa^2y[(\nu+1)\ln y+\nu]+12M_0(a-2y)+4Pa^3}{24Dy}+ \tag{28}$$
$$+\frac{y[Py^3(1+3\nu)-6Pa^2y(1+\nu)+8a(3M_0+Pa^2)]}{48DR^2}=0.$$

The equation (28) serves for determination of the quantity y for fixed load intensity P.

5. Numerical results

The equation (28) is solved numerically making use of the computer code *Mathematica*. The results of calculations are presented in Table 1 and Fig. 2–Fig. 3 in the case $a = 0.3R$. Calculations carried out showed that the plastic region expands with the growth of the load intensity. The transverse deflections of the plate are depicted in Fig. 2 for different values of the load intensity.

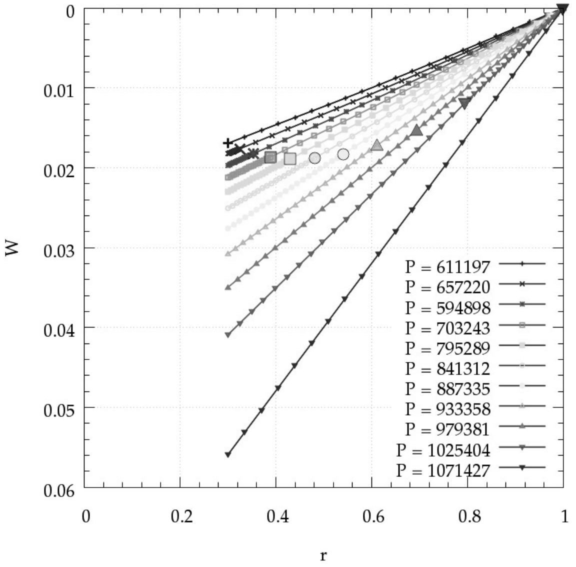

Fig. 2. Transverse deflections.

The enlarged symbols in Fig. 2 indicate the border between elastic and plastic regions. The distributions of radial bending moment M_1 are presented in Fig. 3.

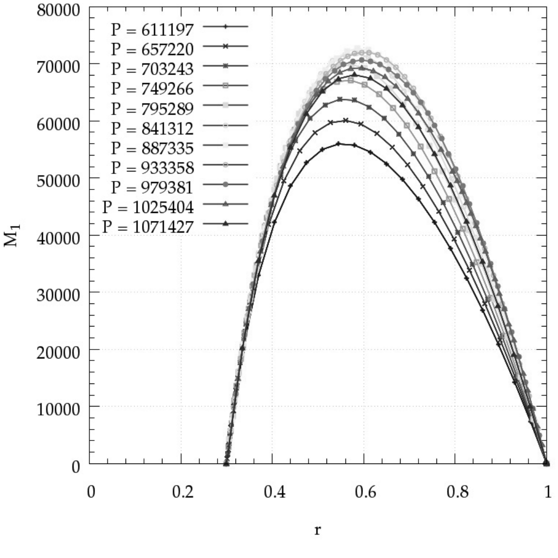

Fig. 3. Radial bending moments.

It can be seen from Fig. 3 that the distributions of bending moment are statically admissible since at each $r \in [a, R]$ corresponding values of M_1, M_2 are such that the point either lies on the side $M_2 = M_0 (= 200000$ N) of the yield hexagon or is located inside the hexagon. The elastic plastic stage of deformation is completed at the loading level where the whole plate is plastic. This situation corresponds to

$$P = P_2 = \frac{6M_0(R-a)}{R^3 + 2a^3 - 3a^2R} \tag{29}$$

and $y = R$.

6. Concluding remarks

The problem of determination of the stress strain state of annular plates is solved in the case of a Tresca's material. For the simplicity sake the model of a sandwich plate was employed. The plate under consideration is simply supported at the outer edge and absolutely free at the inner edge. Statically and kinematically admissible stress fields and distributions of displacements are constructed for the initial elastic and the subsequent elastic plastic stage of deformation.

It is shown that with increasing the intensity of external loading the plate reaches to fully plastic state.

Acknowledgements

The partial supports from the Estonian Science Foundation Grant ETF9110 “Optimization of structural elements” and from the Institutional project IUT20-57 “Structural Problems in Analysis, Algebra, and Geometry, with Applications to Numerical Analysis” of the Estonian Ministry of Education and Research are gratefully acknowledged.

References

[1] R.M. Cooper and G.A. Shifrin. An experiment on circular plates in the plastic range. *Proc. 2nd US National Congress of Applied Mechanics ASME, Ann Arbor*, 1954, pp. 527–534.

[2] G. Eason. The elastic-plastic bending of a simply supported plate. *Journal of Applied Mechanics,* Vol. 28, 1961, pp. 395–401.

[3] P.G. Hodge. *Plastic Analysis of Structures*. Krieger, New York, 1981, 425 p.

[4] J. Lellep and J. Polikarpus. Elastic plastic bending of stepped annular plates. *In: A. Zemliak, N. Mastorakis(Eds), WSEAS, Proceedings of American-Math'11*, Puerto Morelos, 2011, pp. 140–145.

[5] J. Lellep and J. Polikarpus. Elastic plastic bending of stepped circular plates. *In: J. Lellep, E. Puman (Eds), Optimization and Analysis of Structures,* Tartu, 2013, pp. 81–87.

[6] E.T. Onat and R.M. Haythornthwaite. The load-carrying capacity of circular plates at large deflections. *Journal of Applied Mechanics*, Vol. 26, 1956, pp. 49–55.

[7] J.N. Reddy. *Theory and Analysis of Elastic Plates and Shells*. CRC Press, Boca Raton, 2007, 547 p.

[8] M.A. Save, C.E. Massonet and G. De Saxce. *Plastic Limit Analysis of Plates, Shells and Disks*. Elsevier, Amsterdam, 1997, 580 p.

[9] A.N. Sherbourne and A. Srivastava. Elastic-plastic bending of restrained pin-ended circular plates. *International Journal of Mechanical Sciences*, Vol. 13, 1971, pp. 231–241.

[10] B. Tekinalp. Elastic-plastic bending of a built-in circular plate under a uniformly distributed load. *Journal of the Mechanics and Physics of Solids*, Vol. 2, No. 5, 1957, pp. 135–142.

[11] G.J. Turvey and G.T. Lim. Axisymmetric full-range analysis of transverse pressure-loaded circular plates. *International Journal of Mechanical Sciences*, Vol. 26, No. 9, 1984, pp. 489–502.

Optimal design of conical shells with stiffeners

Jaan Lellep[1], **Ella Puman**[2]

Institute of Mathematics, University of Tartu
Tartu, Estonia
[1]jaan.lellep@ut.ee, [2]ella.puman@ut.ee

Abstract. Elastic conical shells subjected to the lateral pressure are considered. The shells are furnished with a system of ring stiffeners. The locations of these stiffeners are determined so that a cost function attains its minimal value. Invoking the methods of the theory of optimal control the necessary conditions of optimality are derived for the case of an arbitrary cost function.

The optimal positions of stiffeners are established numerically in the case where the cost function coincides with the mean deflection of the shell.

Keywords: *conical shell, stiffener, optimal design, elastic shell.*

1. Introduction

The optimal design of thin-walled shells is a topic which has an essential meaning in the tehnology and in the science. The use of conical shells in the pressure vessels is studied by Ross [5].

A method for determination of optimal parameters of conical shells with piece wise constant shell wall was developed by Lellep and Puman [2, 3].

In the previous paper by the authors [3] an approach to the analysis and optimization of ring-stiffened shells based on finite elements was accomodated for truncated conical shells. Corradi et al [1], Xu, Liu and Cen [7] are established the plastic limit loads for different shells of revolution, including conical shell, making use of various numerical methods. Lin et al [4] developed an analytical prediction of the collapse load.

In the present paper a method is proposed for optimization of locations of ring stiffeners for elastic conical shells subjected to the lateral loading.

2. Formulation of the problem and basic relations

An axisymmetric conical shell of outer radius R and inner radius a will be considered. The inner edge of radius a is connected with the rigid boss whereas the outer edge of the shell is simply supported (Fig. 1). The shell is loaded by the uniformly distributed lateral loading of intensity P.

In order to deduce the flexibility the the shell is furnished with ring stiffeners. Let the thickness of the shell wall be h, the thickness of stiffeners – d and the width of stiffeners – b. Assume that the stiffeners are located for $x \in [\bar{a}_i, \bar{a}_i + b]$ where x-axis coincides with a generator of the mid surface of the conical shell. Making use of polar coordinates one can state that the stiffener is located between $r = \bar{a}_i \cos\varphi$ and $r = (\bar{a}_i + b)\cos\varphi$, φ being the angle of inclination of the generator of the cone.

The kinematics of the shell is prescibed with the help of displacements U and W. Let U be directed along the x-axis and W be orthogonal to the middle surface of the shell.

The linear deformation components are (see Soedel [6])

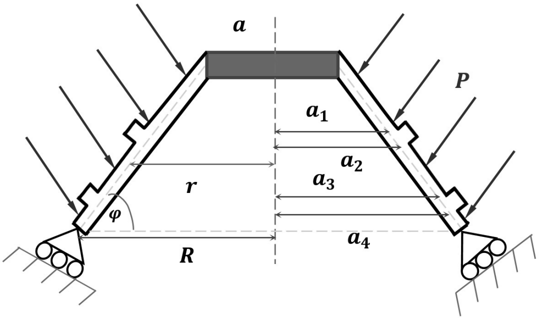

Fig. 1. Ring-stiffened conical shell.

$$\varepsilon_1 = \frac{dU}{dr}\cos\varphi,$$
$$\varepsilon_2 = \frac{1}{r}(U\cos\varphi + W\sin\varphi), \tag{1}$$

provided the stress strain state remains axisymmetric during the deformation.

Similarily, the curvatures can be presented as

$$\varkappa_1 = -\frac{d^2W}{dr^2}\cos^2\varphi,$$
$$\varkappa_2 = -\frac{1}{r}\frac{dW}{dr}\cos^2\varphi. \tag{2}$$

In the case of shells of revolution the generalized stress components contributing to the internal energy are the membrane forces N_1, N_2 and bending moments M_1, M_2. Here the subscript 1 indicates the radial direction whereas the index 2 is associated with the tangential direction.

We are looking for the design of the truncated conical shell with stiffeners for which the cost function

$$J = \int_a^R F(W, U, N_1, N_2, M_1, M_2)dr + G(a_1, \dots, a_k) \tag{3}$$

attains the minimal value so that the governing equations with boundary conditions are satisfied. In (3) F, G stands for given functions. It is assumed that F, G are continuous and differentiable with respect to their arguments. The minimization of (3) is implemented by the variation of locations of stiffeners; the aim of the paper is to determine the best positions for stiffeners.

The material of the shell is assumed to be a pure elastic material which obeys the Hooke's law. The strain components (1), (2) admit to present the Hooke's law as

$$N_1 = B\left(U'\cos\varphi + \frac{\nu}{r}(U\cos\varphi + W\sin\varphi)\right),$$
$$N_2 = B\left(\frac{1}{r}(U\cos\varphi + W\sin\varphi) + \nu U'\cos\varphi\right), \tag{4}$$

$$M_1 = -D\left(W'' \cos^2 \varphi + \frac{\nu}{r} W' \cos^2 \varphi\right),$$
$$M_2 = -D\left(\frac{W'}{r} \cos^2 \varphi + \nu W'' \cos^2 \varphi\right).$$

In (4) prims denote the differentiation with respect to the current radius r and

$$D = \frac{Eh^3}{12(1-\nu^2)}, B = \frac{Eh}{1-\nu^2}. \tag{5}$$

where E and ν are Young modulus and Poisson ratio, respectively. The equilibrium equations of a shell element have the form

$$\begin{gathered} (rN_1)' = N_2, \\ (rM_1)' - M_2 + rN_1 \frac{\sin \varphi}{\cos^2 \varphi} + \frac{P(r^2 - a^2)}{2r \cos^2 \varphi} = 0. \end{gathered} \tag{6}$$

The governing equations (4), (6) can be presented in the form of equations of the first order as follows

$$\begin{aligned} W' &= Z, \\ Z' &= -\frac{M_1}{D \cos^2 \varphi} - \frac{\nu}{r} Z, \\ U' &= \frac{N_1}{D \cos \varphi} - \frac{\nu}{r}(U + W \tan \varphi), \\ N_1' &= \frac{1}{r}(N_2 - N_1), \\ M_1' &= \frac{1}{r}(M_2 - M_1) - N_1 \frac{\sin \varphi}{\cos^2 \varphi} - \frac{P(r^2 - a^2)}{2r \cos^2 \varphi} \end{aligned} \tag{7}$$

and a system of algebraic equations from where one can define

$$\begin{aligned} N_2 &= \nu N_1 + \frac{B}{r}(1 - \nu^2)(U \cos \varphi + W \sin \varphi), \\ M_2 &= \nu M_1 + \frac{D}{r}(1 - \nu^2) Z \cos^2 \varphi. \end{aligned} \tag{8}$$

In (7) Z is in auxiliary variable defined by the first equation in (7). Introducing the notation

$$y_1 = W, y_2 = Z, y_3 = U, y_4 = N_1, y_5 = M_1 \tag{9}$$

one can present (7) briefly as

$$y_i' = f_i(\vec{y}) \tag{10}$$

where f_i $(i = 1, \ldots, 5)$ denote the right-hand sides of equations (7), provided N_2 and M_2 are substituted from (8) to (7).

The boundary conditions for (10) are

$$y_1(a) = 0, y_2(a) = 0, y_1(R) = 0, y_5(R) = 0. \tag{11}$$

The problem defined by (3), (9)–(11) can be considered as a variational problem of the theory of optimal control.

It is reasonable to assume that the state variables satisfy the additional constraint

$$\int_{a}^{R} S(a_1, \dots, a_k, \vec{y})\, dr = K_0 \tag{12}$$

where K_0 is a given constant and S a given function.

3. Optimality conditions

In order to get the necessary conditions of optimality let us consider an augmental functional

$$J_* = G(\vec{a}) + \sum_{j=0}^{k} \int_{a_j}^{a_{j+1}} \left\{ F(\vec{y}) + \psi_0 S + \sum_{i=1}^{5} \psi_i \big(y_i' - f_i(\vec{y}) \big) \right\} dr \tag{13}$$

where $\psi_0 = const$ and $\psi_i(r)$ $(i = 1, \dots, 5)$ are adjoint variables. Here $a_0 = a$ and $a_{k+1} = R$.

Calculating the total variation of (13) and equalizing it to zero one obtains the adjoint system

$$\psi_i' = -\frac{\partial H}{\partial y_i}; i = 1, \dots, 5 \tag{14}$$

with transversality conditions

$$\begin{gathered} \psi_3(a) = \psi_4(a) = \psi_5(a) = 0, \\ \psi_2(R) = \psi_3(R) = \psi_4(R) = 0. \end{gathered} \tag{15}$$

In (14) the Hamilton function has the form

$$H = -F - \psi_0 S + \sum_{i=1}^{5} \psi_i \big(f_i(y) \big). \tag{16}$$

For determination of parameters a_j $(j = 1, \dots, k)$ one obtains the equations

$$\frac{\partial G}{\partial a_j} + \left[H(a_j) \right] = 0; j = 1, \dots, k. \tag{17}$$

In (17) the square brakets denote finite jumps of correspondung quantities, e.g.

$$\left[H(a_j) \right] = H(a_j + 0) - H(a_j - 0). \tag{18}$$

4. Numerical results and discussion

Numerical results have been obtained for shells with one and two stiffeners. The results of calculations are presented in Fig. 2–3 and Table 1.

The distributions of tranverse deflections are presented in Fig. 2–3 for the shell with

$$h_0 = 0.025\text{m}; h_1 = 0.05\text{m}; R = 1\text{m}; E = 2.1 \cdot 10^{11}\ \text{Pa}; \nu = 0.3; P = 5 \cdot 10^{10}\text{Pa}.$$

The lowest curve in Fig. 2 corresponds to the optimal positions of stiffeners whereas other solid lines are associated with $a_1 = 0.65$ and $a_1 = 0.85$. The dashed lines correspond to the shell without stiffeners.

Optimal values of parameters for the shell with the single stiffener are accomodated in the Table 1. Here V stands for the optimal material volume and S_{opt} is the optimal value of the cost function. In the last column of Table 1 the values of the coefficient of effectivity e are presented. It can be seen from Table 1 that the value of the cost function can be reduced more than two times.

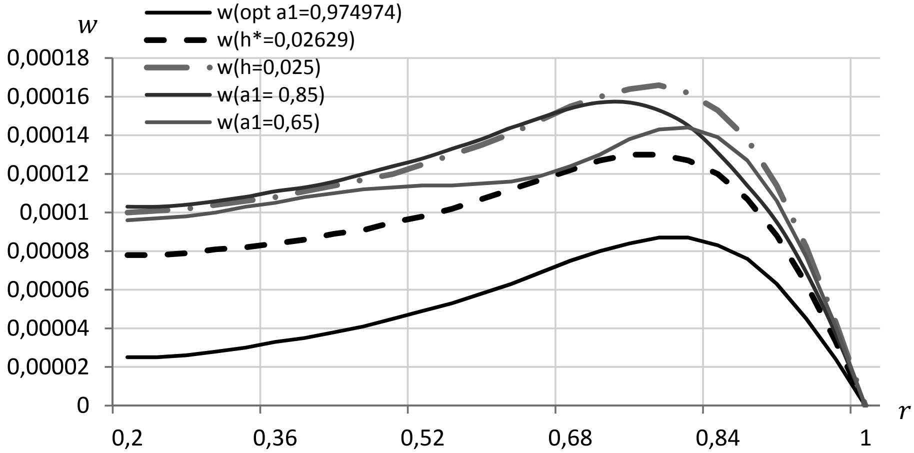

Fig. 2. Transverse deflections for shell with single stiffener, $a = 0.2\text{m}, \varphi = 36°$.

Table 1. Optimal locations for the stiffener.

a	a_1	S_{opt}	h_*	V	S_{const}	e
0.1	0.963906	0.002855	0.026233	0.025971	0.006914	0.412963
0.2	0.967998	0.002537	0.026277	0.025226	0.005805	0.436963
0.3	0.971999	0.002168	0.026352	0.023981	0.004625	0.468724
0.4	0.963996	0.001750	0.026453	0.022221	0.003487	0.501592
0.5	0.969900	0.001080	0.026637	0.019978	0.002456	0.441521
0.6	0.960000	0.001070	0.026899	0.017216	0.001496	0.715097

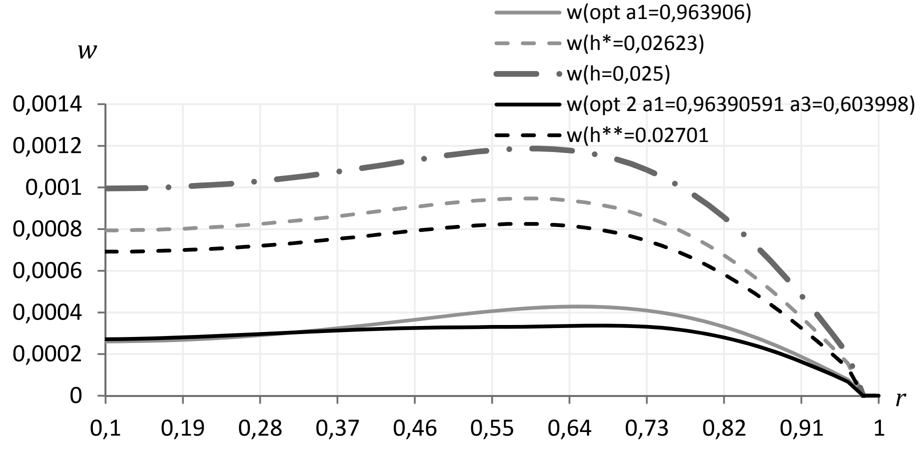

Fig. 3. Transverse deflections for shell with one and two stiffeners, $a = 0.1\text{m}, \varphi = 17°$.

The lowest curve in Fig. 3 corresponds to the optimal positions of two stiffeners whereas the other solid line is associated to the optimal position of one stiffener. The dashed lines correspond to the shell without stiffeners.

5. Concluding remarks

An optimization tehnique is developed for circular conical shells subjected to the lateral distributed loading. The flexibility of the shell is reduced by the ring-stiffeners. The shell wall and the stiffeners are assumed to be elastic. The optimal locations are determined for stiffeners so that the cost function attains its minimal value. The numerical optimization procedure is implemented for the shell with two stiffeners in the case where the measure of flexibility of the shell is its integral deflection. The case of a single stiffener is investigated as well. Calculations carried out showed that in the case of a single stiffener it's best position is located near the outer edge of the shell.

Acknowledgements

The supports from the Estonian Science Foundation through the Grant ETF9110 and from the Institutional research funding IUT20-57 of the Estonian Ministry of Education and Research are acknowledged.

References

[1] L. Corradi, L. Luzzi and P. Vena. Finite element analysis of anisotropic structures. *Computer Methods in Applied Mechanics and Engineering*, 2006, Vol. 195. pp. 5422–5436.
[2] J. Lellep and E. Puman. Optimization of inelastic conical shells with cracks. *Structural and Multidisciplinary Optimization*, Vol. 33, 2007. pp. 189–197.
[3] J. Lellep and E. Puman. Finite element analysis of ring-stiffened conical shells. *In: J. Lellep. E. Puman (Eds) Optimization and Analysis of Structures*, Tartu, 2013, pp. 88–93.
[4] J.S. Lin, X. Wang, C.Q. Fang and X. Huang. Collapse loading and energy absorption of fiber-reinforced conical shells. *Composites*, Par. B, 2015, Vol. 74, pp. 178–189.
[5] C.T.F. Ross. *Pressure Vessels under External Pressure. Statics and Dynamics*. Elsevier, London, 1990, 256 p.
[6] W. Soedel. *Vibration of Shells and Plates*. Marcel Dekker, New York, 2004, 553 p.
[7] B. Xu. Y. Liu and Z. Cen. Some developments in limit analysis solutions and structures. *Metals and Materials*, Vol. 4, No. 3, 1998, pp. 329–335.

Integral identities and rational approximations of the Crocco boundary problem

Mickhail R. Petrichenko[1], Dmitry W. Serow[2]

Peter the Great Saint-Petersburg Polytechnical University
Saint-Petersburg, Russia
[1]fonpetrich@mail.ru, [2]dimusum@yandex.ru

Abstract. Integral properties of homogeneous solutions of the Crocco boundary problem and splitting (flat) expansion for the Blasius constant approximation estimator have been considered. The first derivative $d\varphi/dh$ has been proved to have a logarithmic singularity at the point $h = 1$. Therefore the second one tends to minus zero and the function itself tends to plus zero because h tends to unity minus zero so the splitting series is not slower to diverge as compared with the harmonic one. An integral invariant existence has been proved for a uniform solution of the Crocco boundary problem. The solution exhibits the squared norm of the derivative. The condition for the distribution minimum has been established to be satisfied along the real uniform solutions of the Crocco boundary problem.

Keywords: *Crocco boundary problem, Blasius constant, Cauchy problem.*

1. Introduction

The main objective of this paper is the estimate of the Blasius constant applying some integral identities obtained from the equation Crocco. In the problems of physical content the constant determines the intensity of the transfer to a solid boundary of $D(\varphi)$,the domain change of the Crocco potential φ.

The Crocco boundary value problem is considered as following. Let $\varphi: (0,1) \to (0,a)$ is a diffeomorphism of the segments. Let us suppose that equation and boundary conditions are following:

$$2\varphi \frac{d^2\varphi}{dh^2} + h = 0, \qquad \varphi(1) = \left(\frac{d\varphi}{dh}\right)_{h=0} = 0. \tag{1}$$

The main problem is to define the Blasius constant a.

The following statements are faithful.

(i) The boundary problem (1) is equivalent to a Cauchy problem:

$$2\varphi \frac{d^2\varphi}{dh^2} + h = 0, \qquad \varphi(1) - a = \left(\frac{d\varphi}{dh}\right)_{h=0} = 0.$$

(ii) Let us suppose at the preceding statement that a is the Blasius constant.
Then the 2-diffeomorphism $\varphi = \varphi(h)$ for distribution satisfies the inequality

$$\forall\varepsilon.\ \exists\delta = \delta(\varepsilon) > 0 \longrightarrow -\delta(\varepsilon) < \varphi(1, a+\varepsilon) < \varphi(1, a-\varepsilon) < \delta(\varepsilon).$$

(iii) Otherwise, if a is the Blasius constant then $h = 1$ is a $\varphi(h)$ zero; or if $\varphi(0) = 1$, then $\varphi(H) = 0$, where $H = a^{-2/3}$.

The Blasius constant is calculated in [1] (on 32-bit (minimum)). For this purpose, a flat (planar) series and analytical continuation of the solution in a neighborhood of $h =$

$0\, are\ applied$. Ad hoc it is proved that the point $h = 1$ is a singular point for derivative $d\varphi(h)/dh$: when $h \to 1 - 0$, derivative is unbounded below.

(iv) If $h \to 1 - 0$, derivative $d\varphi(h)/dh$ has a logarithmic singularity. Indeed, the equation of the Crocco boundary problem can be written as following

$$\psi \frac{d\psi^2}{d\omega} - h = 0, \qquad \psi := \frac{d\varphi}{dh}, \qquad \omega := \log \frac{a}{\varphi} \tag{2}$$

which implies

$$\psi = \frac{d\varphi}{dh} = -\sqrt{\int_0^\omega h(\tau) d\tau}.$$

Let $h \to 1 - 0,$ then $\omega \to \infty$. □

(v) Let us consider the identity

$$\int_0^1 \left(\frac{d\varphi}{dh}\right)^2 dh = \frac{1}{4}. \tag{3}$$

The identity equation (1) is integrated, taking into account boundary conditions and the fact that $\varphi \log(a/\varphi) \to +0, \varphi \to +0$. □

(vi) Identity (3) can be rewritten as

$$\int_0^1 \psi\, dh = \int_0^\infty h(\tau)(1 - h(\tau)) d\tau = \frac{1}{4}. \tag{4}$$

In order to prove this identity the equation (2) is substituted in (3) and commuting sequence of integration is used. □

(vii) Let m is positive real number. Then the following identity takes place

$$m(1 - m) \int_0^1 h^{m-2} \varphi^2(h) dh - 2 \int_0^1 h^m \left(\frac{d\varphi}{dh}\right)^2 dh + \frac{1}{m + 2} = 0. \tag{5}$$

The identity (3) is obtained if $m = 0$. One can write if $m = 1$

$$\int_0^1 h^m \left(\frac{d\varphi}{dh}\right)^2 dh - \frac{a^2}{2} = \frac{1}{6}. \tag{6}$$

Example. Let the distribution $\varphi(h)$ is given by the binomial $\varphi(h) = a(1 - h^m)$. For determination of the constants a and m one can apply (3) and (6) so then it is obtained

$$\frac{(am)^2}{2m + 1} - \frac{1}{4}, \qquad \frac{(am)^2}{2m} - \frac{a^2}{2} - \frac{1}{6}, \qquad m^2 - \frac{9m}{2} + \frac{3}{2} = 0,$$

$$m = \frac{9 + \sqrt{57}}{4} = 4.137458609, \qquad a^2 = \frac{1}{3m - 1}, a = 0.325949538.$$

The calculation error is 1.84%. Thus the binomial approximation of the solution of the boundary problem (1) has the form

$$\varphi(h) = (1 - h^m)\sqrt{\frac{1}{3m-1}}, \tag{7}$$

where the “best” value of the exponent is $m = 4.137458609$.

2. Splitting functional series and the Blasius constant evaluation

Let us construct a solution as a series

$$\varphi(h) = a + \sum_{s\geq 1} \lambda^s \varphi_s(h), \tag{8}$$

where λ is splitting parameter. The series functional coefficients $\varphi_s(h)$ satisfy to following conditions

$$\left(\frac{d\varphi_1}{dh}\right)_{h=0} = \varphi_1(1) + \frac{a}{\lambda} = \left(\frac{d\varphi_s}{dh}\right)_{h=0} = \varphi_s(1) = 0 \ \forall s > 2\,.$$

Let us substitute the expansion series into the equation of the boundary problem (1) and let us compare the same exponents λ functional coefficients.

$$\varphi(h) = \sum_{s\geq 1} G_s(h)\,, \qquad G_1(h) = \int_h^1 dz \int_0^z t dt\,, \qquad G_s(h) = \int_h^1 dz \int_0^z \mathrm{g}_s(t)\, dt,$$

where

$$\mathrm{g}_s(h) = \sum_{r\leq s} \left(\frac{\varphi_r(h) d\varphi_r}{dh}\right)^2.$$

Let us assume $G_1 := G, G_{r_r} = G^{r^r}$ and $a = \varphi(0)$ then

$$\varphi(h) = \frac{G(h)}{1 - G(h)} = \frac{1 - h^3}{12a - 1 + h^3},$$

$$a = \frac{G(0)}{1 - G(0)} = \frac{1}{12a - 1} \Rightarrow a = \frac{1}{3}, \qquad \varphi(h) = \frac{1 - h^3}{3 + h^3}.$$

This approximation error is less than 0.4%. Of course the estimate is more accurate approximation of the binomial (7).

The convergence proof flat (splitting) series see in [1, 3].

3. Extremal properties of boundary problem solution

The existence of dissipative problem extremal properties looks quite extravagant. The equation of the limiting problem (1) is equivalent to the canonical (Hamiltonian) system

$$\frac{d}{dh}\begin{pmatrix}\varphi \\ \psi\end{pmatrix} = \begin{pmatrix}\psi \\ -\frac{h}{2}\varphi\end{pmatrix},$$

with momentum ψ and coordinate φ. On the other hand one has

$$\frac{d}{dh}\binom{\varphi}{\psi} = \binom{0.1}{-1.0} \nabla_{\varphi\psi} E.$$

Here $E(\varphi, \psi; h) = (\psi - h\omega)/2$. Then along the real solution (characteristics) of the Crocco boundary problem performed extremum condition

$$S(1, \varphi) = \int_0^1 (\psi - h\omega) dh \to \inf \ \geq \ 0 \tag{9}$$

where $\omega := \log(a/\varphi)$.

Otherwise, the following statement is faithful

Theorem 1. *The inequality $dS \leq \delta S$ holds good where d is the change of S along the path of real solutions and δ is the change in any virtual (compatible with limiting conditions) decision.*

Corollary 1. Considering equation (8) one can put the condition (9) into

$$\int_0^1 \omega(h) dh \to \inf . \tag{10}$$

But, $0 < \omega < \infty$ and, by (10), it is natural to assume that $\omega = \log(a/\varphi)$ is minimally different from 0; φ is minimally different from a. Geometrically, this means that $\varphi(h)$ does not exceed a

$$\int_0^1 \omega(h) dh - a \to \sup \leq \ 0.$$

Let $\varphi \in L_1$ (0,1).This inequality can be weakened to $L_2(0,1) \subset L_1(0,1)$

$$\int_0^1 (\varphi - a)^2 dh = \|\varphi - a\|_2^2 \to \inf \geq 0.$$

Remark. Let

$$\int_0^1 \psi^2 \, dh = \frac{1}{4}, \qquad \psi := \frac{d\varphi}{dh}$$

and let the condition (10) holds good..

Then the following statement is faithful.

Theorem 2. *With boundary value ψ (or norm $\|\psi\|$) momentum reaches a minimum. Conjugate formulation: if momentum is limited,* $\|\psi\| \to \max$.

This is a paraphrase of principle of Duhem.

Variation formulation (9) of the Crocco boundary problem (1) is motivated by the weakening of the solution topology. Indeed, in (9) φ is 2-diffeomorphism, $\varphi \in C^2(0,1)$. For the variation formulation (9) it is excessive demand that $\varphi(h)$ would be 2-diffeomorphism; enough: $\varphi \in W_2^{(1)}(0,1)$. Then $d\varphi/dh \in L_2(0,1)$. In view of the Cauchy inequality $(L_2(0,1) \subset L_1(0,1))$ and moreover $d\varphi/dh \in L_1(0,1)$. Hence, the distribution of the $\varphi(h)$ is absolutely continuous on the interval (0,1), the $C^{(2)}(0,1) \subset C_A(0,1)$ and the feasible solutions set (topologic solutions) is extended.

4. The isoperimetric problem and evaluate $a = \varphi(0)$

Let us assume that instead of (10) the weaker condition holds

$$\int_0^1 h^m(\varphi - a)\,dh \to \inf \geq 0, \qquad \int_0^1 (d\varphi/dh^2)\,dh = 1/4$$

or the Lagrangian (λ is Lagrange multiplier) reaches a minimum

$$Z(\varphi, 1) = \int_0^1 \left(\frac{d\varphi}{dh^2} + 2\lambda\, h^m(\varphi - a)\right) dh \tag{11}$$

and let us run boundary conditions (1). Then $\varphi(h) = a(1 - h^{n+2})$ and $a = a(m) = \sqrt{2m+3}/(2m+4), a(1) = 0.3726, a(2) = 0.3307$. Otherwise $1 < m < 2$. It is convenient to denote $m + 2 := n$. Let $m = 2$ and $n = 4$. Then $a = 0.3307$ (approximation error ~ 0.4%).

Now refine the estimate for the parameter $m = n - 2$.

$$\frac{\varphi}{a} = 1 - h^n, \;\; h = (1 - e^{-\omega})^{\frac{1}{n}}.$$

Let us apply the identity (4) then

$$\frac{1}{4} = \int_0^\infty (1 - e^{-\omega})^{1/n}\left(1 - (1 - e^{-\omega})^{1/n}\right) d\omega = \int_0^1 \frac{z^{1/n}\left(1 - z^{1/n}\right)}{1 - z}\,dz$$
$$= n \int_0^1 \frac{t^{n(1-t)}}{1 - t^n}\,dt.$$

For natural values of n is this integral is easily calculated. For instance, if potentially functions take $n = 4$, it turns out $1/4 = n(2\log 2 + \pi - 4)/8 \Rightarrow n = 3.33203753$. Numerical integration leads to a value of $n = 3.963$. Then $a = \sqrt{2n-1}/2n = 0.33203753$ and the error does not exceed 0.007%.

5. Conclusion

(i) The approximate solution of the boundary problem (1) is expressed in the form:

$$\varphi(h) = a(1 - h^\infty).$$

The constants selection can increase the calculations error of $a = \varphi(0)$ to a percent hundredths.

(ii) The inequality $dS \leq \delta S$, where d is the functional actions S change along the path of real solutions, δ is change in any virtual (compatible with limiting conditions) decision, holds.

(iii) If with a limited value ψ (or norm $||\psi||$) the momentum reaches a minimum then the conjugate formulation is:: if the momentum is limited,then $||\psi|| \to$ max.

References

[1] V.P. Varin. *Flat expansions of solutions and their applications*. Keldysh Institute preprints, Moscow, Vol. 23, 2014.

[2] V.P. Varin. *A solution of the Blasius problem*. Keldysh Institute preprints, Moscow, Vol. 40, 2013.

[3] V.P. Varin. *Flat expansions of solutions to ODEs at singularities*. Keldysh Institute preprints, Moscow, Vol. 64, 2010.

In situ study of micromechanics of smart composite laminates

Andres Punning[1], Urmas Johanson[2], Alvo Aabloo[3]

IMS Lab, Institute of Technology, University of Tartu
Tartu, Estonia
[1]andres.punning@ut.ee, [2]urmas.johanson@ut.ee [3]alvo.aabloo@ut.ee

Abstract. We have developed a methodology to characterize the factual bending of materials of sub-millimeter thickness. Applying the digital image correlation method to thin smart composite laminates, deformed under scanning electron microscope, in situ, reveals the actual bending strain, as well as the precise layer-by-layer strain distribution in the axial and thickness directions. The technique is exemplified with a particular type of electroactive polymers – conducting polymer actuator.

Keywords: *cantilever beam, strain, bending strain, thickness strain, digital image correlation, DIC, scanning electron microscope, SEM, electroactive polymer.*

1. Introduction

During the last few decades, new polymeric transducer materials have been developed for conversation the electrical energy to the mechanical energy [1, 2]. These materials belong to the larger group of electroactive polymers (EAP). One challenging sub-group of the EAP-s is the class of ionic electroactive polymers (IEAP). The electromechanical activeness of the IEAP materials is caused by the electrically induced movement of ions and solvent in the porous polymer structure. A typical IEAP actuator has a trilayer structure, where two sides of a ions-containing porous polymer structure are covered with electronic conductive electrodes. Connecting the electrodes to the electrical power source makes typically this material bending. Such actuators have many advantages comparing to the traditional electromechanical transducers, as they are lightweight and noiseless, have quite simple structure, and require low working voltage of 1–5 Volts.

1.1. Electronic conducting polymer actuators

One interesting subgroup of IEAP-s is the class of electronic conducting polymer (ECP) based actuators. In this case the electrode layers are composed of some organic ECP, e.g. Polypyrrole (PPy) or poly (3,4-ethylenedioxythiophene) (PEDOT) [3]. After synthesis, such conductive polymeric electrode layer comprises positively charged polymer chains together with anions, compensating this charge. The ECP electrodes have dense structure. During reduction (polymer chains lose charge), then anions have to migrate out of the electrode layer. If the anions are too big, or the polymer structure is too tight, then the cations have to enter to the electrode layer from the porous membrane. During oxidation (polymer chains obtain charge), additional amount of anions is incorporated to electrode layer. During the actuation cations and anions move to the direction of oppositely charged electrodes. Ion incorporation to the electrode layer causes its expansion. The small inequal expansion of the opposite electrodes leads to easily perceivable bending of the whole actuator. If this system is kept in charged state for a prolonged time, the ion pairs start to leave the expanded electrodes causes the so-called back-relaxation of the actuator.

1.2. Traditional strain measurement

The most widely used measure for characterizing bending actuators - the strain of an actuator in a cantilever configuration - is actually the difference of strains of the opposite external surfaces of the trilayer laminate. This parameter serves for two purposes, namely, a) describing the extent of bending of a curved actuator with a single number; and b) enabling formulating the relation between strain and stress. In fact, it is adopted from the classical mechanics of cantilever beam, developed by Galilei, Bernoulli, Euler and many of their followers [4]. A traditional cantilever beam is a simple bar-like structural detail whose primary function is to support transverse loading and carry it to the supports. However, the nature of bending of a cantilever in the classical mechanics and an IEAP actuator are totally different. The function of a structural beam is resisting the transverse external loads through its bending action, while the changes in the shape of bending IEAP actuators are caused by the changes in their internal structures.

In order to adopt the bending behavior of the IEAP actuators to the classical mechanics, several simplistic assumptions have been embraced. The most commonly applied postulates are: a) the form of the bent actuator is an exact circular arc; b) strain at any cross-section of the actuator is symmetric about the centroid of the cantilever; c) generated stresses in the actuator are caused solely by the elongation or contraction of the two electrode layers; d) the thickness change of the whole beam is neglible [5, 6]. Naturally, the mechanical properties of the IEAP material are expected being homogeneous over the whole sample.

The magnitude of the bending strain of the IEAP actuators is in the range of up to 2% only. Due to their sub-millimeter thickness, it is practically impossible to measure this value directly. Instead, it is commonly deducted from the macroscopic measurements. The widely used strain difference measurement geometry is depicted in Fig. 1. Owing to the expansion and contraction of the two opposite electrodes, the actuator segment $A-B$ with a length l bends, forming an arc $A-F$ (of radius R and of an arc length L). The displacement δ is commonly measured with a laser displacement meter, guided in a direction perpendicular to the initial straight actuator at the distance l from the fixed input contacts, located at A.

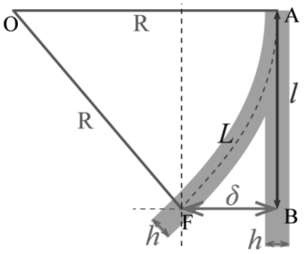

Fig.1. Strain measurement geometry.

It is easy to show [7], that the strain difference ε of the bending laminate (difference of strains of the opposite external surfaces) is expressed through the displacement δ and thickness h of the laminate as

$$\varepsilon = \frac{2\delta h}{l^2 + \delta^2}. \tag{1}$$

This equation, however, is based purely on geometry and stands regardless of the position of the neutral layer. Therefore, the obtained strain difference ε shows the comparison of the strains of the outer layers, but does not tell anything about their actual values, nor about the position of the neutral layer. In fact, similar strain difference can be yielded by an unlimited number of combinations of the two unequal strains, even when both outer layers become longer or both become shorter.

2. Experimental

In this study, the commercial 0.11 mm thick poly(vinylidene difluoride) (PVdF) membranes (Immobilon-P, Millipore, according to product specification: hydrophilic, porosity 70%, pore size 100 nm) was covered chemically and later electrochemically with PPy as described by Temmer et al. [3]. For the electrolyte and solvent, the Ionic Liquid (IL) 1-Ethyl-3-methylimidazolium bis(trifluoromethylsulfonyl)imide (EMIMTFSI) was used. The scanning electron microscope (SEM) micrograph of the cross-section of the actuator is presented in Fig. 2A. As seen, thickness of the the electrodes of the nearly 150 thick ECP actuator is under 10 µm only.

In order to determine the factual strains in the IEAP actuators, we studied the samples under SEM in situ, and compared the resulting micrographs. The experiments were conducted using a Hitachi TM3000 tabletop SEM equipped with electrical terminals in the investigation chamber. The experiments were conducted under the charge reduction regime, where at higher chamber pressures the gas molecules eliminate the extra charge generated by the electron beam. This mode allows imaging non-conducting objects without charging effects. The accelerating voltage was 15 kV, while one input terminal of the samples was connected directly to the chassis of the investigation chamber. As a result, we have not noticed any special actuator behaviour that could have been caused by the vacuum environment, or the high voltage electron beam.

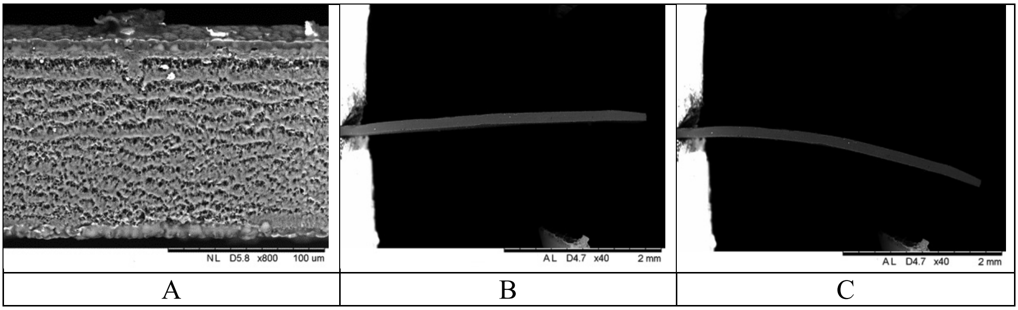

A B C

Fig. 2. IEAP cross-section (A); IEAP in initial state (B); IEAP with voltage applied (C).

2.1. Digital image correlation

As a non-interferometric optical technique, the DIC method is commonly used as a tool for the surface deformation measurement in the field of experimental solid mechanics [8]. It provides a direct access to full-field displacements and strains by comparing the digital images of the specimen surface in the un-deformed and deformed states respectively.

For DIC, we used the MATLAB package 'Improved Digital Image Correlation (DIC)' [9]. but for the IEAP actuators we interpreted the numerical results of the displacement field in a different manner. The procedure starts with the definition of a rectangular uniform grid within the limits of the image of the undeformed actuator, shown in Fig. 2A. The grid is positioned exactly parallel to the outer surfaces of the object of research, so it divides the defined portion of the laminate to layers of equal thickness and length. DIC tracks the positions of the same physical points shown in an undeformed image and a deformed image, as shown in Fig. 2B. The acquired coordinates enable the precise comparison of any distances between the grid points in the images captured before and after deformation.

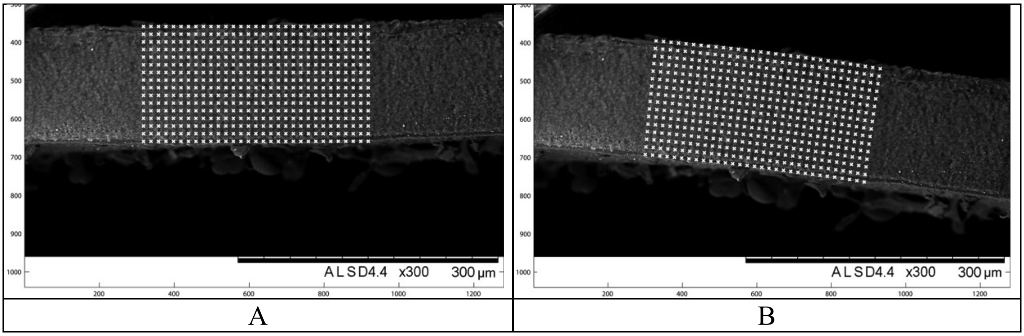

A

B

Fig. 3. Grids, defined in the image of an undeformed actuator (A), and found by DIC in the image of the deformed actuator (B).

With sufficiently small grid step, the length of the polyline gives a good approximation to the length of the layer. The difference of the strains of the outer layers gives the bending strain ε of the laminate. Comparison of the lengths and averaged thicknesses of each individual layer in the bending state and in the initial state leads to the two arrays: the layer-by-layer axial strain and layer-by-layer thickness strain.

3. Results

3.1. Back-relaxation of an actuator

As described above, the conducting polymer actuators exhibit the slow back-relaxation effect. In vacuum chamber, in the absence of humidity, this process is extremely slow, lasting tens of minutes. Scanning of the region of an IEAP sample takes only about ten seconds, therefore recording the SEM micrographs of a very slowly moving actuator is justified.

The diagrams given in Fig. 4. depict the layer-by-layer axial strains and thickness strains of a back-relaxing actuator at two time points: – 60 seconds and 500 seconds after the 1.4 V input voltage was applied. In the following four diagrams, the thickness of the IEAP material is normalized to unity, and the origin of the horizontal axis is set at the centroid of the beam, so initially (before bending) the outer layers are located at positions –0.5 and +0.5. Fig. 4A shows that initially, at the 60 seconds the actuator bends axially symmetrically with respect to the centroid. During back-relaxation the convex side of the laminate becomes shorter, while the concave side remains unchanged. In this process, the neutral layer migrates towards the convex side of the bending beam, eventually surpassing the location at the quarter of the thickness of the laminate. Fig. 4B shows that the thickness of the laminate increases gradually, while the thickening of the layers at the concave side is about twice more intensive. During the back-relaxation, the layers at the concave side of the laminate thicken even more. Although the thickness strains of the layers at the concave side reach up to 5%, the total thickness strain of the whole IEAP laminate is 2.7% and 2.9% at the time points of 60 and 500 seconds respectively.

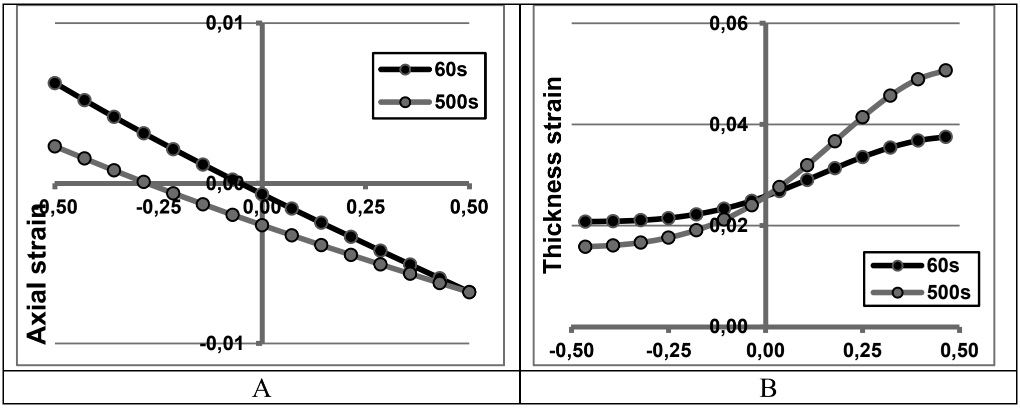

A | B

Fig. 4. Layer-by-layer axial strains (A) and thickness strains (B) of the actuator at the two different time points.

3.2. Second area moment of inertia

For IEAP actuators, the bending moment can be used as a measure of the internal forces that produce a bending displacement [1]. The relevant requisite of the bending moment, depending on the position of the neutral layer, is the area moment of inertia (second moment of area) of the beam. As explained in Section 1.2, the traditional approach of the IEAP actuators assumes that the neutral layer N of a bending IEAP actuator always coincides with the centroid C of the beam (see Fig. 5A) and neglects its thickness change.

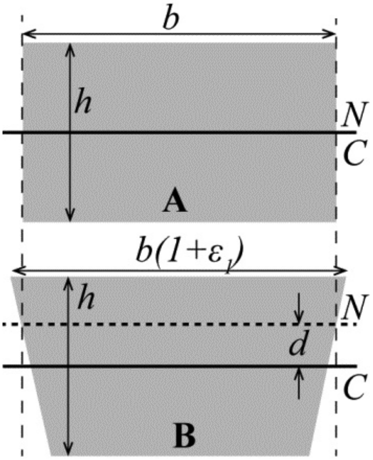

Fig. 5. Dimensions for finding the area moment of inertia.

The area moment of inertia (second moment of area) of the IEAP actuators is therefore commonly calculated according to the equation

$$I_A = \frac{bh^3}{12}, \tag{2}$$

where b and h are the width and thickness of the actuator, respectively, see Fig. 5A.

In fact, the expansion and contraction of the beam occurs in both directions, therefore the cross-section of the laminate transforms to a trapezoid, depicted in Fig. 5B, while during back-relaxation the neutral layer N migrates to the distance d (normalized to the thickness h) from the centroid C. Dividing this shape with the neutral layer into two trapezoids (and neglecting the thickness strain of the beam), its second area moment is expressed as

$$I_B = \frac{b(1+\varepsilon_L)h^3(0.5-d)^3}{3} + \frac{bh^3(0.5+d)^3}{3}, \tag{3}$$

where ε_L is the absolute strain of the convex surface of the beam.

The error, caused by the inappropriate approach to the neutral layer position, is given by the relation

$$\frac{I_B}{I_A} = \varepsilon_L(-4d^3 + 6d^2 - 3d + 0.5) + 12d^2 + 1. \tag{4}$$

With applicable ε_L and d values ($\varepsilon_L < 1\%$ and $d = 0..0.5$), this error lies roughly in the range between 1 and 4. For example, for the actuator at 500 seconds time point (see Section 3.1) the $\varepsilon_L = 0.0025$ and $d = 0.3$. With such values, the $I_B/I_A = 2.08$. It turns out, that he actual second area moment is twice bigger than that, calculated according to the equation (2).

4. Conclusions

We have developed a technique for determining the factual deformations and strains of thin (cantilever) beams under SEM in situ. The DIC technique reveals the layer-by-layer strain distribution in a sub-millimeter thick beam in axial as well as in the thickness direction. In this study we show that simplifications, adopted in the simplistic modelling of ECP and IEAP actuators, may occasionally be inappropriate.

Acknowledgments

This work is partially supported by the Institutional Research Funding project IUT20-24 from Estonian Research Council. The authors express their gratitude to Mr. Rauno Temmer for fabricating the samples of the ECP actuators.

References

[1] Y. Bar-Cohen. *Electroactive Polymer (EAP) actuators as Artificial Muscles: Reality, Potential, and Challenges.* SPIE Press, 2004.

[2] F. Carpi and E. Smela. *Biomedical Applications of Electroactive Polymer Actuators.* John Wiley & Sons, 2009.

[3] R. Temmer, A. Maziz, C. Plesse et al. In search of better electroactive polymer actuator materials: PPy versus PEDOT versus PEDOT–PPy composites. *Smart Materials & Structures.* Vol. 22, No. 10, 2013, 104006.

[4] S. Timoshenko. *History of Strength of Materials: With a Brief Account of the History of Theory of Elasticity and Theory of Structures*. Dover Publications, 1983.

[5] G. Alici and N. Huynh. Predicting force output of trilayer polymer actuators. *Sensors and Actuators, A-Physical,* Vol. 132, No. 2, 2006, pp. 616–625.

[6] K. Mukai, K. Asaka, T. Sugino, K. Mukai and H. Randriamahazaka. High performance fully plastic actuator based on ionic-liquid-based bucky gel. *Electrochimica Acta* Vol. 53, No. 17, 2008, pp 5555–5562.

[7] A. Punning, V. Vunder, I. Must, U. Johanson, G. Anbarjafari and A. Aabloo. In situ scanning electron microscope study of strains of ionic electroactive polymer actuators. *Journal of Intelligent Material System and Structures,* 2015. (in print).

[8] F. Hild and S. Roux. Digital Image Correlation: from Displacement Measurement to Identification of Elastic Properties – a Review. *Strain,* No. 42, 2006, pp. 69–80.

[9] E. Jones. Improved Digital Image Correlation (DIC), Available at MATLAB Central File Exchange. Available at: http://www.mathworks.com/matlabcentral/fileexchange/43073-improved-digital-image-correlation--dic- (accessed 10. November 2013), 2013.

Application of spherical harmonics to description of non-spherical particles

Urtė Radvilaitė[1], Rimantas Kačianauskas[2], Dainius Rusakevičius[3]

Department of Strength of Materials and Engineering Mechanics,
Vilnius Gediminas Technical University,
Vilnius, Lithuania
[1]urte.radvilaite@vgtu.lt; [2]rimantas.kacianauskas@vgtu.lt; [3]dainius.rusakevicius@vgtu.lt

Abstract. The problem of particle shape description by applying spherical harmonics is considered in the framework of the Discrete Element Method (DEM). Two typical symmetric non-spherical particle shapes are investigated for modelling and verification purposes. Rotational ellipsoidal particle presents the sample of the smooth non-spherical axi-symmetric particle shapes, while smooth cube is an ideal particle shape with known characteristics presenting huge class of sphero-polyhedrons. The paper addresses the original optimised semi-analytical modelling technique minimizing the order of spherical harmonic expression while maintaining sufficient accuracy. The variation of several criteria (surface area, volume and etc.) against approximation order parameters is illustrated.

Keywords: *discrete element method, particle shape, spherical harmonics, smooth cube, ellipsoid.*

1. Introduction

Discrete element method (DEM) introduced by Cundall and Strack presents the Lagrangian type modelling technique which is most widely used to study the behaviour of particulate materials. Developments covering conceptual DEM issues related to the particle shape and different simulation aspects are reviewed in [1].

Modeling of the contact between two arbitrary shaped particles is rather difficult task. Usually the particles are approximated by spheres, and the well-known Hertz theory is widely used in DEM applications to model the inter-particle contact. However, the particles of real granular materials are often of irregular shapes. The simulation of such materials by spherical particles does not always yield the reliable results, since many effects may be missed.

There are suggested various models which are suitable for approximation of real non-spherical particles in DEM, but most of them, including multi-spheres and polyhedral shapes, are of semi-discrete character and they have inherent drawbacks. Until now there is a lack for a universal modelling tool getting an analytical expression of a shape. Such a model could control the accuracy of the results in systematic fashion and thus retaining advantages of spherical contact calculation.

In this paper spherical harmonics as semi-analytical hierarchical method are introduced. Spherical harmonics is widely used and well-understood tool of applied mathematics, physics and engineering. The application samples are encountered in weather and climate modelling, in the representation of gravitational, topographic, and magnetic data in geophysics, in the numerical solution of certain partial differential equations [2], they occur as well in a great variety of different physical problems such as electromagnetism, gravity, mechanics or hydrodynamics [3]. Successful 3D applications of sophisticated spherical harmonics comprise lunar regolith or sand particles [4, 5].

In the next section the spherical harmonics expansion and its formulation are given. The suggested model is applied to ellipsoidal and smooth cube shaped particle and the results are given in the third section.

2. Spherical harmonics expansion

Spherical harmonics form an orthonormal base and arbitrary continuous function $F(\theta,\varphi)$ given in spherical coordinates can be expanded into spherical harmonics. In applications spherical harmonic expansion of a function is limited to a finite number N and is given by

$$F(\theta,\varphi)=\sum_{l=0}^{N}\sum_{m=0}^{l}a_l^m Y_l^m(\theta,\varphi) \tag{1}$$

where $Y_l^m(\theta,\varphi)$ is spherical harmonics of degree $l\in N_0$ and order m $(0\le|m|\le l)$ and a_l^m is their coefficient [6].

Spherical harmonics formal definition is

$$Y_l^m(\theta,\varphi)=N_l^{|m|}P_l^{|m|}(\cos\theta)e^{im\varphi} \tag{2}$$

where $N_l^{|m|}$ is a normalization constant and $P_l^{|m|}(\cos\theta)$ – associated Legendre polynomials [7].

Because usually only real valued functions are used in applications, it is useful to have a real spherical harmonics, which are real or imaginary parts of complex function when $m>0$ or $m<0$ and original function itself when $m=0$. This definition is given by

$$Y_l^m=\begin{cases}\sqrt{2}N_l^m\cos(m\varphi)\,P_l^m(\cos\theta) & if\ m>0\\ N_l^0P_l^0(\cos\theta) & if\ m=0\\ \sqrt{2}N_l^{|m|}\sin(|m|\varphi)\,P_l^{|m|}(\cos\theta) & if\ m<0\end{cases} \tag{3}$$

Using spherical harmonic expansion (1) requires two basic steps: first – generating of spherical harmonics and second – the calculation of expansion coefficients. The coefficients are calculated using least square method which minimizes the error between the exact function values and those given by spherical harmonics expansion

$$\min_a\sum_{i=1}^{n}\left(r_i-F_i(a)\right)^2, \tag{4}$$

where $r_i=r(\theta_i,\varphi_i)$ are coordinates of the given points,

$$F_i(a)=\sum_{j=1}^{k}y_{i,j}a_j,\ i=1,\dots,n$$

is spherical harmonics expansion at the point (θ_i,φ_i), a_j is unknown expansion coefficients, $y_j=y_l^m(\theta,\varphi)$ – spherical harmonics transformed into one-dimensional array, where element index is given by $j=(l+1)l+m$.

3. Modelling approach

Modelling approach considered hereafter is aimed to illustrate non-regular shaped particle. The particle presents three-dimensional body surface which is described by discrete set of points. This imaginary body could be reconstructed by a quasi-surface described in spherical coordinates. The simplified case of symmetric body is considered. This description means that each arbitrary point on the surface will be defined by the variable radial length R and two spherical angles θ and φ.

Several basic assumptions are employed for characterization of particle shape. Skeleton of the particle surface presented in polar form is convex, or star-shaped, i.e. each generatrix ray is uniquely related to the point on the continuous surface. Axial symmetry and/or rotational symmetry is assumed to be imposed.

Particle surface is assumed to be continuous random non-smooth function uniquely defined by a discrete set of random as well as determined parameters. Consequently, the surface, or skeleton geometry is generated numerically according to specified rules by applying fixed or randomly defined values of the model parameters.

We assume that quasi-surface is initially generated in deterministic manner. Discrete model of the particle is presented by a set of N reference points located on the particle surface while particle surface is presented by a set of triangles. Definition of geometry is assumed to be hierarchical, and series of models may be developed by varying of them. It means that accuracy of geometry description could be hierarchically improved by increasing number of specified points.

4. Numerical results

For testing of the spherical harmonics technique two sample particles of the specified geometry have been generated numerically. Rotational quasi-ellipsoidal particle presents sample of the smooth non-spherical axi-symmetric particle shapes, while smooth cube is ideal particle shape with known characteristics presenting huge class of sphero-polyhedrons. The suggested technique is based on numerical data processing. The method reads the input data – set of surface points – and generates the spherical harmonics with their coefficients.

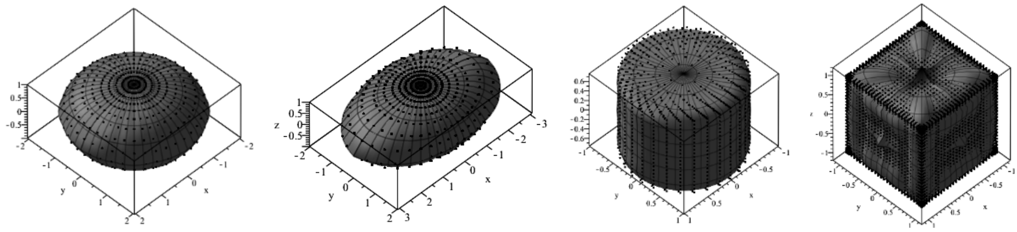

(a) (b) (c) (d)

Fig. 1. Spherical harmonics model of: (a) a disk; b) an ellipsoid; (c) a cylinder; (d) a cube.

In Fig. 1 models of several differently shaped particles are given. The order of spherical harmonics expansion used in those models is $N = 3$, i.e. the total number of spherical harmonics used in model is 16.

Spherical harmonics expansion applied to any particle is

$$\begin{aligned}F(\theta,\varphi) = {} & \alpha_1 \frac{1}{2\sqrt{\pi}} + \alpha_2 \frac{\sqrt{3}}{2\sqrt{\pi}} \sin\theta \sin\varphi + \alpha_3 \frac{\sqrt{3}}{2\sqrt{\pi}} \cos\theta + \alpha_4 \frac{\sqrt{3}}{2\sqrt{\pi}} \sin\theta \cos\varphi \\ & + \alpha_5 \frac{\sqrt{15}}{4\sqrt{\pi}} \sin^2\theta \sin 2\varphi + \alpha_6 \frac{\sqrt{15}}{2\sqrt{\pi}} \cos\theta \sin\theta \sin\varphi \\ & + \alpha_7 \frac{\sqrt{5}}{4\sqrt{\pi}} (3\cos^2\theta - 1) + \alpha_8 \frac{\sqrt{15}}{2\sqrt{\pi}} \cos\theta \sin\theta \cos\varphi \\ & + \alpha_9 \frac{\sqrt{15}}{4\sqrt{\pi}} \sin^2\theta \cos 2\varphi + \alpha_{10} \frac{\sqrt{35}}{4\sqrt{2\pi}} \sin^3\theta \sin 3\varphi \\ & + \alpha_{11} \frac{\sqrt{105}}{4\sqrt{\pi}} \cos\theta \sin^2\theta \sin 2\varphi + \alpha_{12} \frac{\sqrt{21}}{4\sqrt{2\pi}} (5\cos^2\theta - 1) \sin\theta \sin\varphi \\ & + \alpha_{13} \frac{\sqrt{7}}{4\sqrt{\pi}} \cos\theta\, (5\cos^2\theta - 3) + \alpha_{14} \frac{\sqrt{21}}{4\sqrt{2\pi}} (5\cos^2\theta - 1) \sin\theta \cos\varphi \\ & + \alpha_{15} \frac{\sqrt{105}}{4\sqrt{\pi}} \cos\theta \sin^2\theta \cos 2\varphi + \alpha_{16} \frac{\sqrt{35}}{4\sqrt{2\pi}} \sin^3\theta \cos 3\varphi \end{aligned} \tag{5}$$

Table 1. The coefficients of spherical harmonics expansion for different particles.

Particles **Coefficients**	**Disk** $(\boldsymbol{a = 2, b = 2, c = 1})$	**Ellipsoid** $(\boldsymbol{a = 3, b = 2, c = 1})$	**Cylinder** $(\boldsymbol{h = 1.5, r = 1})$	**Cube** $(\boldsymbol{a = 2})$
α_1	11.937	11.704	1.3837	50.585
α_2	-3.0667	-3.2667	1.9980	-26.950
α_3	-5.5944	-5.5189	2.0409	-26.256
α_4	-3.0696	-1.1541	1.9943	-26.950
α_5	1.0287	0.55538	-0.80288	9.7819
α_6	1.2268	1.4421	-1.0907	9.9177
α_7	0.31725	0.37836	-1.1815	-0.60375
α_8	1.2371	0.042162	-1.0872	9.9177
α_9	-0.038866	0.072996	-0.072617	-0.30523
α_{10}	0.12479	0.22229	-0.014879	0.54388
α_{11}	0.13559	0.074378	0.31629	-2.1040
α_{12}	0.056502	-0.021092	0.10157	0.23980
α_{13}	0.21873	0.20784	0.16425	0.18793
α_{14}	0.053894	0.26146	0.099595	0.23980
α_{15}	0.16438	0.092113	0.029535	-0.075936
α_{16}	0.12815	0.12236	-0.014740	0.54388

The spherical harmonics for any arbitrarily shaped particle are the same, only expansion coefficients are recalculated. The coefficients for different particle shapes are given in Table 1.

The estimation of the models is made by calculating absolute difference between theoretical and experimental values of geometrical characteristics: surface area, volume and inertia of moment. As shown in Fig. 2, error estimation for cube shaped particle gives more accurate results when used more points.

Also the accuracy of model can be changed by increasing the number of spherical harmonics. The more spherical harmonics are used, the more initial points of model should be used. Additionally, it should be mentioned that using more spherical harmonics increases the calculation time.

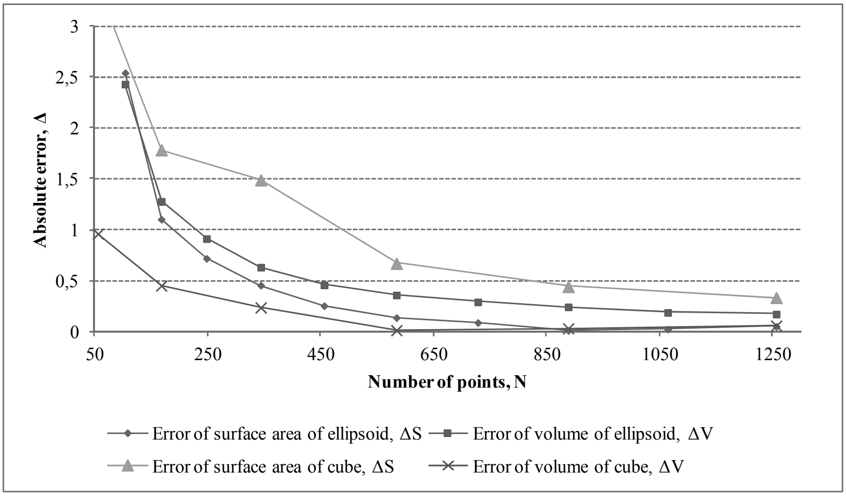

Fig. 2. Error estimation of spherical harmonics model.

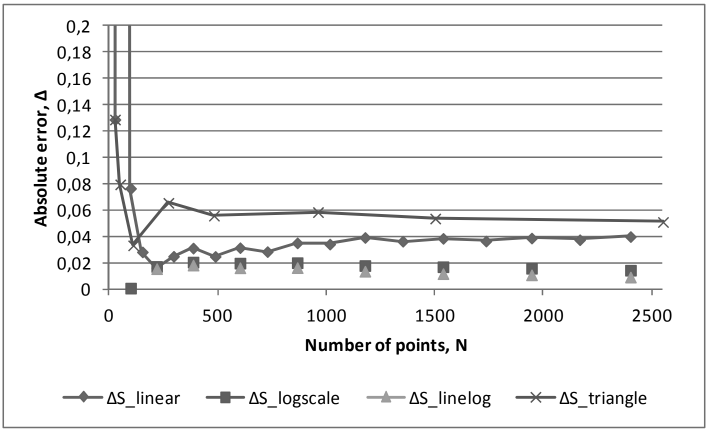

Fig. 3. Error estimation of spherical harmonics model with different mesh.

The accuracy of the spherical harmonics models also depends on the type of mesh used. For a cube particle several types of mesh was analysed. Fig. 3 shows the errors estimation when the used linear mesh, logarithmic scale mesh, combined linear and logarithmic mesh and triangular mesh have been used.

This methodology of surface approximation by spherical harmonics is applied for experimentally given points of maize corn surface [8, 9].

5. Conclusion

The expansion of spherical harmonics have been introduced for generation of particles of arbitrary shape. The discussed technique was applied to particles of known geometry in order to estimate the errors. The results show that there is no need to use a large number of spherical harmonics in order to obtain acceptable results.

References

[1] G. Lu, J.R. Third and C.R. Muller. Discrete element models for non-spherical particle systems: from theoretical developments to applications. *Chemical Engineering Science*, Vol. 127, 2015, pp. 425–465.

[2] V. Rokhlin and M. Tygert. Fast algorithms for spherical harmonic expansions. *SIAM Journal of Scientific Computing*, Vol. 27, No. 6, 2006, pp. 1903–1928.

[3] R.J. Morris, R.J. Najmanovich, A. Kahmaran and J.M. Thornton. Real spherical harmonic expansion coefficients as 3D shape descriptors for protein binding pocket and ligand comparisons. *Bioinformatics*, Vol. 21, No. 10, 2005, pp. 2347–2355.

[4] E.J. Garboczi. Three dimensional shape analysis of JSC-1A simulated lunar regolith particles. *Powder Technology*, Vol. 207, 2011, pp. 96–103.

[5] X. Liu, E.J. Garboczi, M. Grigoriu, Y. Lu, and S.T. Erdogan. Spherical harmonic-based random fields based on real paticle 3D data: Improved numerical algorithm and quantitative comparison to real particles. *Powder Technology*, Vol. 207, 2011, pp. 78–86.

[6] H. Wang, P. Wu, and Z. Wang. An approach for spherical harmonic analysis of non-smooth data. *Computers & Geosciences*, Vol. 32, 2006, pp. 1654–1668.

[7] M.-H. Mousa, R. Chaine, S. Akkouche and E. Galin. Toward an efficient triangle-based spherical harmonics representation of 3D objects. *Computer Aided Geometric Design*, Vol. 25, 2008, pp. 561–575.

[8] C. González-Montellano, Á. Ramírez, E. Gallego, and F. Ayuga. Validation and experimental calibration of 3D discrete element models for the simulation of the discharge flow in silos. *Chemical Engineering Science*, Vol. 66, 2011, pp. 5116–5126.

[9] R. Kačianauskas, Á. Ramírez-Gómez and U. Radvilaitė. Semi-analytical model for non-spherical particles. *Proceedings of the International Conference on Numerical Analysis and Applied Mathematics 2014* (ICNAAM-2014), Rhodes, Greece, 22.–28. September 2014, Melville : AIP Publishing, 2015.

One variant of the multiscale methods for fracture

Larissa Roots

Institute of Structural Mechanics, Bauhaus-University Weimar
Weimar, Germany
larissa.roots@uni-weimar.de

Abstract. The aim of the paper is to gain a better understanding of the phenomena involved with material failure by contributing to the first set of experimentally validated computational methods capable of predicting material failure from the atomistic to the continuum level. This requires the combination of knowledge from different areas, i.e. Computational Mechanics, Computational Material Science. This method bridges three different length scales from micro-scale over meso-scale to macro-scale. Between mechanical characteristics of a solid body at the level of continuous mechanics (Young's modules, Poisson's ratio) and parameters at the molecular level (the molecule size, structure of a crystal lattice) there is the dependence. Therefore, this work is devoted to develop the theoretical framework and its extension to various materials.

Keywords: *Bernoulli's hypothesis, continuous mechanics, molecular dynamics.*

1. Introduction

One major research focus in the Material Science and Engineering Community in the past decade has been to obtain a more fundamental understanding on the phenomenon "material failure". Such an understanding is critical to the design of new materials and Engineering components as well as for the development of more robust and reliable (predictive) numerical methods. To gain a better understanding of material failure, first principle type simulations are required. In many engineering applications, the global response of the system is often governed by the behavior at the smaller length scales. For example, in metallic failure, one of the most common modes of failure is the appearance of shear bands, which are often the progenitors of cracks. Thus subscale behavior must be computed accurately for good predictions of the full scale behavior, so the numerical models must deal with multiple spatial and temporal length scales.

A plethora of methods have been developed in the past decade that aim to resolve the domain where material failure takes place at the atomistic scale. Calculations at the atomistic scale promise to provide more insight into the fundamental mechanics of "materials failure". However, the scales of engineering problems involving macroscopic cracks and shear bands are orders of magnitudes larger than the length and time scales at the atomistic level.

Therefore, methods that bridge these two length and time scales are needed and have been the focus of intense research for many years (see Fig. 1). However, most coupling methods and simulations are focused on models of intact materials (in the absence of cracks), assume low temperatures are (to simplify Molecular Dynamics simulations). The transfer of information through the different length scales for problems involving material failure and finite temperatures remains a very challenging task.

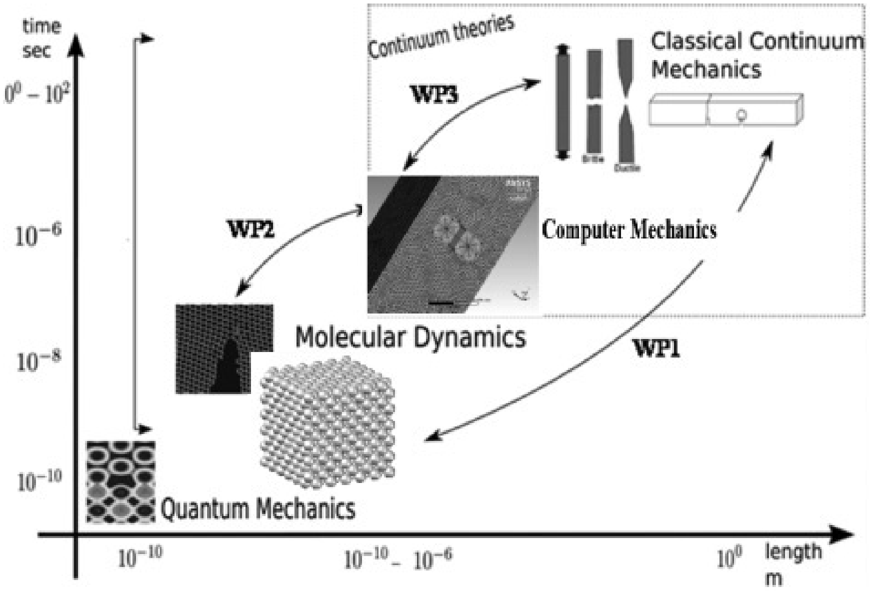

Fig. 1. Overview over different simulation tools and associated length scales and time scales.

Classical fracture mechanics is based on a continuum description of material domains and fracture behavior described in terms of empirical parameters. Continuum mechanics methods such as the finite element method (FEM) and the extended finite element method (XFEM) provide an economical numerical representation of material behavior at length scales in which continuum assumptions apply.

In the classical theory of elasticity (the section of continuous mechanics) it is supposed that movements of a body in comparison with its linear sizes are small, and relative lengthenings and corners of shift are small in comparison with unit. The small movements and linear dependence between tension and deformations allow to apply the principle of independence of action of forces. It gives the possibility to count result of impact on a body of system of forces as addition of results of influence of each force separately. Saint-Venant's principle in continuous mechanics is of great importance: “... the difference between the effects of two different but statically equivalent loads becomes very small at sufficiently large distances from load.” On the basis of Saint-Venant’s principle the loading distributed by small part of a surface of a body can be replaced with the concentrated force. The hypothesis of flat sections (Bernoulli’s hypothesis) plays not less important role in the theory of elasticity as in the section of continuous mechanics: before and after deformation, the cross sections of a beam is flat and perpendicular to axes of a beam. Besides in the theory of elasticity full elasticity is ability of solid bodies to restore completely an initial form and volume after elimination of external physical impacts. Ideally elastic body is supposed isotropic and homogeneous. Ideally elastic body is supposed continuous, i.e. continuous before deformation, elastic body remains continuous and after deformation. Any volume of a body, includes microvolumes, has no emptiness and gaps. It gives the possibility to consider deformations and movements of points of a body as continuous functions of coordinates. Thereby the atomistic structure of body and motion of the molecules in a body isn't taken into account in continuous mechanics.

Real bodies with this or that accuracy can be considered quite elastic, isotropic, homogeneous and continuous. The solid body is one of four aggregate states of substance, with a stable form and with the characteristic thermal movement of the atoms making small fluctuations about balance position. Solid bodies can have a crystalline and amorphous structure. Within this article we will be limited to consideration by a crystalline structure of solid bodies. The crystal lattice can be thought of as an array of 'small boxes' infinitely repeating in all three spatial directions. Such a unit cell is the smallest unit of volume that contains all of the structural and symmetry information to build-up the macroscopic structure of the lattice by translation. Natural form of crystals – regular polyhedrons. Atoms and molecules in a solid body are densely packed together. So it keeps the mutual situation relatively each other and it keeps intermolecular interactions.

Molecular dynamics (MD) is a powerful tool for modelling of fracture in material with various internal structure and defects distribution. Methods of molecular dynamics are based on Lennard-Jones type pairwise potentials of interaction. The concept of pairwise potential implies that interaction of two particles depends only on their relative positioning and does not depend on position of any other particles. All potentials of Lennard-Jones type describe interaction for which pushing away at small distances and attracting at greater distances are characteristic. In the MD the big ensemble of the particles modeling atoms or molecules is considered. The particles interact with each other and besides can be subjected to external influence. In overwhelming majority of cases particles are considered as point masses. For all particles the equations of motion are formulated. The received system of the equations is solved by numerical methods. Rapid development of computer facilities gives possibility to solve such problems for the increasing number of particles. However, now it is impossible to model a macroscopic body, comparing each atom a point mass. Literature [1–5] was used for introduction.

2. Deformation of face-centered cubic crystal system

Let's consider the face-centered cubic crystal system with side $A = 2\sqrt{2}Rn$, where R – atomic radius of material, n- number of atoms on the side (Fig. 2). The face-centered cubic system is closely related to the hexagonal close packed system, and the two systems differ only in the relative placements of their hexagonal layers. The [111] plane of a face-centered cubic system is a hexagonal grid.

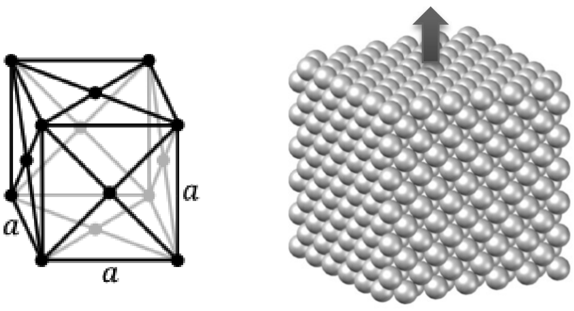

Fig. 2. Face-centered cubic crystal system.

Let’s in the tension test the face-centered cubic crystal system is subjected to a continually increasing uniaxial tensile force while simultaneous observations are made of the elongation of the specimen. The parameters, which are used to describe the stress-strain curve of a cubic, are the tensile strength, yield strength or yield point, percent elongation, and reduction of area. The first two are strength parameters; the last two indicate ductility (Pic.4).

Hypothesis of flat sections (Ja. Bernoulli's hypothesis) has to be carried out and at the molecular level in the cubic. It will force atoms to move in certain manner (Fig. 3).

Let's denote $L = H = 2\sqrt{2}\,Rn$, where L – length and H – width of cubic before deformation.

After deformation we will have

$$H_1 = 2(1+x)Rn,$$

$$L_1 = 2(\sqrt{4-(1+x)^2} + \sqrt{4-(1+x)^2})Rn,$$

where $x \in \left[0, \sqrt{2}-1\right]$.

After deformation 2 parallel layers are formed of each molecular layer. This process will end when $H_1 = 2Rn, x = 0$.

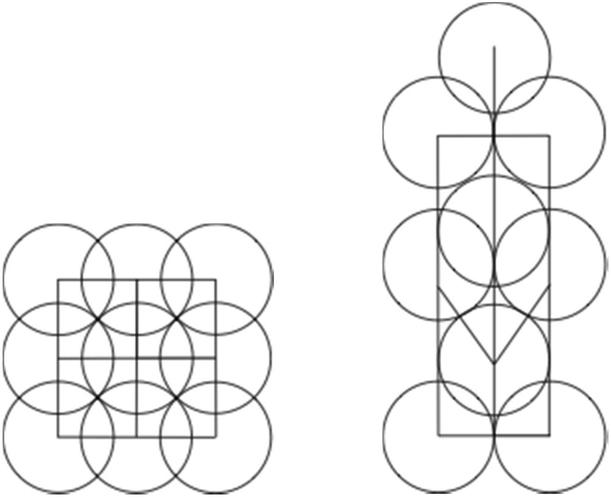

Fig. 3. Face-centered cubic before and after deformation.

In turn,

$$\varepsilon_L = \frac{\Delta L}{L} = \frac{\sqrt{4-(1+x)^2} + \sqrt{4-2(1+x)^2}}{\sqrt{2}} - 1$$

(*i.e.*, [change in length] as a fraction or percentage of total length),

$$\varepsilon_H = \frac{\Delta H}{H} = 1 - \frac{1+x}{\sqrt{2}}.$$

For an elastic zone before a point 1 on the stress-strain curve (Fig. 4) Poisson's ratio is constant

$$\gamma = \frac{\varepsilon_H}{\varepsilon_L} = const.$$

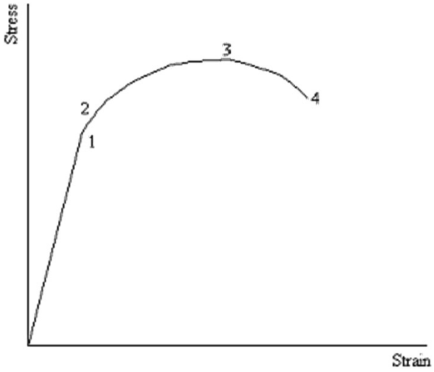

Fig. 4. Stress-strain curve.

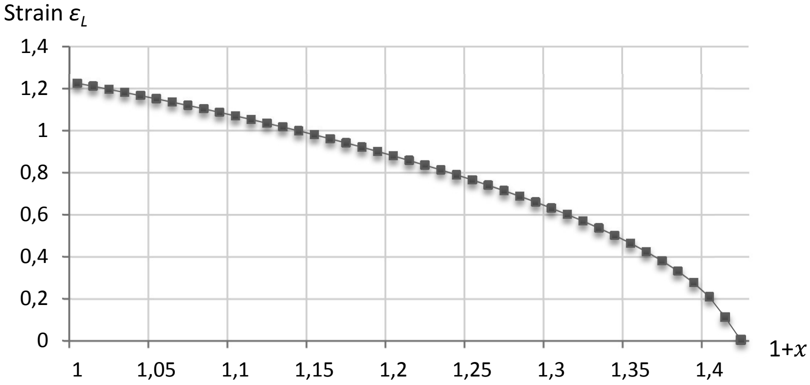

Fig. 5. Strain ε_L vrs $1 + x$.

In a plastic zone after a point 1 on the stress-strain curve ratio $\varepsilon_H/\varepsilon_L$ is function from x.

$$\frac{\varepsilon_H}{\varepsilon_L} = f(x).$$

The strain ε_L as function from $1 + x$ is represented in Fig. 5. When $x = 0$, it corresponds to the maximum $\varepsilon_{Lmax} = \sqrt{3}/\sqrt{2}$. It corresponds to a point 3 on the stress-strain curve (Fig. 4).

3. Concluding remarks

Hypothesis of flat sections (Bernoulli's hypothesis) has to be carried out and at the molecular level in the cubic. It will force atoms to move in certain manner. For an elastic zone before a point 1 on the stress-strain curve (Fig. 4), strain ε_L is small and each atom fluctuat concerning balance position. In a plastic zone after a point 1 on the stress-strain curve strain ε_L doesn't depend on the atomic radius of material.

When formation of 2 parallel layers from one layer is the complete, we will have necking between points 3 and 4 on the stress-strain curve (Fig. 4) and fracture in point 4. Necking is a mode of tensile deformation where relatively large amounts of strain localize disproportionately in a small region of the material. The resulting prominent decrease in local cross-sectional area provides the basis for the neck.

Acknowledgments

The partial support from the target financed from the Grant MJD433 "Multiscale method for fracture" is gratefully acknowledged.

References

[1] R.W.N. Honeycombe. *The Plastic Deformation of Metals*. Edward Arnold (Publishers) Ltd, 1968.
[2] A.E.H. Love. *A treatise on the mathematical theory of elasticity*. Fourth Edition, New York Dover Publications, 1944.
[3] S. Timoshenko. *Strength of Materials*. New-York, 1930.
[4] P. Budarapu, R. Gracie Shih-Wei Y., X. Zhuang and T. Rabczuk. Efficient Coarse Graining in Multiscale Modeling of Fracture. *Theoretical and Applied Fracture Mechanics*, Vol. 69, 2014, pp. 126–143.
[5] S.-W. Yang, P.R. Budarapu, D.R. Mahapatra, S.P.A. Bordas, G. Zi and T. Rabczuk. A meshless adaptive multiscale method for fracture. *Computational Materials Science*, Vol. 96, 2015, pp. 382–395.

Inverse technique for the glass stiffness characterization

Liene Šable[1], Eduards Skuķis, Guntis Japiņš, Kaspars Kalniņš[2]

Institute of Materials and Structures, Rīga Technical University
Riga, Latvia
[1]lienesable@gmail.com, [2]kaspars.kalnins@sigmanet.lv

Abstract. Current paper presents the application of inverse optimization approach for estimation of stiffness for glass panel specimens. The approach is based on elaborated metamodels of numerical frequency responses and minimisation of variation between physical tests. Present approach highlight several advantages in comparison with conventional mechanical test methods. As example 4-point bending present exposure of testing personnel to hazardous eruption of glass shreds once annealed and tempered specimens reach ultimate stress level. Therefore non-destructive test according to ASTM E756-05 for determination of stiffness from self-frequency responses has been selected as verification reference compared to the inverse approach. For initial optimisation task three design parameters: elastic and shear modulus has been implemented in simulation with commercial FEM code ANSYS. A Latin hypercube design of computer experiments within given domain of interest has been evaluated, where metamodel responses was obtained by partial polynomial approximations. An overall good agreement has been obtained between inverse and standard ASTM E756-05 method. As a future step this method will be extended for glass laminated panels.

Keywords: *annealed glass, tempered glass, Eigen frequencies, NDT.*

1. Introduction

The stiffness of glass is one of the highest compared with others materials characteristics – where Young’s modulus is three times greater than concrete, by magnitude compared to most of polymers and equivalent to aluminium. This is reason why glass is so popular structural material and even considered and utilized for load bearing structures. Transparency, high mechanical strength and relatively medium density are glass properties which are reason for glass frequent applicability [1]. Moreover, it is expected that both annealed and tempered glass share the same Young’s modulus value, and it doesn’t depend on glass edge trimming and finish quality. In comparison to many other crystals, whose properties depend on the direction in which they are measured, glass exhibits amorphous isotropy, i.e., the properties are not dependent on direction [2]. This should encourage design engineers to extensively utilise such material, however due brittleness it`s almost abandoned in design practice for load carrying structures.

For glass using in load bearing structures is necessary high quality glass without mechanical damages and glass stiffness is a parameter which is believed to be depended on glass production/furnishing quality. So far the most test method for glass mechanical material mechanical characterization [3–5] was 4 – point bending test according to EN 1288-3:2001 [5]. However, this test method are relatively expensive and wasted material is in large quantities. As an alternative method for bending test is non-destructive technique, based on vibration tests and extractions of the stiffness by calculation method according to ASTM E1876-01 [6].

2. Reference characterization according to ASTM E1876-01

As a reference for glass dynamic elastic properties evaluation are extracted according to ASTM [7] at ambient temperature. Specimens of materials possess specific mechanical resonant frequencies that are prescribed by stiffness, mass, and geometry of the test specimen, where last two are simple to measure. Therefore if one can determine experimentally self-frequencies, this enable dynamic stiffness determination using the resonant frequency in either the flexural or longitudinal mode of vibration. Moreover the dynamic shear modulus, is found determining torsional resonant vibrations.

Dynamic Young's modulus equation for governing flexure frequency of a rectangular bar are expressed as follows [7]:

$$E = 0.9465\left(\frac{mf_f^2}{b}\right)\left(\frac{L^3}{t^3}\right)T_1 \tag{1}$$

where E – Young's modulus, m – mass of the bar, b – width of the bar, L – length of the bar, t – thickness of the bar, f_f – fundamental resonant frequency of bar in flexure and T_1 – correction factor for finite thickness of bar. Similarly the shear modulus can be determinate:

$$G = \frac{4Lmf_t^2}{bt}\left[\frac{B}{1+A}\right], \tag{2}$$

where G– dynamic shear modulus and f_t – fundamental resonant frequency of bar in torsion. Furthermore A – an empirical correction factor dependent on the width to – thickness ratio of the test specimen. This correction factor has an effect of less than 2% and can be omitted, unless accuracies of better than 2% are desired.

$$A = \frac{\left[0.5062 - 0.8776\left(\frac{b}{t}\right) + 0.3504\left(\frac{b}{t}\right)^2 - 0.0078\left(\frac{b}{t}\right)^3\right]}{\left[12.03\left(\frac{b}{t}\right) + 9.892\left(\frac{b}{t}\right)^2\right]}, \tag{3}$$

$$B = \left[\frac{\frac{b}{t}+\frac{t}{b}}{4\left(\frac{t}{b}\right) - 2.52\left(\frac{t}{b}\right)^2 + 0.21\left(\frac{t}{b}\right)^6}\right]. \tag{4}$$

Finally μ - Poisson's ratio is determinate based on theory of elasticity:

$$\mu = \left(\frac{E}{2G}\right) - 1. \tag{5}$$

The applied standard is limited for substantial approach because of the characteristics allows to be extracted from simple beam responses, and for non-conventional geometrical shapes this calculation is not applicable our should it be considered with caution.

3. Inverse technique

Alternatively elastic modulus determination have been optimized by inverse method. The basic idea of material identification procedure elaborated on vibration tests and indirect optimization methodology. A schematic representation of the inverse method is given in

Fig. 1. For given procedure as first step the parametrical input file in finite element commercial code ANSYS is made. Then design of experiments are sampled within the domain of interest for design parameters E, G and the thickness – t. Furthermore first ten self-frequencies have been obtained in all sampled combinations. These responses are approximated by partial polynomial functions to generate surrogate our metamodels. In parallel vibration experiments (Fig. 2) are carried out with the purpose to determine natural frequencies. An identification of material properties is performed in the final stage minimizing the error functional between experimental and numerical parameters of structural responses [8].

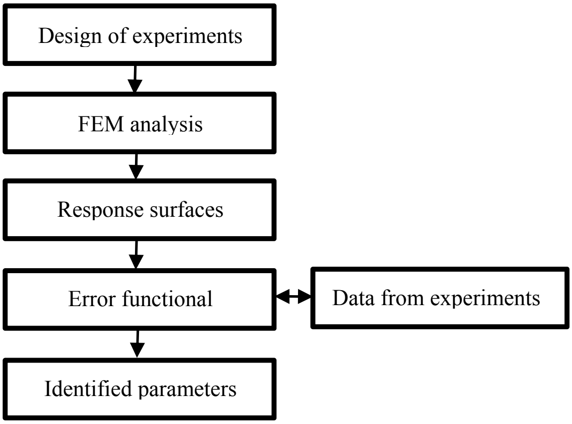

Fig. 1. Inverse procedure.

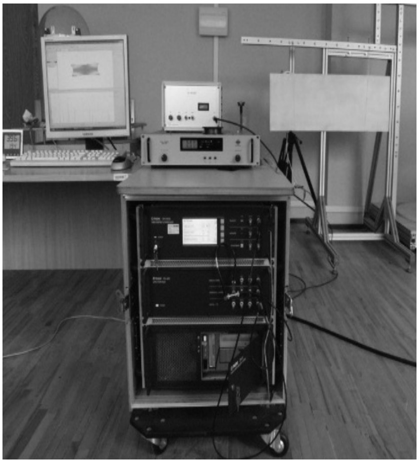

Fig. 2. Test set-up for modal analysis on POLYTECH PSV-400 equipment.

3.1. Experimental investigation

Experimentally elastic modulus determination have been done by non – destructive method – measuring structural responses in full frequency spectrum. Laser vibrometer test equipment PSV-400 was used for this purpose (Fig. 2). The Polytech PSV-400 vibrometer is a laser based measurement tool for non-contact measurements, visualization and analysis of structural vibrations. In modal test an entire surfaces of glass panel can be scanned and probed automatically by applying flexible and interactive measurement grids. Moreover measurements can be made over a wide frequency bandwidth from 0 to 800 Hz. Excitation of the structure has been introduced by software controllable loudspeaker. Structural modal responses has been captured by a laser vibrometer and converted to graphical mode shapes for visual matching with FEM Eigen mode results from commercial code ANSYS [9]. Modal analysis testing glass panel samples size $L = 1100 \pm 1\text{mm}$ long and $b = 360 \pm 1\text{mm}$ wide were cut from a single glass plate with a thickness of 8,10,12 mm (h), edges where grinded and polished.

3.2. Finite element models

All numerical analysis employed commercial software ANSYS and SHELL281 shell finite element. The SHELL281 is most advanced and well-suited for linear, large deformation, and/or large strain nonlinear applications [9]. The element has eight nodes with six degrees of freedom at each node. Furthermore once verified the model could be extended for laminated glass analysis, where viscoelastic plies are incorporated in FE analysis. That type of analysis can determine vibration damping our loss factors, thus identifying some more advanced properties. Graphical correlation with experimental and numerical self-frequency mode shaped are given in Fig. 3.

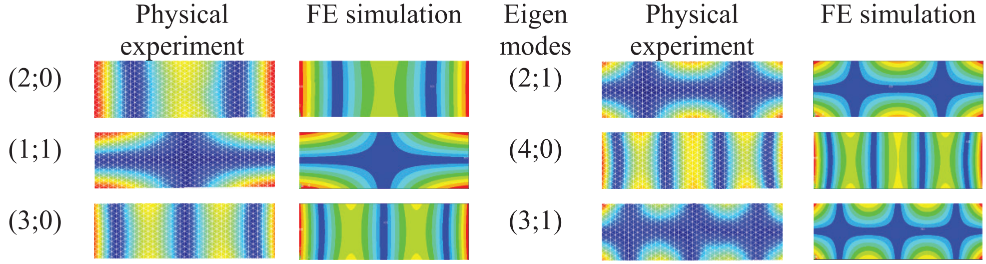

Fig. 3. Experimental and numerical Eigen frequency modes for glass specimens.

3.3. Metamodelling approach

Metamodelling is a set of tools, based on design of experiments, parametrical our non-parametrical approximations of mathematical model of given system. Approximation model should be unsophisticated enough to guarantee instant calculation times at the same time keeping required prediction accuracy. Therefore cross-validation error estimation was set as a criteria for evaluating best mathematical approximation function of each self-frequency.

For design of experiment, three design parameters have been defined in Table 1.

Table. 1. Domain of interest.

Parameters	Unit	Lower bound	Upper bound
Elastic modulus, E	GPa	70	75
Shear modulus, G	GPa	29	33
Thickness, t	mm	7.8	11.9

Design of experiments was made employing Latin Hypercube design with Mean Square Error (MSE) space filling criteria in order to uniformly redistribute the points inside domain of interests. In order to obtain statistically reliable mathematical approximation functions it is necessary to carry out a definite number of numerical experiments. $EdaOpt$ [10] optimisation software was used to create experimental design with 140 experiments and 3 variables. A two dimensional section of 3-dimensional design is shown in Fig. 4. For approximation purposes in-house software $VariReg$ [11] was utilised with ability to approximate experimental data by full or partial polynomials and Kriging. Analysing cross-validation error estimates was concluded that the lowest approximation error was conducted by partial polynomial function based on Adaptive Basis Function Construction approach (ABFC) [11].

The number of Eigen frequencies was determined according to minimum required amount of non-coupled modes. Employing these numerical values, the approximating functions (response surface) for all Eigen frequencies (excluding coupled Eigen frequencies) were obtained. The objective function in the case can be written in the following form:

$$\boldsymbol{\Phi}(X) = \sum_{i=1}^{6} \frac{\left(f_i^{exp} - f_i^{FEM}\right)^2}{\left(f_i^{exp}\right)^2} \longrightarrow \text{min.} \tag{6}$$

Minimizing (1) function, the elastic material constants have been identified. The results have been verified comparing the experimentally measured Eigen frequencies with the numerically obtained using the identified elastic properties. The residuals are calculated the following expression

$$\Delta_{\boldsymbol{i}} = \frac{f_i^{exp} - f_i^{FEM}}{f_i^{exp}} \times 100. \tag{7}$$

4. Results and discussions

For experimental verification three different thicknesses and edge finish concepts has been investigated. Abbreviation used: annealed panels referred as AN and annealed specimens with edges grinded and polished $AN+$. Similarly tempered glass is referred ESG and $ESG+$. Dedicated in-house tool for the identification procedure has been developed.

As a reference values the dynamic stiffness obtained in accordance to ASTM [7] are as follows: AN samples $= 73.9 \pm 1$ GPa, $AN+ = 73.7 \pm 1\text{GPa}, ESG = 70.9 \pm 0.5\text{GPa}$, $ESG+= 71.3 \pm 0.5\text{GPa}$. Shear modulus values AN samples $= 31.3 \pm 0.2\text{GPa}, AN+= 31.2 \pm 0.5\text{GPa}, ESG = 28.9 \pm 0.5\text{GPa}, ESG+= 29.1 \pm 0.3\text{GPa}$. One may conclude that there is only slight scatter affecting glass material stiffness in accordance with edge and temperature treatment.

Furthermore identified mechanical characteristics (for AN sample, $E = 72.51\text{GPa}, G = 29.82\text{GPa}$) with actual thickness $t = 7.88$ mm have been compared with experimental and approximation frequency results. Verification of the simple glass sheet presented in Table 2 do not show discrepancy above 1.7% and below 1% in average among all specimens for prediction of first six Eigen frequencies.

Table. 2. Identification data for annealed glass.

Obtained parameters			Physical experiments						Metamodels					
E_x	G_{xy}	t	f_1	f_2	f_3	f_4	f_5	f_6	f_1	f_2	f_3	f_4	f_5	f_6
72.51	29.82	7.88	36.0	69.2	99.7	145.2	196.0	234.7	36.0	69.2	99.7	145.3	195.8	234.8
72.53	29.79	7.88	36.0	69.2	99.7	145.0	196.0	234.7	36.0	69.2	99.7	145.2	195.8	234.7
72.58	29.67	9.81	44.7	85.7	124.2	180.0	244.0	291.5	44.9	85.8	124.1	180.1	243.7	291.1
72.51	29.82	9.76	44.5	85.5	123.5	179.5	242.5	290.2	44.6	85.5	123.4	179.5	242.4	290.0
72.60	29.61	11.96	54.7	104.2	151.2	219.0	297.2	354.2	54.7	104.3	151.4	219.0	297.2	354.1
72.58	29.66	11.94	54.5	104.2	151.2	218.5	296.7	353.7	54.6	104.2	151.1	218.8	296.5	353.6

A summary of both annealed and tempered glass with variety of edge trimming characteristics are given in Table 3. One may observe that Young's modulus tend to be over evaluated by approximately 1 GPa compared to $ASTM$ standard method. Furthermore results show good agreement in sensitivity analysis by capturing the decrease in shear modulus for tempered glass specimens.

Table. 3. Summary of annealed and tempered glass identified mechanical properties.

$Annealed$ $glass$	$f(2;0)$, Hz	$f(1;1)$, Hz	E, GPa	G, GPa	μ
AN_8mm	36.0	69.25	72.96	31.06	0.174
AN+_8mm	36.0	69.25	74.57	31.75	0.174
AN_10mm	44.75	85.75	74.52	31.39	0.187
AN+_10mm	44.50	85.50	73.84	31.27	0.181
AN_12mm	54.75	104.25	74.44	30.94	0.203
AN+_12mm	54.50	104.25	72.66	30.48	0.192

$Tempered$ $glass$	$f(2;0)$, Hz	$f(1;1)$, Hz	E, GPa	G, GPa	μ
ESG_8mm	32.25	66.25	70.68	28.72	0.230
ESG+_8mm	32.25	66.25	70.68	28.72	0.230
ESG_10mm	44.00	83.25	70.42	28.92	0.218
ESG+_10mm	44.25	83.75	71.53	29.39	0.217
ESG_12mm	54.00	102.00	71.51	29.25	0.222
ESG+_12mm	53.75	101.25	71.69	29.16	0.229

5. Conclusions

Comparing ASTM standard method and inverse method it has been concluded that inverse method could be assumed to be more accurate as it exploited all tested self-frequencies, in contrary to only first two. Both estimates are in good agreement as inverse method complies with uncertainty indicated in ASTM method.

As a further step will validate results from non-destructive tests with conventional 4-point bending results and to apply inverse methodology for identification of laminated glass properties and viscoelastic adhesive properties.

References

[1] M. Feldmann and R. Kasper. *Guidance for European Structural Design of Glass Components*. Luxembourg: Publications Office of the European Union, 2014, 196 p.

[2] C. Schittich and G. Staib. *Glass Construction Manual*. Institut fur Internationale Architektur-Dokumentation GmbH, Munich, 2006, 352 p.

[3] L. Sable and K. Kalnins. *Evaluation of glass in design of load bearing structures*. *Civil Engineering '13, 4th International Scientific Conference Proceedings*, Latvia, Jelgava, 16–17 May, 2013, Jelgava, 2013, pp. 46–52.

[4] F.A. Veer. The strength of glass, a nontransparent value. *Heron* ,Vol. 52, 2007, pp. 87–104.

[5] EN 1288-3:2001 “Glass in building-Determination of the bending strength of glass- Part 3: Test with specimen supported at two points (four point bending)”, Brussels, 2001.

[6] ASTM E1876-01, *Standard Test Method for Dynamic Young’s Modulus, Shear Modulus, and Poisson’s Ratio by Impulse Excitation of Vibration*. New York, 2002.

[7] E. Barkanov, E. Skukis and B. Petitjean. Characterisation of viscoelastic layers in sandwich panels via an inverse technique. *Journal of Sound and Vibration*, Vol. 327, 2009, pp. 402–412.

[8] P. Ragauskas and E. Skukis. Material properties identification. Comparison of two techniques. ISSN 1392-1207, *Mechanika*, No 1(57), 2007, pp. 39–44.

[9] ANSYS® Academic Research, Release 16.0.

[10] J. Auziņš and A. Januševskis. *Eksperimentu plānošana un analīze*. Riga, RTU publishing, 208 p.(in Latvian lang.)

[11] G. Jekabsons. *A software tool for regression modelling using various modelling methods*. RTU, 2010.

Optimization of the holding system of floating marine objects on the basis of numerical modeling of their behavior

Ilya Teslyaruk[1], **Alexander Bolshev**[2]

Institute of Civil Engineering, Peter the Great St. Petersburg Polytechnic University
Saint-Petersburg, Russia
[1]iteslyaruk@gmail.com, [2]bolshev@cef.spbstu.ru

Abstract. In article, the procedure of optimization of holding systems of marine floating objects based on execution of serial mathematical experiments simulating the behavior of floating anchored structures under the influence of various external loading is considered. Elements, components, methodologies of mathematical simulation and procedures of enhancement of holding systems of floating objects are described.

Keywords: *mathematical modeling, floating anchored objects, external loads, optimization of holding systems, safety of marine objects.*

1. Introduction

In case of design and operation of various floating marine objects, it is necessary to analyze a wide range static and dynamic tasks, studying relocation of these objects under the influence of a wind, waves and currents. Usually for safety of floating object it is necessary to design completely system of its holding and/or to set up its parameters; to specify the level of external influences in case of which safety of object is guaranteed. Thus, being guided by duration of operation of objects, it is necessary to study behavior of constructions under the influence of the most different combinations of external influences. The most universal and rather cheap method of the solution of the specified complex of questions, use of methods of mathematical simulation of behavior of floating constructions for search of options and enhancement of systems of their holding is.

In this operation for the solution of the specified tasks the program package “Anchored Structures” [1] developed at the St. Petersburg Polytechnic University with assistance of the Russian Maritime Register of Shipping is used.

2. Problem formulation

Design of new holding system of floating marine object, usually, provides a choice of number of anchor lines; caliber of chains or cables of which they consist; lengths of each line or position of an anchor; spatial arrangement of lines; initial tension of lines; type of an anchor and an assessment of its holding ability on this or that ground soil.

At design of holding system of already existing object it is possible to change only the position of anchors, the spatial position of lines and their initial tension.

Optimal new retention system usually is defined by the minimum length and caliber of lines with which it is provided performance of a number of limitations of the external influences guaranteeing safe operation of a construction at any possible combination.

For the already existing object the length, the spatial arrangement and the initial tension of lines in which restrictions on safety of a construction remain in all possible combinations of external influences or in the widest range of influences define the optimality of holding system.

Thus, search of optimal holding system assumes repeated modeling of behavior of floating object under the influence of various combinations of external forces; check of restrictions by criteria of safety of a construction in each of estimated cases; modification of variable parameters of retention system for search of the optimal engineering decision.

2.1. Geometrical modeling of the hull of marine object

Mathematical simulation behavior of floating object begins with creation of three-dimensional geometrical model. In this case the solid-state model is created in the program AutoCAD (Fig. 1). In the same place the surface model of object is created. By means of the special interface of model are transferred to the simulating complex and are used for display of behavior of object in real time in the course of mathematical simulation (Fig. 2) and for calculation of external loadings (Fig. 3).

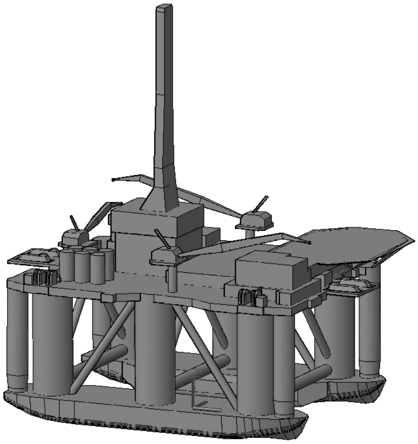

Fig. 1. Three-dimensional geometric model of a floating object in AutoCAD.

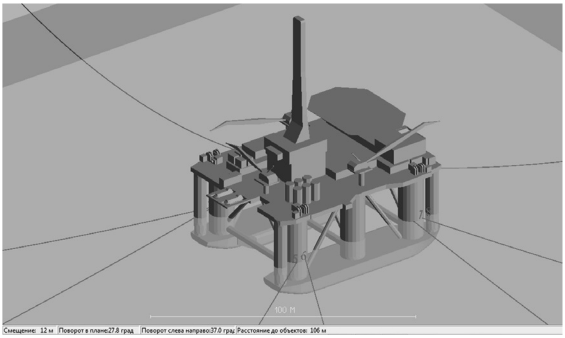

Смещение: 12 м | Поворот в плане:27.8 град | Поворот слева направо:37.0 гра | Расстояние до объектов: 106 м

Fig. 2. Three-dimensional geometric model of a floating object in the program “Anchored Structures”.

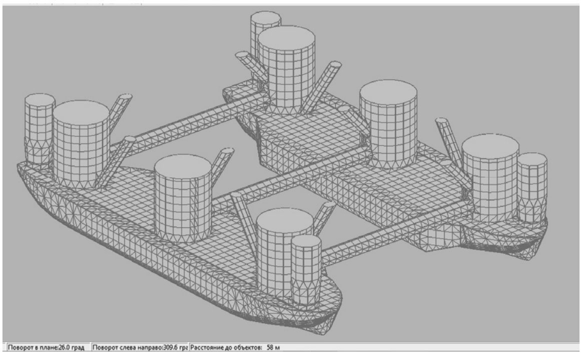

Поворот в плане:26.0 град | Поворот слева направо:309.6 гра | Расстояние до объектов: 58 м

Fig. 3. Surface model of the wetted part of the hull of floating object in the program "Anchored Structures".

2.2. Simulation of external loads on the floating object

The most considerable external loads of buoyant object are connected to impact of disturbance. Within this operation the irregular waves were represented by the range consisting of set of elementary harmonic waves. Thus simulation of a two-dimensional uneasy surface of the sea (a deviation from zero level of a quiet surface of $\varsigma(x,t)$ is carried out by means of the following representation :

$$\varsigma(x,t)=\sum_{i=1}^{N} a_i\cos(k_i x-\omega_i t+\varphi_i), \tag{1}$$

where $a_i=\sqrt{2S(\omega_i)\Delta\omega_i}$ – the amplitude of the i-th harmonic spectrum; k_i – wave number of the i-th harmonic spectrum; ω_i – angular frequency of the i-th harmonic spectrum; φ_i – random phase of i-th harmonic spectrum uniformly distributed in the range $[0,2\pi]$; $\Delta\omega_i$ – the frequency range of the spectrum $[\omega_i-\Delta\omega_i/2,\omega_i+\Delta\omega_i/2]$, which determines the amplitude of the i-th harmonic; x – the horizontal coordinate along the direction of wave propagation; t – time.

The vector of a wave load on a construction in 6 levels of freedom $\mathbf{F}_w(t)$, depending on the time, was determined by the following formula:

$$\mathbf{F}_w(t)=\sum_{i=1}^{N}\sum_{n=1}^{M}\mathbf{F}_{in}(\omega_i,\theta_n)\sin(\omega_i t+\varphi_{in}), \tag{2}$$

where $\mathbf{F}_{in}(\omega_i,\theta_n)$ – vector of amplitudes of loading from i-th harmonic spectrum of excitement propagating in the direction of the n-th; t – time; ω_i – the angular frequency; φ_{in} – phase of i-th harmonic spectrum of the load; N,M – the number of partitions of the three-dimensional spectral intervals.

For receiving wave loads and hydrodynamic characteristics of constructions in a program complex the variety of widely known method of hydrodynamic features – a method of spatial sources of radiation – is used [2]. This method is based on obtaining the filling and reflected potentials of disturbance and integration of resultant liquid pressures on the wetted surface of a construction.

In case of calculation of forces and the moments from a wind the problem definition assuming existence of prior data about the sail area and resistance when blowing a construction under different angles was used.

In this case the wind load on a construction is calculated by a formula:

$$F = \varrho_a \bar{V}_w^2 C_w A_w(\alpha_w - x_6)/2, \tag{3}$$

where $\bar{V}_w$ – the estimated average wind speed, $\mathrm{m/s}$; ϱ_a – density of air; $A_w(\alpha)$ – function of the sail area from an angle of the direction of a wind concerning a construction; C_w– resistance coefficient; x_6 – construction turning angle in the plan.

In case of the account dynamic component of wind speed was presented in the form:

$$V_w = \bar{V}_w + V_w'. \tag{4}$$

The dynamic component of the wind speed spectrum V_w' is described by wind gusts according to regulatory documents ISO1901-1 [3].

Calculation of forces and the moments from a current assumes existence of prior data about the area of underwater windage of object and resistance in case of a construction flow under different angles. Determination of forces of a current was executed on estimated formulas similar (3).

2.3. Simulation of holding system

The modelled anchor lines can represent different types of rope, circuits, flexible connections of pipes or any their combinations.

Calculation of stresses in anchor lines was made by a quasistatic method, with small depths of the sea [4], thus the tension and a path of the line were function of provision of a hawse point of a construction. In case of calculation of anchor lines their stretching and possibility of laying down of part of line on a water area bottom which, in turn, can have an inclination were considered.

In case of big to sea depths response of anchor lines was calculated by a dynamic method (taking into account dynamics of lines). In this setting, the lines were considered as elastic, heavy, flexible threads the weight of which concentrates in nodal points [5]. Thus, each line was described as a daisy of elementary masses connected by elastic weightless threads.

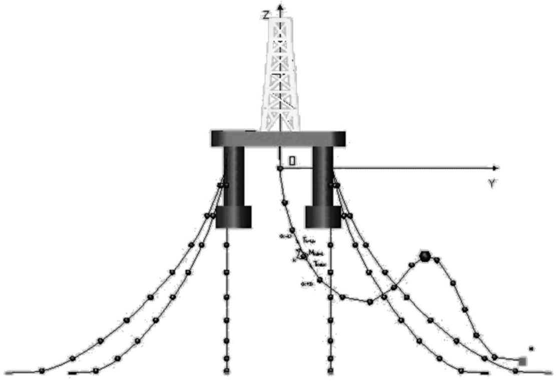

Fig. 4. Simulation of dynamics of floating object together with dynamics of lines.

2.4. Solution of static and dynamic tasks

In case of simulation of tasks of a statics the decision of system of six non-linear algebraic equations representing [6] a balance of all the forces acting on structure was made:

$$\mathbf{C}(\mathbf{X}_c) + \mathbf{F}_R(\mathbf{X}_c, \mathbf{L}_1) + \mathbf{F}_S(\mathbf{X}_c) + \mathbf{F}_B(\mathbf{X}_c) + \mathbf{F}_{df} + \mathbf{F}_w + \mathbf{F}_c + \mathbf{F}_i = 0, \tag{5}$$

where $\mathbf{F}_{df}$, $\mathbf{F}_w$, $\mathbf{F}_c$, $\mathbf{F}_i$ – external static forces of wave drift from a wind, a current and ice respectively; $\mathbf{X}_c$ – the displacement vector of a construction in six levels of freedom; $\mathbf{C}(\mathbf{X}_c)$ – vector of restoring forces; $\mathbf{F}_R(\mathbf{X}_c, \mathbf{L}_1)$ – vector of the forces of reaction system of anchoring; $\mathbf{F}_S(\mathbf{X}_c)$ – vector of reaction of mooring lines; $\mathbf{F}_B(\mathbf{X}_c)$ – vector of reaction of fenders.

The dynamic problem was solved in a time domain by means of integration of system of ordinary non-linear differential equations of movement of anchored floating object [1].

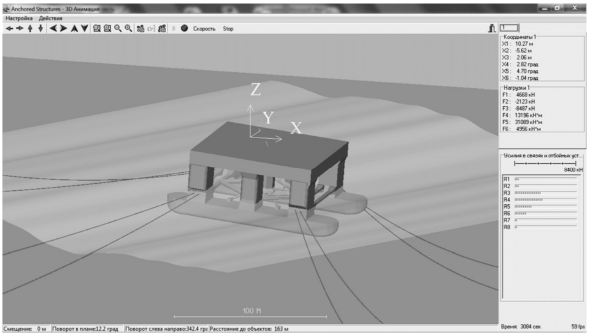

Координаты 1
X1: 10.27 м
X2: -5.62 м
X3: 2.06 м
X4: 2.82 град
X5: 4.70 град
X6: -1.04 град

Нагрузки 1
F1: 4668 кН
F2: -2123 кН
F3: -8487 кН
F4: 13196 кН*м
F5: 31089 кН*м
F6: 4956 кН*м

Смещение: 0 м
Поворот в плане:12.2 град
Поворот слева направо:342.4 гр
Расстояние до объектов: 163 м
Время: 3084 сек
59 fps

Fig. 5. Simulation of pitching of floating object in a 100-year storm repetition.

3. Restrictions on the behavior of the floating object

Safety of operation of the floating object is usually determined by performing the following restrictions: the maximum permissible vertical and horizontal movement; the maximum permissible angles of heel and trim; minimum permissible reserves of tension in the anchor links; minimum permissible reserves the horizontal load transferred to the anchor.

The listed restrictions, as a rule, are specified for the construction survival modes during an extremal storm [7], for the modes of operation or for execution of specific sea operations and depend on the accepted calculation method (quasistatic or dynamic).

3.1. Plan of numerical experiment

For execution of numerical experiment at first the matrix of estimated cases enveloping possible combinations of levels of external influences from a wind, disturbances and currents taking into account a variation of propagation directions of a wind and disturbance in the range from 0 to 360 ° was formed.

Further, for some initial values of parameters of holding systems modeling of the entire matrix of the estimated cases was executed, execution of restrictions on safe criterions was analyzed and critical combinations of external influences in case of which the situation appeared the worst. The values of the maximum displacement of the floating objects or coefficients of margin of safety of anchor lines in case of a critical combination of external influences were associated with the selected earlier variable parameter values of holding systems.

Further, modification of parameters of holding systems was executed and the cycles of simulation were repeated until it was possible to provide execution of all safe criterions in case of all possible combinations of external influences.

4. Conclusions

Use of methods of mathematical modeling and application of high-settlement complex allow to formalize the task of finding the best parameters of holding systems of floating anchored objects by busting combinations of external influences. Simulation of behavior of object in case of implementation of each combination, assessment of safety of object in each estimated case and coherent modification of the parameters of holding systems to ensure safe operation of the floating object at all possible levels of external load.

References

[1] А.С. Большев, М.А. Кутейников и С.А. Фролов. Математическое моделирование морских плавучих объектов в программном комплексе “Anchored Structures”. *Научно-технический сборник РМРС*, вып. 36, 2013, стр. 68–90.

[2] C.J. Garrison and P.Y. Chow. Wave forces on submerged bodies. *Journal of Waterways, Harbors and Coastal Engineering,* Proceedings of American Society of Civil Engineering, Vol. 98, No. WW3, 1972, pp. 375–392.

[3] ISO 19901-1 Petroleum and natural gas industries Specific requirements for offshore structures Part 1: Metocean design and operating considerations, 2005, 135 pp.

[4] С.А Фролов. Статика и динамика плавучих сооружений, закрепленных гибкими упругими связями. *Реферат диссертации на соискание ученой степени кандидата технических наук*, СПб, СПбГТУ, 1992 г., 16 с.

[5] Bolshev A.S. *Statics and dynamics of anchored floating structures with non-linear characteristics of anchored system Monograph*, Gdansk, 1993, 218 p.

[6] А.С Большев и С.А. Фролов. Применение векторных кусочно-линейных операторов в нелинейных задачах статики и динамики заякоренных сооружений. *Строительная механика и расчет сооружений*. Сб. науч. тр. СПбГТУ, СПб, 1992, с. 137–144.

[7] Правила классификации, постройки и оборудования плавучих буровых установок и морских стационарных платформ. *РМРС*, СПб, 2014, 479 с.

Cubic spline collocation method for linear Fredholm integral equations with diagonal and boundary singularities

Mikk Vikerpuur

Institute of Mathematics, University of Tartu
Tartu, Estonia
azzo@ut.ee

Abstract. The numerical solution of a class of linear Fredholm integral equations of the second kind by the collocation method is discussed. The kernel of the integral equation may have weak diagonal and boundary singularities. Using C^2-smooth cubic splines and special non-uniform grids, the convergence rate of proposed numerical schemes is studied for all values of the non-uniformity parameter of the grid.

Keywords: *weakly singular integral equation, boundary singularity, cubic spline collocation method, graded grid.*

1. Introduction

We consider a linear Fredholm type integral equation of the form

$$u = T_K u + f, \tag{1}$$

where $f \in C[0,1]$ and T_K is an integral operator defined by the formula

$$(T_K u)(x) = \int_0^1 K(x,y)u(y)dy,\ 0 \le x \le 1. \tag{2}$$

By $C^k(\Omega)$ $(k \ge 0)$ we denote the set of all k times continuously differentiable functions on $\Omega, C^0(\Omega) = C(\Omega)$. In particular, by $C[0,1]$ we denote the Banach space of continuous functions z on $[0,1]$ with the norm $\|z\|_\infty = \sup_{0\le x\le 1} |z(x)|$.

In practice (see e.g. [5, 6]) the kernel $K(x,y)$ may often have a weak singularity on the diagonal $x = y$: $K(x,y) = a(x,y)|x-y|^{-\nu}$, $0 < \nu < 1, a \in C([0,1]\times[0,1])$. In this paper we will consider a more complicated situation for (1)–(2) where the kernel $K(x,y)$ may have a diagonal singularity at $x = y$ and additionally a boundary singularity at $y = 0$ and/or at $y = 1$. More precisely, we assume that $K \in W^{m,\nu,\varrho_0,\varrho_1}$, where $W^{m,\nu,\varrho_0,\varrho_1} = W^{m,\nu,\varrho_0,\varrho_1}([0,1]\times(0,1))$ consists of m times $(m \ge 0)$ continuously differentiable functions K on $\big([0,1]\times(0,1)\big) \setminus \{(x,y) \in \mathbf{R}^2 : x = y\}$ that satisfy there, for all $k, l, k+l \le m$, the inequalities

$$\left|\left(\frac{\partial}{\partial x}\right)^k \left(\frac{\partial}{\partial x} + \frac{\partial}{\partial y}\right)^l K(x,y)\right| \le c|x-y|^{-\nu-k}\, y^{-\varrho_0-l}(1-y)^{-\varrho_1-l}. \tag{3}$$

Here $c = c(m,K)$ is a positive constant which is independent of x and y, and

$$0 < \nu < 1,\ \ 0 \le \varrho_0 < 1-\nu,\ \ 0 \le \varrho_1 < 1-\nu. \tag{4}$$

Clearly, $W^{m,\nu,\varrho_0,\varrho_1} \subset W^{0,\nu,\varrho_0,\varrho_1}$ for any $m \in \mathbf{N} = \{1,2,\dots\}$. Note that kernels of the form

$$K(x,y) = a(x,y)|x-y|^{-\nu} y^{-\varrho_0}(1-y)^{-\varrho_1} + b(x,y),$$

with

$$a \in C^m([0,1]\times[0,1]), b \in C^m([0,1]\times[0,1]), m \in \{0,1,\dots\}$$

and $\nu, \varrho_0, \varrho_1$ satisfying (4), belong to $W^{m,\nu,\varrho_0,\varrho_1}$.

The main difficulty with this type of equations (1)–(2) is that their solutions (if they exist) are typically singular near the boundary of the interval $[0,1]$ where their derivatives become unbounded (see Lemma 3 below). This complicates the construction of high order methods for the numerical solution of equation (1)–(2). We construct, for equation (1)–(2), a high order collocation method which is based on C^2-smooth cubic splines and graded grids reflecting the singular behavior of the exact solution. We use some ideas of [2, 3, 6], see also [4].

Throughout the paper c is a positive constant which may have different values by different occurrences. For a Banach space E, by $L(E)$ we will denote the Banach space of linear bounded operators $A: E \to E$ with the norm $\|A\|_{L(E)} = \sup\{\|Ax\|_E : x \in E, \|x\|_E = 1\}$.

2. Regularity of the solution

For given $k \in \boldsymbol{N}$ and $\alpha, \beta \in (0,1)$, let $C^{k,\alpha,\beta}(0,1)$ be the set of functions $z \in C[0,1] \cap C^k(0,1)$ such that

$$\left|z^{(j)}(x)\right| \le c\, x^{1-\alpha-j}(1-x)^{1-\beta-j}, \quad 0 < x < 1,$$

where $j = 1, \dots, k$. Clearly, $C^k[0,1] \subset C^{k,\alpha,\beta}(0,1)$, $k \in \mathbf{N}$, $\alpha, \beta \in (0,1)$.

Due to [1] it is easy to see that the following lemma holds.

Lemma 1. *Let* $K \in W^{0,\nu,\varrho_0,\varrho_1}, 0 < \nu < 1, 0 \le \varrho_0 < 1-\nu, 0 \le \varrho_1 < 1-\nu$. *Then* T_K, *defined by the formula (2) is compact as an operator from* $C[0,1]$ *into* $C[0,1]$.

Denote

$$N(I - T_K) = \{u \in C[0,1]: u = T_K u\},$$

where I is the identity mapping in the space $C[0,1]$. A consequence of Lemma 1 is the following result.

Lemma 2. *Let* $f \in C[0,1], K \in W^{0,\nu,\varrho_0,\varrho_1}, 0 < \nu < 1, 0 \le \varrho_0 < 1-\nu, 0 \le \varrho_1 < 1-\nu$ *and let* $N(I - T_K) = \{0\}$. *Then equation (1) is uniquely solvable and its solution belongs to* $C[0,1]$.

It follows from [1] that the regularity of a solution to (1) can be characterized by the following lemma.

Lemma 3. *Let* $K \in W^{m,\nu,\varrho_0,\varrho_1}, f \in C^{m,\nu+\varrho_0,\nu+\varrho_1}(0,1)$, $m \in \boldsymbol{N}, 0 < \nu < 1, 0 \le \varrho_0 < 1-\nu, 0 \le \varrho_1 < 1-\nu$, *and let equation (1) have a solution* $u \in C[0,1]$. *Then* u *belongs to* $C^{m,\nu+\varrho_0,\nu+\varrho_1}(0,1)$.

3. Cubic spline collocation method

For given $N \in \mathbf{N}$ $(N \ge 2)$ and $r \in [1, \infty)$ let $\Delta_N^{(r)} = \{t_0, \dots, t_{2N}: 0 = t_0 < \dots < t_{2N} = 1\}$ be a grid on $[0,1]$ such that

$$t_j = \frac{1}{2}\left(\frac{j}{N}\right)^r, j = 0, \dots, N; \quad t_{N+j} = 1 - t_{N-j}, j = 1, \dots, N. \tag{5}$$

If $r = 1$, then $\Delta_N^{(r)}$ is a uniform grid with the knots $t_j = jh, h = 1/(2N), j = 0, \dots, 2N$. If $r > 1$, then the grid points (5) are more densely clustered near the boundary of the interval $[0,1]$. Denote by $\mathcal{P}_3$ the set of polynomials of degree ≤ 3 and let $S_3^{(2)}\left(\Delta_N^{(r)}\right)$ be the space of cubic splines on $\Delta_N^{(r)}$: $S_3^{(2)}(\Delta_N^{(r)}) = \{z_N \in C^2[0,1]:\ z_N|_{[t_{j-1},t_j]} \in \mathcal{P}_3\,, j = 1,\dots,2N\}$, where $z_N|_{[t_{j-1},t_j]}$ is the restriction of z_N to $[t_{j-1}, t_j]$.

We find an approximation u_N for u, the solution to (1), determining u_N from the following conditions:

$$u_N \in S_3^{(2)}\left(\Delta_N^{(r)}\right), N \geq 2, \tag{6}$$

$$u_N(t_i) - \int_0^1 K(t_i, s) u_N(s)\, ds = f(t_i),\ \ i = 0,\dots,2N, \tag{7}$$

$$\lim_{t\to t_i, t<t_i} u_N'''(t) = \lim_{t\to t_i, t>t_i} u_N'''(t)\,, i = 1, i = 2N-1. \tag{8}$$

The settings (6)–(8) form a system of equations whose exact form is determined by the choice of a basis in the space $S_3^{(2)}\left(\Delta_N^{(r)}\right)$ of cubic splines on $\Delta_N^{(r)}$. For example, we can seek u_N in the form

$$u_N(t) = \sum_{j=-3}^{2N-1} c_j B_j(t)\,, t \in [0,1], \tag{9}$$

where $\{c_j\}$ are unknown coefficients and $\{B_j(t)\}$ are the cubic B-splines with the minimal support $[t_j, t_{j+4}]$. About the construction of B-splines see, for example, [7]. We note that, in addition to the points $0 = t_0 < t_1 < \cdots < t_{2N} = 1$ of the grid $\Delta_N^{(r)}$, for the construction of B-splines $B_j(t)$ $(j = -3, -2, \dots, 2N-1)$, six additional points $t_{-3} < t_{-2} < t_{-1} < 0$ and $1 < t_{2N+1} < t_{2N+2} < t_{2N+3}$ from outside of the interval [0,1] are necessary. We choose them as follows: $t_i = -i(t_1 - t_0), t_{2N+i} = 1 + i(t_{2N} - t_{2N-1}), i = 1,2,3$. Actually, $B_j(t)$ can be presented in the form (see [7])

$$B_j(t) = 4\sum_{k=j}^{j+4} \frac{(t_k - t)_+^3}{\omega_j'(t_k)}\,, t \in \mathbf{R},$$

where $j = -3, \dots, 2N-1$,

$$(t_k - t)_+^3 = \begin{cases} (t_k - t)^3 & \text{for } t_k - t \geq 0, \\ 0 & \text{for } t_k - t < 0, \end{cases}$$

$\omega_j(t) = (t - t_j)(t - t_{j+1})(t - t_{j+2})(t - t_{j+3})(t - t_{j+4})$, with $t \in \mathbf{R}, j = -3, \dots, 2N-1$.

Substituting (9) into (7)–(8), we obtain $2N+3$ equations with respect to $2N+3$ coefficients $c_{-3}, c_{-2}, \dots, c_{2N-1}$:

$$\sum_{j=-3}^{0} c_j \lim_{t\to t_1, t<t_1} B_j'''(t) = \sum_{j=-2}^{1} c_j \lim_{t\to t_1, t>t_1} B_j'''(t),$$

$$\sum_{j=i-3}^{i-1} c_j\ B_j(t_i) - \sum_{j=-3}^{2N-1} c_j \int_0^1 K(t_i, s) B_j(s)\, ds = f(t_i),\ \ i = 0, \dots, 2N,$$

$$\sum_{j=2N-5}^{2N-2} c_j \lim_{t\to t_{2N-1},t<t_{2N-1}} B_j'''(t) = \sum_{j=2N-4}^{2N-1} c_j \lim_{t\to t_{2N-1},t>t_{2N-1}} B_j'''(t).$$

Theorem 1. *Let* $f \in C[0,1], K \in W^{0,\nu,\varrho_0,\varrho_1}$, $0<\nu<1, 0 \le \varrho_0 < 1-\nu, 0 \le \varrho_1 < 1-\nu$. *Furthermore, assume that* $N(I-T_K)=\{0\}$ *and the grid points (5) of the grid* $\Delta_N^{(r)}$ *with* $r \in [1,\infty)$ *are used. Then equation (1) has a unique solution* $u \in C[0,1]$, *the settings (6)–(8) determine for sufficiently large* N, *say* $N \ge N_0$ $(N_0 \ge 2)$, *a unique approximation* $u_N \in S_3^{(2)}\left(\Delta_N^{(r)}\right) \subset C[0,1]$ *for* u, *and*

$$\max_{x\in[0,1]} |u_N(x)-u(x)| \to 0 \text{ as } N \to \infty. \tag{10}$$

Proof. It follows from Lemma 2 that the equation (1) has a unique solution $u \in C[0,1]$. The conditions (6)–(8) have an operator equation representation

$$u_N = P_N T_K u_N + P_N f. \tag{11}$$

Here $P_N: C[0,1] \to C[0,1]$ is an interpolation operator which assigns to each function $u \in C[0,1]$ its piecewise cubic interpolation function $P_N u \in S_3^{(2)}\left(\Delta_N^{(r)}\right) \subset C[0,1]$ satisfying the following conditions:

$$(P_N u)(t_i) = u(t_i),\ i = 0,\dots,2N;\ \lim_{t\to t_j,t<t_j} (P_N u)'''(t) = \lim_{t\to t_j,t>t_j} (P_N u)'''(t),$$

where $j=1$ and $j=2N-1$. We find (see [6]) that $P_N \in L(C[0,1]), \|P_N\|_{L(C[0,1])} \le c, N \in \mathbf{N}$, with a constant $c>0$ which is independent of N, and

$$\|u-P_N u\|_\infty \to 0 \text{ as } N \to \infty \text{ for any } u \in C[0,1]. \tag{12}$$

This, together with Lemma 1, yields that

$$\|T_K - P_N T_K\|_{L(C[0,1])} \to 0 \text{ as } N \to \infty\ . \tag{13}$$

Further, it follows from Lemma 2 that $I-T_K$ is invertible in $C[0,1]$ and $(I-T_K)^{-1} \in L(C[0,1])$. This together with (13) yields that $I-P_N T_K$ is invertible in $C[0,1]$ for all sufficiently large N, say $N \ge N_0$, and $\|(I-P_N T_K)^{-1}\|_{L(C[0,1])} \le c$, $N \ge N_0$, with a constant $c>0$ which is independent of N. Thus, for $N \ge N_0$ equation (11) (method (6)–(8)) provides a unique solution $u_N \in S_3^{(2)}\left(\Delta_N^{(r)}\right) \subset C[0,1]$. We have, for it and u, the solution of equation (1), that $u_N - u = (I-P_N T_K)^{-1}(P_N u - u)$
and

$$\|u_N - u\|_\infty \le \mathrm{c}\|P_N u - u\|_\infty, N \ge N_0, \tag{14}$$

with a constant $c>0$ which is independent of N. This, together with $u \in C[0,1]$ and (12) yields (10).

Further, due to [3], we have the following result.

Lemma 4. *Let* $u \in C^{4,\nu+\varrho_0,\nu+\varrho_1}(0,1)$, $0<\nu<1$, $0 \le \varrho_0 < 1-\nu$, $0 \le \varrho_1 < 1-\nu$. *Then, for sufficiently large* N, *say* $N \ge N_0$ $(N_0 \ge 2)$,

$$\|P_N u - u\|_\infty \le c\varepsilon_N^{(r,\nu,\varrho)},$$

with

$$\varepsilon_N^{(r,\nu,\varrho)} = \begin{cases} N^{-r(1-\nu-\varrho)} & \text{for } 1 \le r < \dfrac{4}{1-\nu-\varrho}, \\ N^{-4} & \text{for } \quad r \ge \dfrac{4}{1-\nu-\varrho}. \end{cases} \tag{15}$$

Here $\varrho = max\{\varrho_0, \varrho_1\}$ *and* c *is a positive constant not depending on* N.

Theorem 2. *Let* $K \in W^{4,\nu,\varrho_0,\varrho_1}$, $f \in C^{4,\nu+\varrho_0,\nu+\varrho_1}(0,1)$, $0 < \nu < 1$, $0 \le \varrho_0 < 1-\nu$, $0 \le \varrho_1 < 1-\nu$. *Assume that* $\mathcal{N}(I - T_K) = \{0\}$ *and the grid points (5) of the grid* $\Delta_N^{(r)}$ *with* $r \in [1,\infty)$ *are used.*

Then method (6)–(8) determines for $N \ge N_0$ $(N_0 \ge 2)$ *a unique approximation* u_N *for* u*, the solution to (1), and*

$$\max_{x\in[0,1]} |u_N(x) - u(x)| \le c\varepsilon_N^{(r,\nu,\varrho)}, \tag{16}$$

where $\varepsilon_N^{(r,\nu,\varrho)}$ *is defined by the formula (15),* $\varrho = max\{\varrho_0, \varrho_1\}$ *and* c *is a positive constant not depending on* N.

Proof: It follows from Theorem 1 that method (6)–(8) determines for $N \ge N_0$ a unique approximation $u_N \in S_3^{(2)}(\Delta_N^{(r)})$ to $u \in C[0,1]$, the solution of equation (1). With the help of Lemma 3 we obtain that $u \in C^{4,\nu+\varrho_0,\nu+\varrho_1}(0,1)$. This together with the estimate (14) and Lemma 4 yields the estimate (16).

Acknowledgements

The supports from the Estonian Science Foundation through the Grant No. 9104 and from the Institutional research funding IUT20-57 of the Estonian Ministry of Education and Research are acknowledged.

References

[1] A. Pedas and G. Vainikko. Integral equations with diagonal and boundary singularities of the kernel. Zeitschrift für Analysis und Ihre Anwendungen, Vol. 25, 2006, pp. 487–516.

[2] A. Pedas and M. Vikerpuur. Smoothing transformation and cubic spline collocation for weakly singular Fredholm integral equations with boundary singularities. AIP Conference Proceedings, Vol. 1479, 2012, pp. 708–711.

[3] A. Pedas and M. Vikerpuur. Cubic spline collocation for a class of weakly singular Fredholm integral equations and corresponding eigenvalue problem. Proceedings of the 17th WSEAS International Conference on Applied Mathematics, Mathematical Methods for Information Science and Economics, Montreux, Switzerland, December 29-31, 2012, WSEAS Press, 2012, pp. 127–132.

[4] P. Uba. A collocation method with cubic splines for multidimensional weakly singular nonlinear integral equation. Journal of Integral Equations and Applications, Vol. 6, No. 2, 1994, pp. 257–266.

[5] G. Vainikko. Multidimensional Weakly Singular Integral Equations. Springer-Verlag, Berlin, 1993.

[6] G. Vainikko, A. Pedas and P. Uba. Methods for Solving Weakly Singular Integral Equations. Tartu, 1984 (in Russian).

[7] Yu.S. Zavyalov, B.I. Kvasov and V.L. Miroshnichenko. Methods of Spline Functions. Moscow, 1980 (in Russian).

Optimal thickness of a cylindrical shell under dynamical loading

Paul Ziemann

Institute of Mathematics and Computer Science,
E.-M.-A. University
Greifswald, Germany
paul.ziemann@uni-greifswald.de

Abstract. In this paper an optimization problem for a cylindrical shell under an applied dynamical loading is discussed. The aim is to look for an optimal thickness of a shell to minimize the deformation when the shell is subject to an external time-dependent force together with an initial impact. The volume of the shell has to stay constant during optimization. A model for the deflection is derived and analyzed and a corresponding optimal control problem is formulated. Numerical solutions are presented for a cylindrical panel with a body falling down onto the opposite side of the shell's only clamped edge and then staying there.

Keywords: *optimal control of PDE, shape optimization, linear elasticity.*

1. Introduction

In this paper we discuss an optimization problem in linear elasticity, particularly in shape optimization. The aim is to look for an optimal thickness of a cylindrical shell to minimize the deformation under an initial impact and a (time-dependent) external force, i.e. in a dynamical setup. As an additional restriction, the volume of the shell is prescribed. The deflection is modelled using a generalization of the steady-state "basic shell model" [1] which makes use of the hypothesis of Mindlin and Reissner but no further simplifications like in Naghdy or Koiter models. Optimization results for steady-state can be found in [2] and for dynamic conditions with rotational symmetric loading in [3].

After stating the deflection model and the optimal control problem we give some analytical results regarding existence and uniqueness of solutions as well as continuity and differentiability of the deflection with respect to the thickness of the shell. We then focus on the numerical solution to an example of a cylindrical panel with one clamped edge and a body falling down onto the shell at the opposite side of that edge leading to an initial impact and then acting with its weight force. This problem was formulated by J. Lellep from University of Tartu.

2. Geometrical description of the shell

For the geometrical description, we first need a chart describing the midsurface of the shell. Let $\omega = [0, l] \times [\varphi_a, \varphi_b]$ be the parameter region and $z\colon \omega \to \mathbb{R}^3$, $z(x, \varphi) = (x, R\cos\varphi, R\sin\varphi)$ be a mapping to describe the midsurface of a cylindrical panel with length l and radius R. We call $\mathcal{S} = z(\omega)$ the midsurface of the shell. The vectors $a^1 = (1, 0, 0)$ and $a^2 = 1/R(0, \sin\varphi, \cos\varphi)$ form a local contravariant basis on $\mathcal{S}$. Additionally, we consider an orthonormal vector $a_3 = (0, \cos\varphi, \sin\varphi)$. To describe the shell body we introduce $\tau\colon \mathcal{S} \to \mathbb{R}^+, \tau \in W^{1,\infty}(\mathcal{S})$ as the *thickness* of the shell and define the 3D-reference domain

$$\Omega_{(\tau)} := \left\{ (x,\varphi,h) \in \mathbb{R}^3 \mid (x,\varphi) \in \omega, h \in \left(-\frac{\tau(x,\varphi)}{2}, \frac{\tau(x,\varphi)}{2} \right) \right\} \tag{1}$$

together with the mapping $\Phi_{(\tau)}: \Omega_{(\tau)} \to \mathbb{R}^3$

$$\Phi_{(\tau)}(x,\varphi,h) = z(x,\varphi) + ha_3 = (0, (R+h)\cos\varphi, (R+h)\sin\varphi). \tag{2}$$

We call $\mathcal{B}_\tau := \Phi_{(\tau)}(\Omega_{(\tau)})$ the shell. Let us denote a local covariant basis with $g_1 = (1,0,0), g_2 = (R+h)(0, -\sin\varphi, \cos\varphi)$ and $g_3 = a_3$. In the context of shells, we assume τ to be *small* other dimensions, in particular $\tau(x,\varphi) < R$.

3. Modeling the displacement

We consider a small displacement $U: \mathcal{B}_{(t)} \to \mathbb{R}^3$ of the shell. For modeling we use the Reissner-Mindlin kinematical assumptions, which state that normals to the midsurface remain straight and unstretched during deformation. This leads to the displacement approach

$$U(x,\varphi,h) = u(x,\varphi) + h\theta(x,\varphi) \tag{3}$$

with $u = u_1 a^1 + u_2 a^2 + u_3 a_3$ describing a translation of all points on a line normal to the midsurface in $z(x,\varphi)$ and $\theta = \theta_1 a^1 + \theta_2 a^2$ representing a rotation vector, all in local coordinates. We introduce the space of admissible displacements

$$\mathcal{V} := \left\{ (u,\theta) \mid u = (\underline{u}, u_3) \in H^1(\mathcal{S})^2 \times H^1(\mathcal{S}), \theta \in H^1(\mathcal{S})^2 \right\} \cap \mathcal{BC} \tag{4}$$

where $H^1(\mathcal{S})$ and $H^1(\mathcal{S})^2$ are Sobolev-spaces for scalar functions and first order tensors on the midsurface, respectively. Let us assume for the boundary conditions $\mathcal{BC}$ that the shell body is hardclamped over the edge $x = 0$, i.e. $(u,\theta)|_{x=0} = 0$. We next consider the linear 3D-Green-Lagrange-strain tensor which is given by

$$e_{ij} = \frac{1}{2}\left(g_i \cdot U_{,j} + g_j \cdot U_{,i} \right), \qquad i,j = 1,2,3, \tag{5}$$

where $U_{,i}$ means the partial derivative of U w.r.t. to the i-th coordinate. Calculation leads to

$$\mathbf{e} := \begin{pmatrix} e_{11} \\ e_{22} \\ \sqrt{2}e_{12} \end{pmatrix} = \begin{pmatrix} u_{1,1} + h\theta_{1,1} \\ u_{2,2} + Ru_3 + h\left(\theta_{2,2} + \frac{1}{R}u_{2,2} + u_3 \right) + \frac{h^2}{R}\theta_{2,2} \\ \frac{1}{\sqrt{2}}\left(u_{1,2} + u_{2,1} \right) + \frac{h}{\sqrt{2}}\left(\theta_{1,2} + \theta_{2,1} + \frac{1}{R}u_{2,1} \right) + \frac{h^2}{\sqrt{2}R}\theta_{2,1} \end{pmatrix} \tag{6}$$

and shear strain

$$\zeta = \begin{pmatrix} e_{13} \\ e_{23} \end{pmatrix} = \frac{1}{2}\begin{pmatrix} \theta_1 + u_{3,1} \\ \theta_2 + u_{3,2} - \frac{1}{R}u_2 \end{pmatrix} \tag{7}$$

By Hooke's law we get a relationship between strains and stresses σ^{ij}. Adding the assumption that the normal stress σ^{33} is zero (*plain-stress*) and using Voigt-notation we later can represent the equilibrium conditions for isotropic material in a short way with help of the matrices

$$\mathbf{C} := \begin{pmatrix} L_1 + 2L_2 & \frac{1}{(R+h)^2} L_1 & 0 \\ \frac{1}{(R+h)^2} L_1 & \frac{1}{(R+h)^4}(L_1 + 2L_2) & 0 \\ 0 & 0 & \frac{2}{(R+h)^2} L_2 \end{pmatrix}, \tag{8}$$

$$\mathbf{D} := \begin{pmatrix} 4L_2 & 0 \\ 0 & \frac{4}{(R+h)^2} L_2 \end{pmatrix},$$

where $L_1 = E\nu/((1+\nu)(1-\nu))$ and $L_2 = E/(2(1+\nu))$ are the 2D-Lamé constants expressed with Young's modulus E and Poisson's ratio ν. To account for dynamical loadings and impacts we introduce a time-dependence on $\big(u(t), \theta(t)\big) =: y(t), t \in [0, T]$ and assume the deformation to be in the space

$$W(0,T) = \{y \mid y \in \ L^2(0,T;\mathcal{V}), \partial_t y \in L^2(0,T;\mathcal{H}), \partial_t^2 y(0,T;\mathcal{V}^*)\} \tag{9}$$

where $L^2(0,T;\cdot)$ is a space of abstract functions which are square Bochner-integrable, $\mathcal{H} = L^2(\mathcal{S})^2 \times L^2(\mathcal{S}) \times L^2(\mathcal{S})^2$ is a rigged Hilbert space and $\mathcal{V}^*$ is the dual space of $\mathcal{V}$.

By starting from full 3D-equation of momentum $\partial_t^2\ U(t) - \operatorname{div}(\sigma(U(t))) = F(t)$ in $\mathcal{B}_{(\tau)}$ for $t \in [0,T]$ we can first switch to a weak formulation and then simplify using the above mentioned Reissner-Mindlin kinematics and plain-stress assumption, but no further shell-related simplifications, e.g. Naghdy or Koiter models. We can state dynamic deformation equations in variational form:

Given a surface loading $f \in H^1(0,T;L^2(\mathcal{S}))$, find $y \in W(0,T)$, so that

$$\varrho M_{(\tau)} \partial_t^2 y(t) + L_{(\tau)}\big(y(t)\big) = \ F(t) \ \text{ in } \mathcal{V}^* \text{ for all } t \in [0,T], \tag{10}$$

together with initial conditions $y(0) = 0, \partial_t y(0) = g/\tau$ where $g \in \mathcal{V}$ represents an initial impact on the shell body and ϱ is the density. In state equation (10) we have the linear operator $M_{(\tau)}\colon \mathcal{V}^* \to \ \mathcal{V}^*$ arising from dynamical part,

$$M_{(\tau)}(u,\theta) = \begin{pmatrix} \tau & 0 & \frac{\tau^3}{12R} \\ 0 & \tau & 0 \\ \frac{\tau^3}{12R} & 0 & \frac{\tau^3}{12} \end{pmatrix} \begin{pmatrix} \underline{u} \\ u_3 \\ \theta \end{pmatrix} \tag{11}$$

and the linear operator $L_{(\tau)}\colon \mathcal{V} \to \mathcal{V}^*$,

$$L_{(\tau)}(u,\theta)(v,\psi) = \int_{\Omega_{(\tau)}} \mathbf{e}(u,\theta)^T\, \mathbf{C}\mathbf{e}(v,\psi) + \zeta(u,\theta)^T \mathbf{D} \zeta(v,\psi) \mathrm{d}V, \tag{12}$$

where this part is also known as *basic-shell-model*, introduced in [1] and analyzed in [2]. The functional $F(t) \in \mathcal{V}^*$ represents a loading applied on the midsurface in orthogonal direction, i.e.

$$F(t)(v,\psi) = \int_\omega f v_3 \mathrm{d}S. \tag{13}$$

Finally, we can state our optimization problem

$$
\begin{aligned}
&\min_{\substack{\tau\in W^{1,\infty}(\mathcal{S})\\ y=(u,\theta)\in W(0,T)}} \; J(u,\theta;\tau) := \int_0^T \|u\|^2 dt + \frac{\lambda}{2}\|\tau\|^2_{H^1(\mathcal{S})}\\
&\text{s.t. } \varrho M(\tau)\partial_t^2 y(t) + L_{(\tau)}\big(y(t)\big) = F(t) \text{ in } \mathcal{V}^* \text{ for } t\in[0,T]\\
&y(0) = 0, \partial_t y(0) = \frac{g}{\tau}\\
&\tau_{\min} \le \tau(x,\varphi) \le \tau_{\max} \text{ in } \mathcal{S}, \int_\omega \tau \,\mathrm{d}S = C.
\end{aligned} \tag{14}
$$

4. Analysis of the problem

We want to study state equation (10) according to existence and uniqueness of a solution and Gâteaux-differentiability of the solution w.r.t. thickness. Let us collect all the thickness restrictions in $U_{\mathrm{ad}} := \left\{\tau \in W^{1,\infty}(\mathcal{S}) \;\middle|\; \tau_{\min} \le \tau(x,\varphi) \le \tau_{\max} \text{ in } \mathcal{S}, \int_\omega \tau \,\mathrm{d}S = C\right\}$.

Theorem 1. *Let $f \in H^1(0,T;\, L^2(\mathcal{S}))$ and $g \in \mathcal{V}$ be given. For $\tau \in U_{ad}$, the variational problem (10) has an unique solution in $W(0,T)$.*

Proof. Proven by using techniques from [4] together with analysis of $L_{(\tau)}$ from [1] and analysis of $M_{(\tau)}$. □

Definition 1. We call the operator $G: U_{\mathrm{ad}} \to W(0,T)$, which maps the thickness τ to the solution $(y_\tau) \in W(0,T)$ of (10) *control-to-state-operator.*

Theorem 2. *The operator G is continuous and Gâteaux-differentiable. The directional derivative $G'(\tau)q = \bar{y} = (\bar{u},\bar{\theta})$ is given as the solution to*

$$
\begin{aligned}
&\varrho M_{(\tau)}\partial_t^2\bar{y}(t) + L_{(\tau)}\big(\bar{y}(t)\big) = -\varrho\big(M'_{(\tau)}q\big)\partial_t^2 y_{(\tau)}(t) - Z_{q,y_{(\tau)}(t)}\\
&\qquad\qquad\qquad\qquad\qquad\qquad \text{in } \mathcal{V}^* \text{ for } t\in[0,T],\\
&\bar{y}(0) = 0, \qquad \partial_t\bar{y}(0) = -\frac{g}{\tau^2}
\end{aligned} \tag{15}
$$

where $M'_{(\tau)}\, q$ means Gâteaux-derivative of $M_{(\tau)}$ w.r.t. τ in direction q and

$$
\begin{aligned}
&Z_{q,(u_{(\tau)},\theta_{(\tau)})}(v,\psi)\\
&\quad = -\int_\omega \sum_{h_i\in\left\{\pm\frac{\tau}{2}\right\}} \Bigg[\Big(\mathbf{e}\big(u_{(\tau)},\theta_{(\tau)}\big)^T\mathbf{C}\mathbf{e}(v,\psi)\\
&\quad + \zeta\big(u_{(\tau)},\theta_{(\tau)}\big)^T\mathbf{D}\zeta(v,\psi)\Big)\left(1+\frac{h}{R}\right)\bigg|_{h=h_i}\Bigg]\frac{q}{2}\,\mathrm{d}S.
\end{aligned}
$$

Proof. By using results from [2] for $L_{(\tau)}$ and differentiability of $M_{(\tau)}$ w.r.t. τ together with estimates from theory of hyperbolic PDE regarding dependence of the solution from initial data. □

Theorem 3. *The reduced objective $J_s: U_{\mathrm{ad}} \to \mathbb{R}, J_s(\tau) := J(G(\tau),\tau)$ is Gâteaux-differentiable and it holds*

$$
J_s'(\tau)q = -\int_0^T \Big(\varrho\big(M'_{(\tau)}q\big)\partial_t^2\, y_{(\tau)}(t), p(t)\Big)_{\mathcal{H}} + Z_{q,y_{(\tau)}(t)}p(t)\, dt + \lambda(\tau,q)_{H^1(\mathcal{S})} \tag{16}
$$

with adjoint $p \in W(0,T)$ as solution to

$$\begin{aligned} &\varrho M_{(\tau)}\partial_t^2 p(t) + L_{(\tau)}\big(p(t)\big) = 2\left(u_{(\tau)}(t), 0\right) \text{ in } \mathcal{V}^* \text{ f.a.} t \in [0,T], \\ &p(T) = 0, \qquad \partial_t p(T) = 0. \end{aligned} \tag{17}$$

Proof. By direct calculation.

5. Numerical solution

We solve the reduced problem $\min_{\tau\in U_{ad}} J_s(\tau)$ numerically in Fortran. The spatial discretization is done with 9-node-biquadratic shell elements. For time domain we use a Crank-Nicolson scheme. The resulting system is solved using Pardiso and the optimization is done using IpOpt. Note that the key for a successful optimization process is an expression for the gradient given to IpOpt that is based on (16) and not on finite differences. The optimization starts on a coarse grid consisting of 289 nodes and ends up on a fine grid with about 4000 nodes.

We consider a quarter tube of length 1, i.e. $\omega = [0,1] \times [\pi/4, 3\pi/4]$ with radius $R = 1$, $E = 210$, $\nu = 0.3$, $\varrho = 7.8$ and volume $C = \pi/20$ which corresponds to a constant thickness of 0.1. Minimum and maximum thickness are 0.05 and 0.15, respectively and a small regularization parameter $\lambda \approx 10^{-5}$ is used. We study the time domain $[0, 1]$. A mass "falling" onto the opposite side of the clamped edge $x = 0$ is giving an impact $g(x, \varphi) = -0.1a_3$ for $(x, \varphi) \in [0.9, \pi/2 - 0.05] \times [1, \pi/2 + 0.05]$. The mass stays on the panel and acts with its weight force $f(x, \varphi) = -a_3$ in the same region, see Fig. 1.

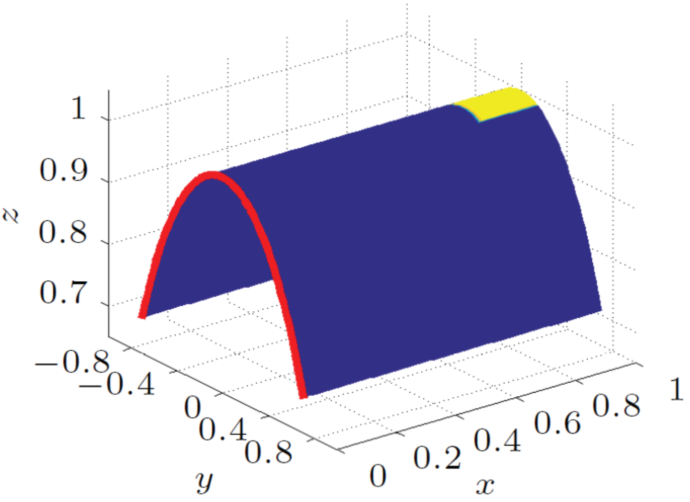

Fig. 1. Initial configuration with loaded region (yellow) and clamped edge (red).

The corresponding optimal thickness (solution to (14)) is shown in Fig. 2. We see a region of maximal thickness surrounding the loaded region as well as kind of trusses emerging to the loose edges of the shell. Like the load, the optimal thickness is symmetric to the φ-coordinate. Moreover, a small moderate thick region is placed nearer to the clamped edge. This thickness distribution could also be an interesting starting point for topology optimization where regions with minimal thickness are considered as holes.

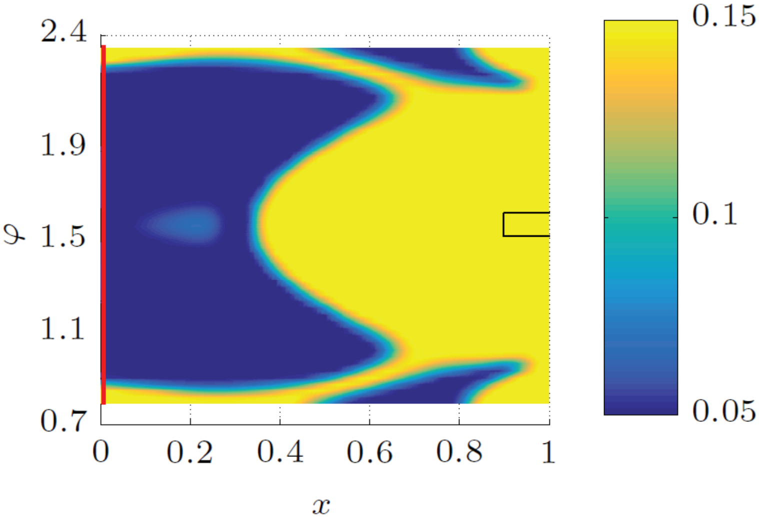

Fig. 2. Optimal thickness over parameter domain (color), loaded region (black line) and clamped edge (red line).

References

[1] D. Chapelle and K.J. Bathe. The Finite Element Analysis of Shells – Fundamentals. Springer, 2003.

[2] P. Ziemann. Optimal Thickness of a Cylindrical Shell. *Mathematics and its Applications*, Vol. 6, No. 2, 2015, pp. 214–234.

[3] P. Nestler. Optimal Thickness of a Cylindrical Shell Under a Time-Dependent Force. *Journal of Optimization Theory and Applications*, 2013, pp. 1–23.

[4] J. Wloka. *Partial Differential Equations*. Cambridge University Press, 1987.

Influence of dynamic processes in a film on damage development in an adhesive base

Suleiman Al-lubani[1], Aiman A. Al Alawin[2], Nabil W. Musa[3]

Mechanical Engineering Department, Philadelphia University
Amman, Jordan
[1]slubani@philadelphia.edu.jo, [2]aalawin@yahoo.com, [3]nmusa@philadelphia.edu.jo

Keywords*:* *aluminum alloy, allying elements, hardness, neural networks.*

In this study the effect of alloying elements on hardness using mathematical modeling tool of artificial neural networks (ANN) was analyzed. The mathematical model has been used for the prediction of hardness for different series of aluminium alloys. Different compositions contents of Cr, Cu, Fe, Mg, Mn, Si, Ti, Zn and aluminium as a major alloying elements have been considered as the input data and the hardness as an output. A database has been established for different series of aluminum alloys. Different series of aluminum alloys and different contents of alloying elements have been defined as the input layer of ANN model. The output layer of the ANN model consists of hardness values. The present research work shows that the improved model could increase the accuracy of the predicted results of mechanical properties of aluminum alloy. This model can also predict the hardness within an average error of less than 1%.

Numerical modeling of cross-flow induced vibrations on circular cylinder at high Reynolds number

Sabine Upnere[1,2], **Normunds Jekabsons**[2,3]

[1] *Institute of Mechanics, Riga Technical University*
Riga, Latvia
[2] *Engineering Research Institute Ventspils International Radio Astronomy Center,*
Ventspils University College
Ventspils, Latvia
[1] *upnere@gmail.com,* [3] *normundsj@venta.lv*

Keywords: *cross-flow,vibrations, fluid-structure interaction.*

This work presents the study of modeling of fluid flow and circular cylinder interaction in order to investigate cross-flow induced vibrations.

The flow around cylinder has been extensively investigated because of its wide applications in civil engineering, such as offshore structures, tall towers or stacks or nuclear reactors.

The high velocity fluid flow interaction with structural components can induces self-excited vibrations of the components. The fluidelastic instability can lead to the maintenance and operational problems.

In order to analyzed flow induced vibration two-dimensional and three-dimensional Finite Element Models have been developed using commercial software. Comparison of numerical and analytical results have been done.

Authors Index